(2)

AFOSR-TR- 89-0360

Molecular Optics: Nonlinear Optical Processes in Organic and Polymeric Crystals and Films

Professor A. F. Garito

UNIVERSITY of PENNSYLVANIA

DEPARTMENT OF PHYSICS

Philadelphia, Pennsylvania

(2)

Molecular Optics: Nonlinear Optical Processes in Organic and Polymeric Crystals and Films

Professor A. F. Garito

UNCLASSIFIED
SECURITY CLASSIFICATION OF THIS PAGE

REPORT DOCUMENTATION PAGE

Form Approved OMB No. 0704-0188

1a. REPORT SECURITY CLASSIFICATION: UNCLASSIFIED	1b. RESTRICTIVE MARKINGS
2a. SECURITY CLASSIFICATION AUTHORITY	3. DISTRIBUTION/AVAILABILITY OF REPORT: Approved for public release; Distribution unlimited
2b. DECLASSIFICATION/DOWNGRADING SCHEDULE	
4. PERFORMING ORGANIZATION REPORT NUMBER(S)	5. MONITORING ORGANIZATION REPORT NUMBER(S): AFOSR-TR- 89-0360
6a. NAME OF PERFORMING ORGANIZATION: University of Pennsylvania; 6b. OFFICE SYMBOL (If applicable)	7a. NAME OF MONITORING ORGANIZATION: AFOSR/NC
6c. ADDRESS (City, State, and ZIP Code): Department of Physics, Philadelphia, PA 19104	7b. ADDRESS (City, State, and ZIP Code): Building 410, Bolling AFB, DC 20332-6448
8a. NAME OF FUNDING/SPONSORING ORGANIZATION: AFOSR; 8b. OFFICE SYMBOL (If applicable): NC	9. PROCUREMENT INSTRUMENT IDENTIFICATION NUMBER: F49620-85-C-0105
8c. ADDRESS (City, State, and ZIP Code): Building 410, Bolling AFB, DC 20332=6448	10. SOURCE OF FUNDING NUMBERS: PROGRAM ELEMENT NO. 61102F; PROJECT NO. 2303; TASK NO. A3; WORK UNIT ACCESSION NO.

11. TITLE (Include Security Classification)
Molecular Optics: Nonlinear Optical Processes in Organic and Polymeric Crystals and Films

12. PERSONAL AUTHOR(S)
A. F. Garito

13a. TYPE OF REPORT	13b. TIME COVERED	14. DATE OF REPORT (Year, Month, Day)	15. PAGE COUNT
FINAL	FROM 6/85 TO 4/88		147

16. SUPPLEMENTARY NOTATION

17. COSATI CODES			18. SUBJECT TERMS (Continue on reverse if necessary and identify by block number)
FIELD	GROUP	SUB-GROUP	

19. ABSTRACT (Continue on reverse if necessary and identify by block number)

Experimental and theoretical studies have firmly established that the largest second and third order microscopic nonlinear optical susceptibilities occur in organic and polymer systems. This major developement has resulted in studies in optical bistability, phase conjugate wave generation, and neural networks.

The physical microscopic origin and mechanism of second and third order nonlinear optical responses in conjugate polymers has been investigated. New theoretical concepts relating to the many-body nature of highly charge-correlated pi-electron states have been devloped. The nonlinear optical reponses of new pi-electron topological structures have been calculated, optical bistability in nonlinear optical conjugated polymers has been demonstrated.

20. DISTRIBUTION/AVAILABILITY OF ABSTRACT	21. ABSTRACT SECURITY CLASSIFICATION	
☒ UNCLASSIFIED/UNLIMITED ☒ SAME AS RPT ☐ OTIC USERS	UNCLASSIFIED	
22a. NAME OF RESPONSIBLE INDIVIDUAL: Dr. Donald R. Ulrich	22b. TELEPHONE (Include Area Code): (202) 767-4963	22c. OFFICE SYMBOL: NC

DD Form 1473, JUN 86 — Previous editions are obsolete. — SECURITY CLASSIFICATION OF THIS PAGE

UNCLASSIFIED

FINAL TECHNICAL REPORT

1 May 85 - 30 April 88

TITLE: Molecular Optics: Nonlinear Optical Processes in Organic and Polymeric Crystals and Films

PRINCIPAL INVESTIGATOR: Prof. A. F. Garito (215) 898-5810

PROGRAM MANAGER: Dr. Donald Ulrich (202) 767-4960

ARPA ORDER: 4989/2 PROGRAM CODE: 5D10

CONTRACTOR: University of Pennsylvania

EFFECTIVE DATE: 1 May 85 EXPIRATION DATE: 30 Apr 88

CONTRACT NUMBER: F49620-85-C-0105 AMOUNT: $1,572,201

Sponsored by
Advanced Research Projects Agency (DOD)
ARPA Order No. 4989/2

Monitored by
AFOSR Under Contract # F49620-85-C-0105

I. SUMMARY

Through experimental and theoretical studies, the Penn nonlinear optics research program, principally funded by DARPA and AFOSR, has firmly established that the largest second $\chi^{(2)}_{ijk}$ $(-\omega_3;\omega_1,\omega_2)$ and third $\chi^{(3)}_{ijkl}$ $(-\omega_4;\omega_1,\omega_2,\omega_3)$ order nonlinear optical properties occur in organic and polymer systems. This major development together with progress in optical bistability, phase conjugate wave generation, and neural networks has stimulated considerable research and development activities in centers throughout the world with many potential applications being pursued in optical signal processing, integrated optics, image reconstruction, sensor protection, data storage, and optical memory and logic technologies. Most notably, many industrial laboratories have successfully developed electrooptic polymers and devices based on the experimental and theoretical results achieved by the current research program.

The major purpose of the research program is to further rapidly accelerate and expand these advances in nonlinear optics research. The principal approach and objectives during the last grant period were comprised of the following original statements.

o Investigate the physical microscopic origin and mechanism of second and third order nonlinear optical responses in conjugated polymers.

o Develop new theoretical concepts relating to the many-body nature of highly charge-correlated π-electron states.

o Calculate nonlinear optical responses of new π-electron topological structures.

o Determine frequency dependent third order $\chi^{(3)}$ and n_2 respones at fast time scales.

o Demonstrate optical bistability in nonlinear optical conjugated polymers.

The remainder of the report is organized in two major sections. Section **II** contains reviews of Selected Research Highlights from the research program during the past two year funding period. Section **III** provides an extended description of major advances illustrative of the results obtained by the funded research program. This section contains

the subjects (I) Nonlinear Optical Processes in Lower Dimensional Conjugated Structures, and (II) Frequency Dependence of the Optical Kerr Effect and Third Order Electronic Nonlinear Optical Processes of Organic systems.

II. SELECTED RESEARCH HIGHLIGHTS

1. ELECTRON DENSITY CORRELATION DIAGRAMS. MICROSCOPIC ORIGIN AND MECHANISM OF NONLINEAR OPTICAL PROCESSES IN CONJUGATED LINEAR CHAINS

The fundamental problem of understanding the origin of large, nonresonant second order macroscopic nonlinear optical susceptibilities observed for conjugated π-electron organic and polymer solids is currently viewed as reducible to theoretical and experimental studies of the corresponding microscopic susceptibilities of single molecular, or polymer chain, units making up the nonlinear optical medium.

Linear polyenes and polyenynes represent the finite chain limit to the corresponding quasi-one-dimensional conjugated polymer chain, and phase matched second harmonic generation, for example, has been demonstrated earlier by us for noncentrosymmetric diacetylene conjugated polymer structures. In this regard, for the fundamentally important case of a noncentrosymmetric linear polyenyne NMDVDA [trans-trans 1-(4 methylphenyl)-8-(4'-nitrophenyl)-1, 7-diene-3,5-octadiyne],

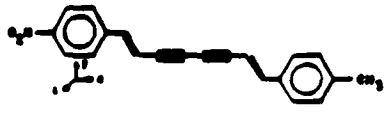

we reported last year the first results of DC induced second harmonic generation (DC SHG) measurements of $\beta_{ijk}(-2\omega;\omega,\omega)$ (Figure 2.1.1).

Electron correlations play an important role in the nonlinear optical responses of conjugated organic structures, and their description of microscopic second and third order nonlinear optical responses differs markedly from independent particle models. As a result, large charge asymmetries occur in the virtual excitation processes, and we have long sought a quantitative diagrammatic description of these features of the fundamental mechanism. This year we successfully developed a diagrammatic theoretical formalism that links the results of our many-

electron calculation of $\beta_{ijk}(-2\omega;\omega,\omega)$ by SCF-MO-SDCI methods with experimental results (Figure 2.1.1).

Electron density correlation diagrams based on the electron state functions provide a compact graphical representation of important microscopic features for second order nonlinear optical processes. The transition moment $\mu^{i}_{nn'}$ is expressed in terms of the transition density matrix $\rho_{nn'}(r,r')$ by $\langle\mu_{nn'}\rangle = -e\int_{r=r'} r\,\rho_{nn'}(r,r')\,dr$ and the dipole moment difference $\Delta\mu^{i}_{n}$ by the difference density function $\rho_n-\rho_g$ between the excited and ground state functions $\langle\Delta\mu_n\rangle = -e\int r\,(\rho_n-\rho_g)\,dr$ where ρ_n is the first order reduced density matrix.

Electron density correlation diagrams $\rho_n-\rho_g$ and $\rho_{nn'}$ for second order processes in NMDVDA involving the dominant contributing states I, III and IV are plotted as examples in Figure 2.1.2. The solid and dashed lines correspond to negative and positive values, respectively. In each case, upon virtual excitation in the second order process, large asymmetric redistribution of electron density occurs along the conjugated chain, especially in the x direction, resulting in large dipole moment differences $\Delta\mu^{i}_{n}$ (Figures 2.1.2a and 2.1.2b) and transition moments $\mu^{x}_{nn'}$ (Figure 2.1.2c) that determine β_x. Thus, for example, $\rho_{IV}-\rho_g$ of Figure 2.1.2b corresponding to $\Delta\mu^{x}_{IV}$ of 33.5D exhibits a large correlation distance between positive and negative regions along the x-direction in comparison to $\rho_I-\rho_g$ of Figure 2.1.2a with its associated value of $\Delta\mu^{x}_{I}$ of 18.7D. The same charge correlated features are exhibited by $\rho_{I,IV}$ of Figure 2.1.2c where the $\mu^{x}_{I,IV}$ of 12.8D is relatively large. Thus, our electron density correlation diagrams provide a quantitative diagrammatic formalism for nonlinear optical processes. Moreover, the formalism is general and can represent the microscopic features of second or third order processes for any conjugated structure.

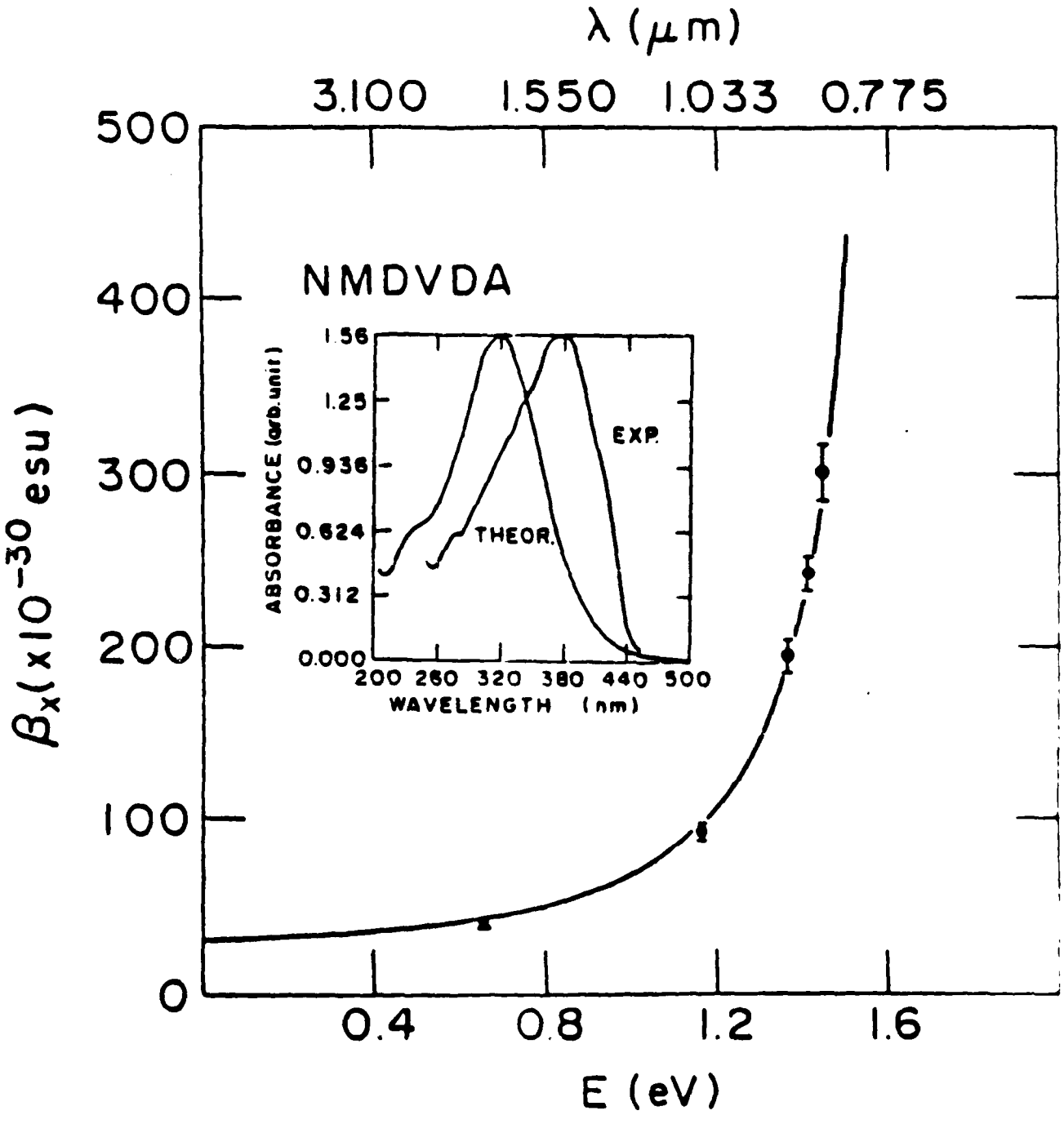
λ (μm)
3.100
1.550
1.033
0.775
500
400
300
200
100
0
NMDVDA
β_x (x10^{-30} esu)
ABSORBANCE (arb.unit)
1.56
1.25
0.936
0.624
0.312
0.000
EXP.
THEOR.
200 260 320 380 440 500
WAVELENGTH (nm)
0.4
0.8
1.2
1.6
E (eV)

Figure 2.1.1

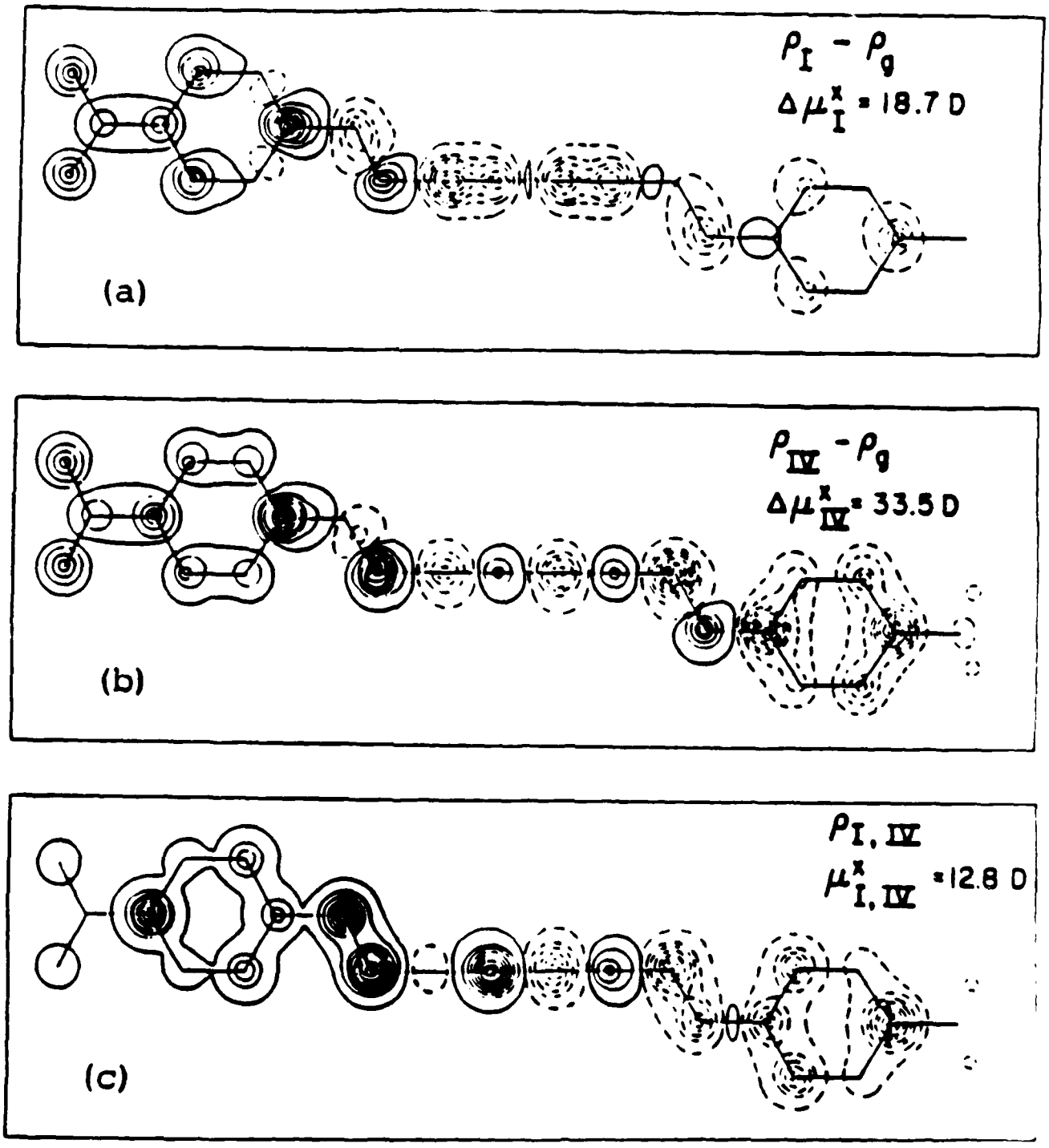
$\rho_I - \rho_g$
$\Delta\mu_I^x = 18.7$ D
(a)
$\rho_{IV} - \rho_g$
$\Delta\mu_{IV}^x = 33.5$ D
(b)
$\rho_{I,IV}$
$\mu_{I,IV}^x = 12.8$ D
(c)

Figure 2.1.2

II. DISPERSION OF RESONANT SECOND HARMONIC GENERATION IN ORGANIC NONLINEAR OPTICAL ULTRATHIN FILMS.

Organic and polymer structures possess unusually large, ultrafast second and third order macroscopic nonlinear optical properties that are fundamentally important to the field of nonlinear optics and provide previously unachievable design features for device implementation in optical technologies. The macroscopic nonlinear optical properties of multilayer thin films can be formed and tailored as nonlinear optical ultrathin films by Langmuir-Blodgett techniques. Earlier, using novel x-ray scattering and data analysis methods, we had reported the profile structures of such films which possess mosaic spreads much less than semiconductor single crystals and allow sufficient accuracy and spatial revolution to accurately(±1 Å) position molecular bonding sequences in a single bilayer.

In this report, we describe the first experimental and theoretical results of resonant second harmonic generation of a single asymmetric organic monolayer of a cyclic polyene DCNQI (Figure 2.2.1). Figure 2.2.2 shows the frequency dependent microscopic second order nonlinear optical susceptibility $\beta_{ijk}(-2\omega;\omega,\omega)$ of a DCNQI monolayer. Included are off-resonance results obtained from separate DCSHG liquid solution measurements. With increased frequency, the β_x values starting at approximately -30×10^{-30} esu increase smoothly to a resonant two-photon maximum of -260×10^{-30} esu near 800 nm corresponding to the singlet-singlet excitation to the first p-electron excited state of DCNQI.

The theoretical solid curve in Figure 2.2.2 was calculated by SCF-MO-SDCI methods in the rigid lattice CNDO/s approximation that included both singly (SCI) and doubly excited configurations (DCI) to account for electron correlations. Comparison of theory and experiment is quite satisfactory.

Density matrices of the state functions provide a compact graphical representation of important microscopic features for second order nonlinear optical processes. Contour diagrams for the states principally responsible for β_x are plotted in Figure 2.2.3 where the

solid and dashed lines correspond to negative and positive values, respectively. In each case, upon virtual excitation in the second order process, large asymmetric redistribution of electron density occurs with large correlation distances across the conjugated structure, especially in the large dipole x direction. This correlated π-electron redistribution results in large dipole moment differences and transition moments that determine β_x.

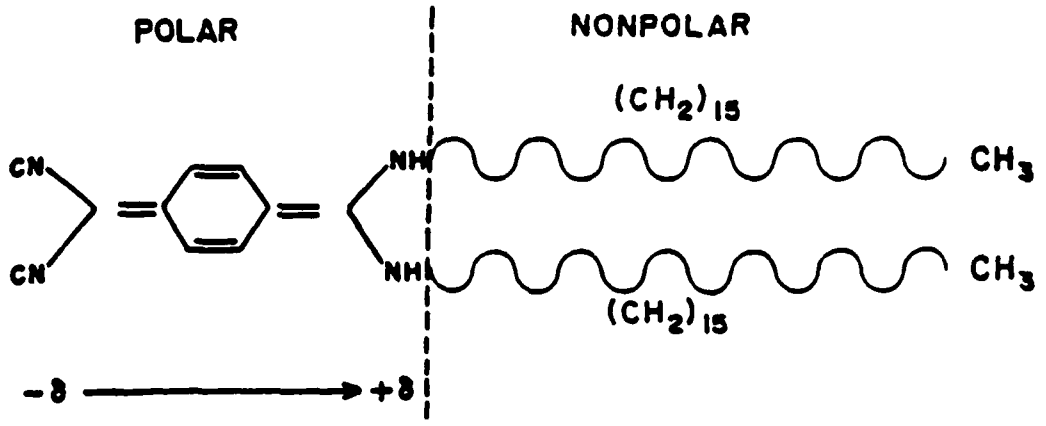

Figure 2.2.1

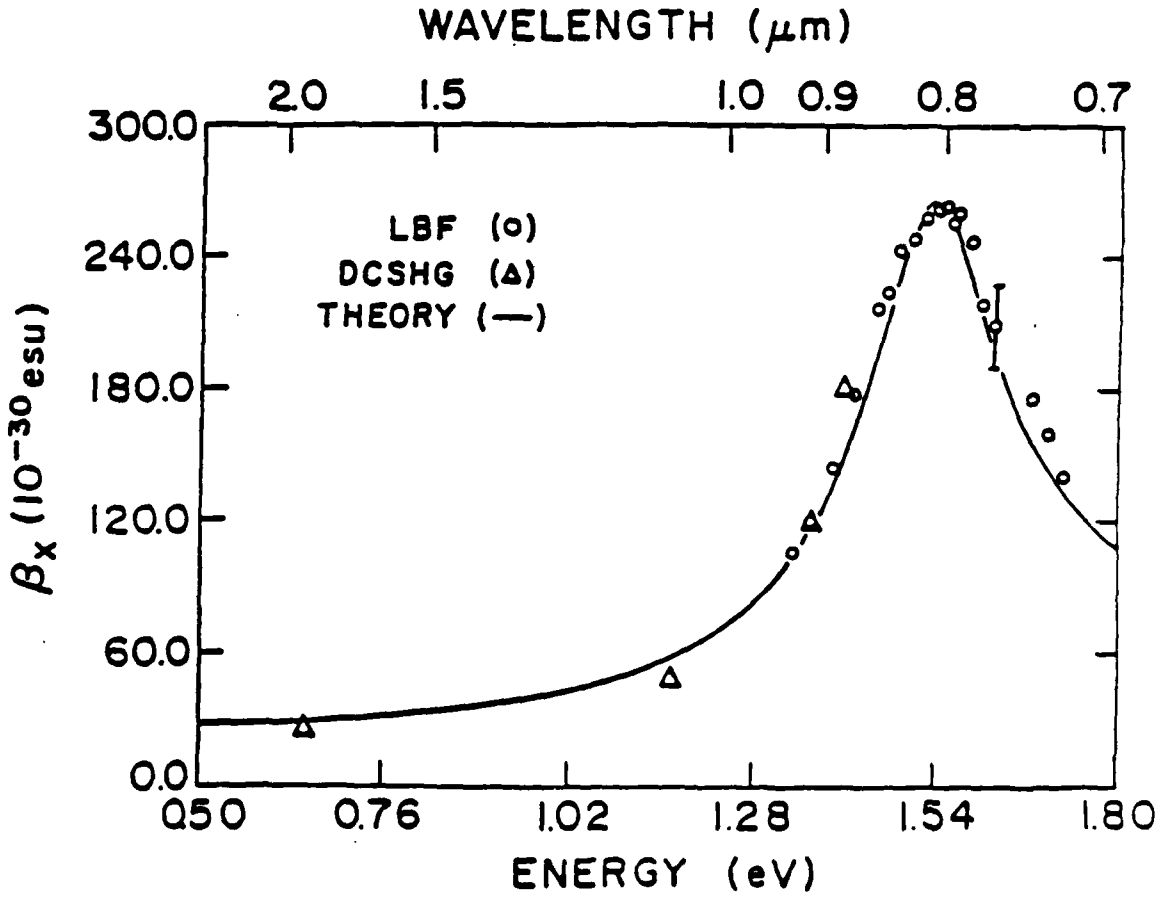

Figure 2.2.2

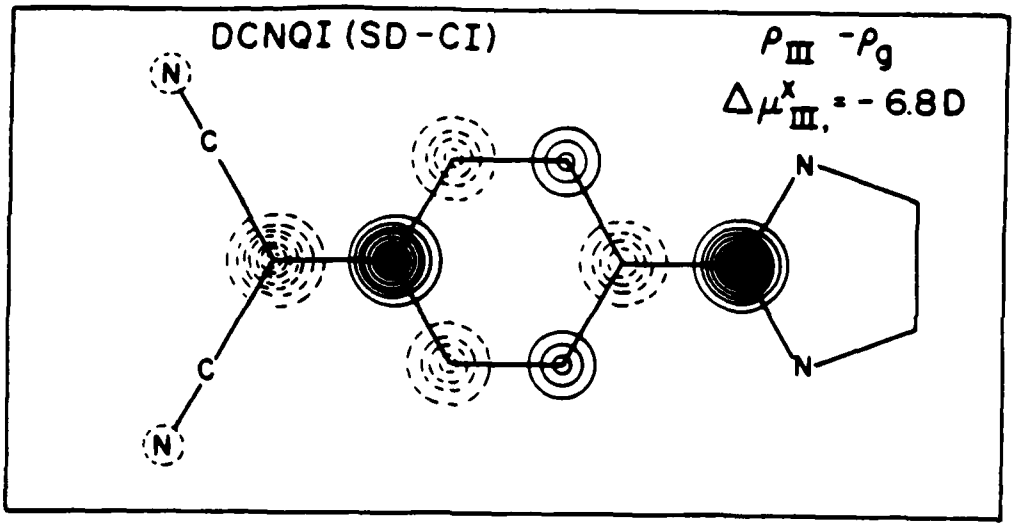
DCNQI (SD-CI)
$\rho_{III} - \rho_g$
$\Delta\mu^x_{III} = -6.8D$
N
C
C
N
N
N

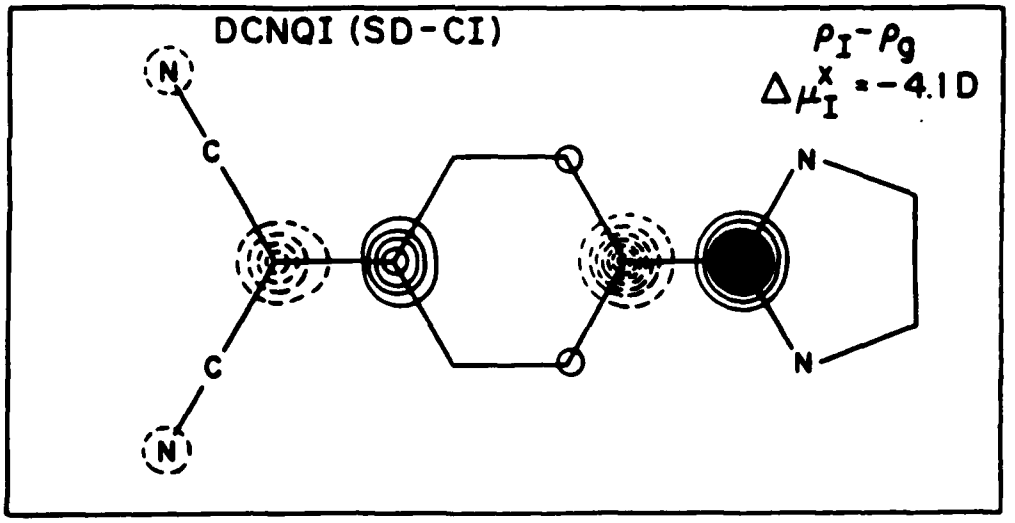
DCNQI (SD-CI)
$\rho_I - \rho_g$
$\Delta\mu^x_I = -4.1D$
N
C
C
N
N
N

Figure 2.2.3

III. DESIGN OF NOVEL STRUCTURES WITH UNUSUALLY LARGE SECOND ORDER RESPONSES

It is now widely accepted that conjugated organic polymer materials possess the largest electronic nonlinear optical responses. Use of organic materials in optical device implementation has already been under intense development in several industrial laboratories and considerable success has been achieved, particularly in the production of electrooptic guest-host polymer thin film devices. To further improve the performance of these devices, it has now become more and more important that specific molecular structures with larger second order susceptibilities $\beta_{ijk}(-\omega_3;\omega_1,\omega_2)$ be developed. We have long held the view that in order to achieve advances in the design of π-electron structures with large values of $\beta_{ijk}(-\omega_3;\omega_1,\omega_2)$, it is essential to have a complete microscopic understanding of second order excitation processes in these many-electron systems. To this end we have successfully developed a many-electron formalism and method for the calculation of microscopic second order nonlinear optical responses. The results of this method provides direct insight and guidelines toward the design of new molecular systems.

The molecular dye MPC [N-methyl[4(1H)-pyridinylidene ethylidene]2,5-cyclohexadien-1-one] has been reported by a French research group

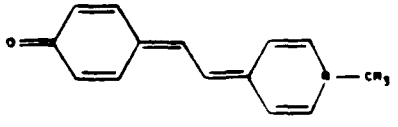

to have a measured $\beta_x(-2\omega;\omega,\omega)$ value of more than 1000×10^{-30} esu far off resonance. However we have studied MPC theoretically, and found by SCF-MO-SDCI methods that the β_x calculated value was much smaller by an order of magnitude. On the basis of our calculated results, we initiated detailed experimental studies of β_x at our laboratory together

with collaborative studies at AT&T laboratories that acted as blind tests. The results from both measurements confirmed not only the calculated value of β_x but also the sign and frequency dependence (Figure 2.3.1). The SCF-MO-SDCI method indeed provides a correct microscopic description of the nonlinear response of a molecule.

Our studies of quinoid ring structure DCNQI (see previous section of Research Highlights) motivated us to perform a complete theoretical analysis of the second order properties of the related extended ring structure DPHQ [2-(4'-dicyanomethylene bis cyclohexa-2,4,5,2',5'-pentaenylidine)-imidazolidine]

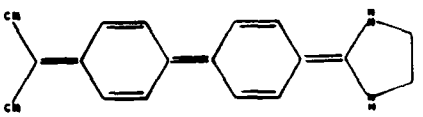

The calculated gas phase dispersion curve for β_x of DPHQ is given in Figure 2.3.2. It is seen that the magnitude of the β_x value is unusually large, achieving nonresonant magnitudes greater than 1000×10^{-30} esu which is the largest value ever observed. The origin of the magnitude, sign, and dispersion of β_x resides in the electron density redistribution accompanying second order virtual processes in the dominant excited state I. The characteristic features of this principal excited state I are illustrated in the ρ_I-ρ_g contour diagram of Figure 2.3.3a, along with the corresponding ρ_I-ρ_g contour diagram for MPC shown in Figure 2.3.3b for comparison. The contour diagram illustrates the highly separated, localized nature of the virtual electron density distribution of DPHQ along the dipolar x-direction compared to the modulated distribution in MPC. The net result is that although the molecular length along the dipolar axis is roughly the same for MPC and DPHQ, the corresponding magnitudes of the dipole moment $\Delta\mu_I^x$ are quite different, equal to 4.4D and 7.7D respectively. Similar results are found for the transition moments μ_{Ig}^x.

The highly correlated electron density redistribution is the primary reason for the unusually large β_x value for DPHQ.

In summary, we have demonstrated by both theoretical and experimental studies of extended cyclic ring structures that our theoretical procedures can successfully complement nonlinear optical experiments. Moreover, our microscopic description for β_{ijk} in terms of highly correlated excitation processes is essentially correct and, thereby, can guide the molecular designs of new structures having β_{ijk} values greater than 1000×10^{-30} esu.

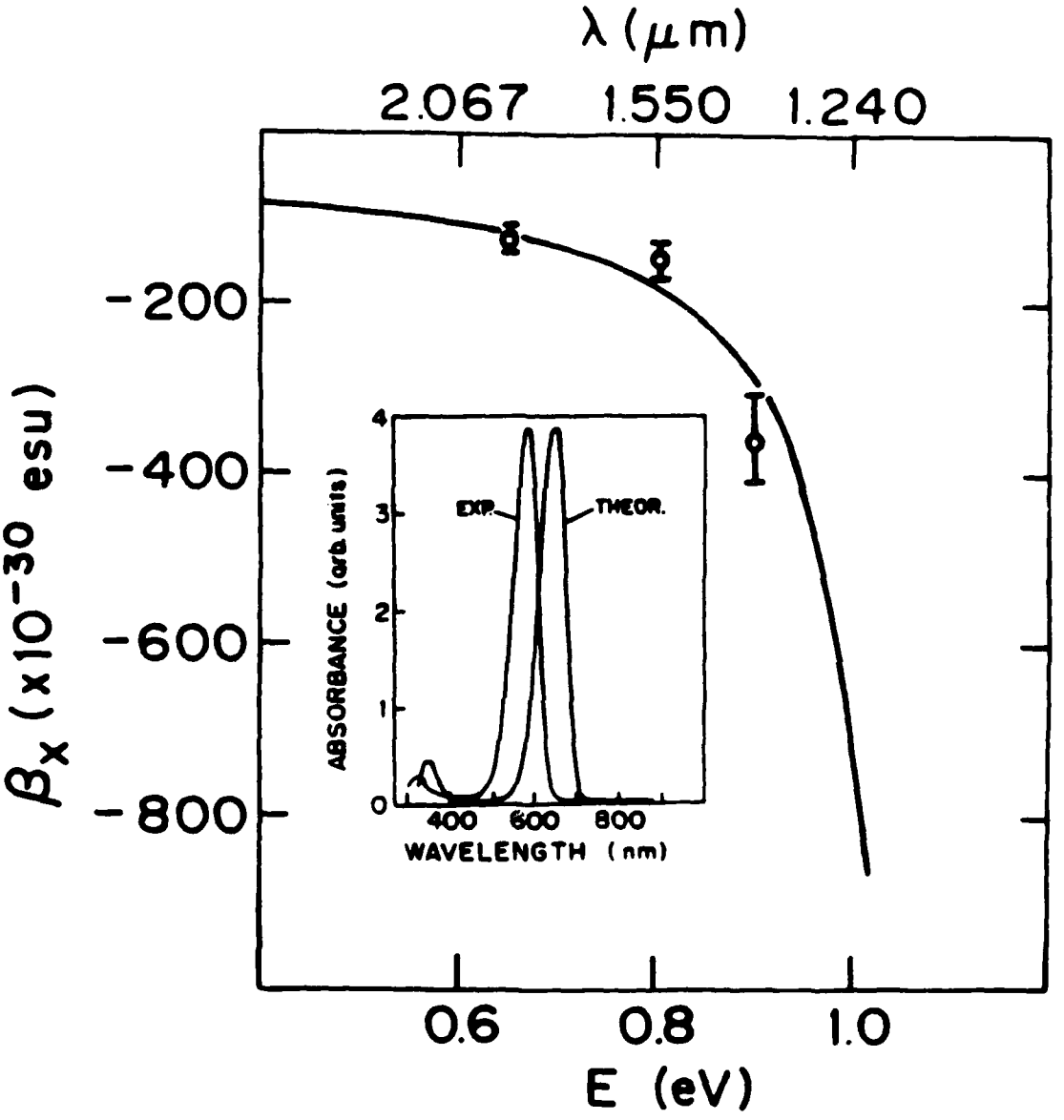
λ (μm)
2.067
1.550
1.240
-200
-400
-600
-800
β_x (x10^{-30} esu)
0.6
0.8
1.0
E (eV)
ABSORBANCE (arb. units)
EXP.
THEOR.
0
1
2
3
4
400
600
800
WAVELENGTH (nm)

Figure 2.3.1

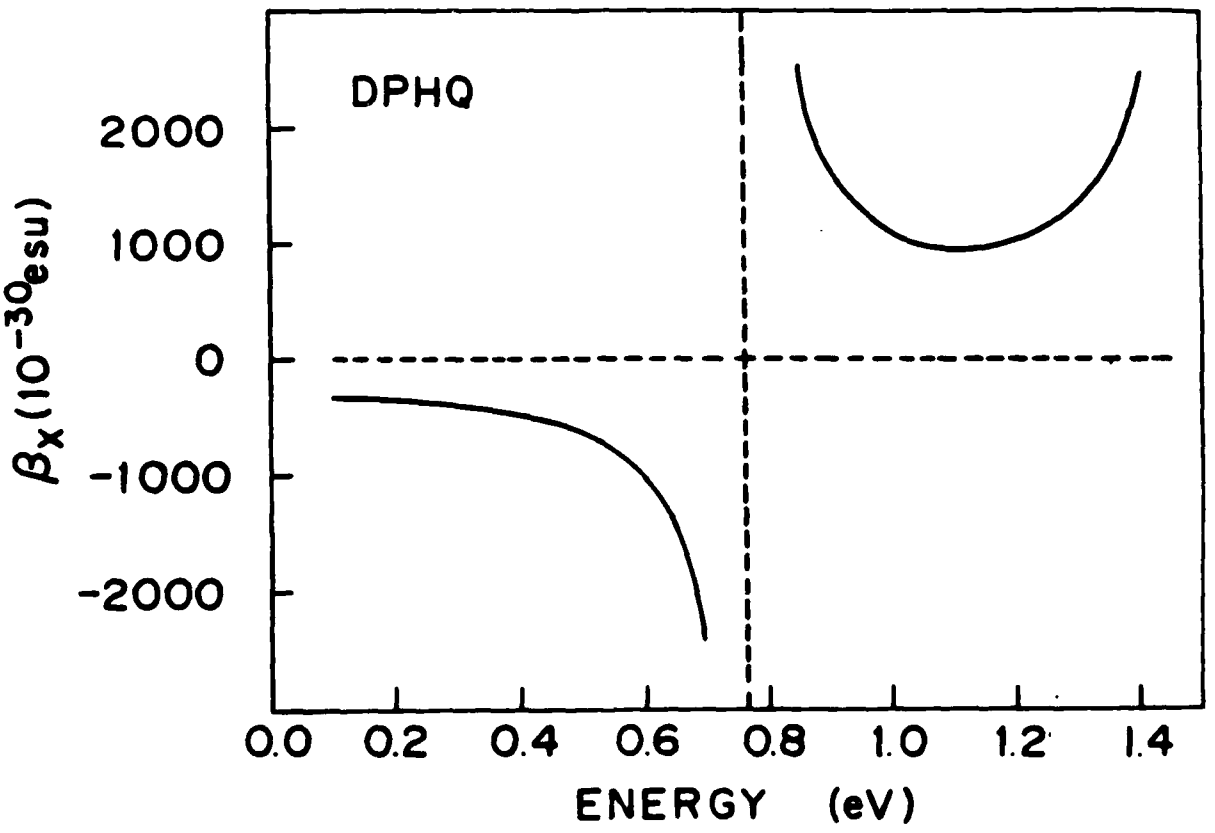
DPHQ
2000
1000
0
-1000
-2000
$\beta_x(10^{-30}esu)$
0.0
0.2
0.4
0.6
0.8
1.0
1.2
1.4
ENERGY (eV)

Figure 2.3.2

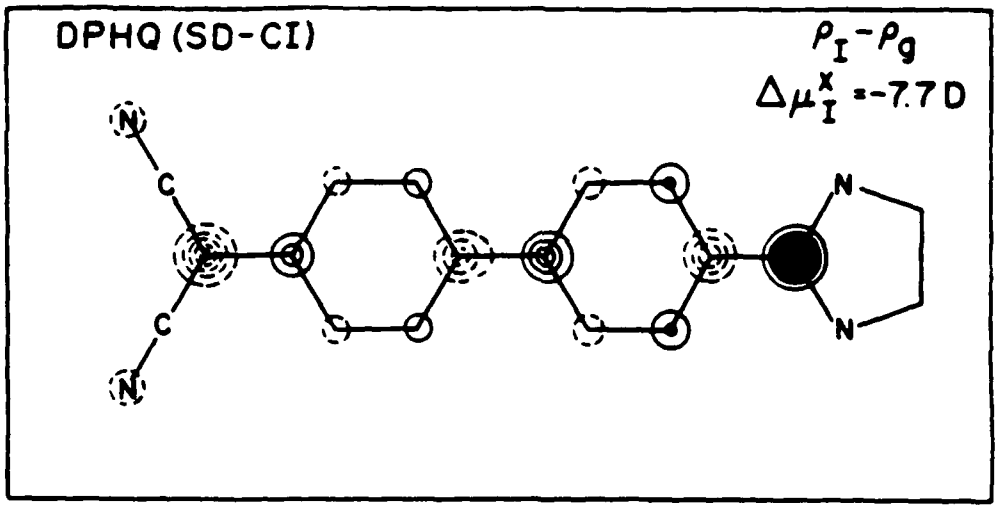

(a)

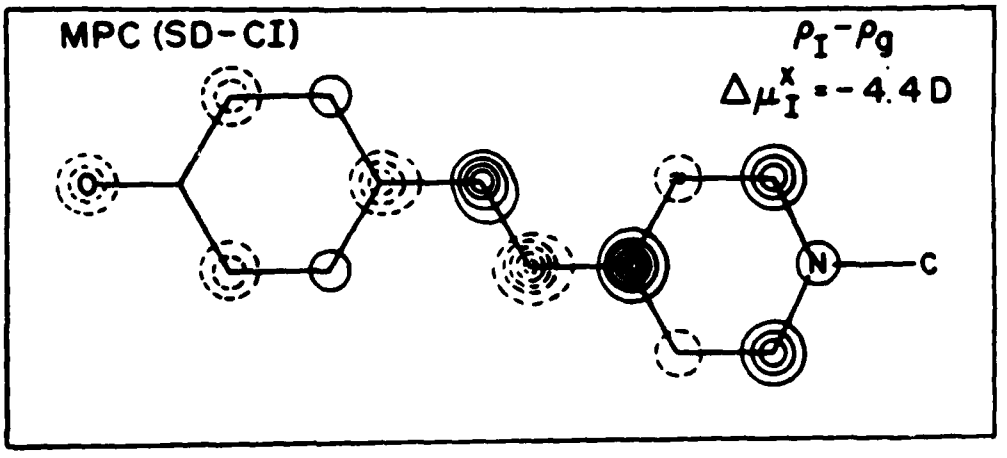

(b)

Figure 2.3.3

IV. NONLINEAR OPTICAL PROCESSES IN CONJUGATED POLYMERS: LARGE NONRESONANT THIRD ORDER ELECTRONIC RESPONSES IN HIGH PERFORMANCE LIQUID CRYSTAL POLYMER STRUCTURES

Organic and polymer structures exhibit unusually large, ultrafast second and third order nonlinear optical properties in a large number of structures, phases, and states. Rapid advances in the field can be achieved through further development of stable, high performance polymer structures having outstanding secondary properties as demonstrated, by example, by high performance liquid crystal PBZ polymers (Figure 2.4.1). For two such rigid rod polymer systems, PBI and PBT (Figure 2.4.2), our third harmonic generation measurements show that they possess large non-resonant third order optical susceptibilities whose origin resides in ultrafast, lossless excitations of highly charge correlated π-electron states.

Since each rigid rod polymer chain is essentially a densely packed, linear array of linked monomer units, a repeat unit can be viewed as the finite chain limit to the corresponding infinite polymer chain. Accordingly, we report experimental and theoretical studies of the microscopic third order susceptibilities $\gamma_{ijkl}(-\omega_4;\omega_3,\omega_2,\omega_1)$ of centrosymmetric TBOZ and TBTZ repeat unit structures of PBZ polymers.

The nonresonant macroscopic third harmonic susceptibility $\chi^{(3)}_L(-3\omega;\omega,\omega,\omega)$ was determined in the isotropic liquid phase by the wedge Maker fringe method. For an isotropic liquid, $\chi^{(3)}_L$ is related to the effective microscpic third order susceptibility $\gamma_L(-3\omega;\omega,\omega,\omega)$ by

$$\chi^{(3)}_L = N\left(\frac{2+n^2_{\omega}}{3}\right)^3\left(\frac{2+n^2_{3\omega}}{3}\right)\gamma_L \qquad (2.4.1)$$

where N is the number density, γ_L the orientational average of the microscopic susceptibility $\gamma_{ijkl}(-3\omega;\omega,\omega,\omega)$ and the refractive index terms are local field factors.

The frequency dependent microscopic $\gamma_{ijkl}(-3\omega;\omega,\omega,\omega)$ shown in Figure 2.4.3 was theoretically determined by SCF-MO-SDCI calculations including singly and doubly excited configurations to account for electron correlations. At λ = 1.907 μm (0.65 eV), the calculated γ_L value 11 x 10^{-36} esu agrees well with the experimental value of 13 x 10^{-36} esu. The major finding is that the microscopic origin of $\gamma_{ijkl}(-3\omega;\omega,\omega,\omega)$ is determined by virtual excitations to highly correlated two photon ^1A_g π-electron states through the first principal one photon ^1B_u excited state. Important features of the highly correlated virtual processes are compactly described by electron density correlation diagrams $\rho_{nn'}$. Figure 2.4.4a shows $\rho_{nn'}$ for the ^1A_g ground and ^1B_u excited states, and Figure 2.4.4b $\rho_{nn'}$ for the ^1B_u and two photon ^1A_g excited states. Thus, we also demonstrate the necessity of including doubly excited configurations in third order calculations as well as the important roles of symmetry and two photon states in third order processes.

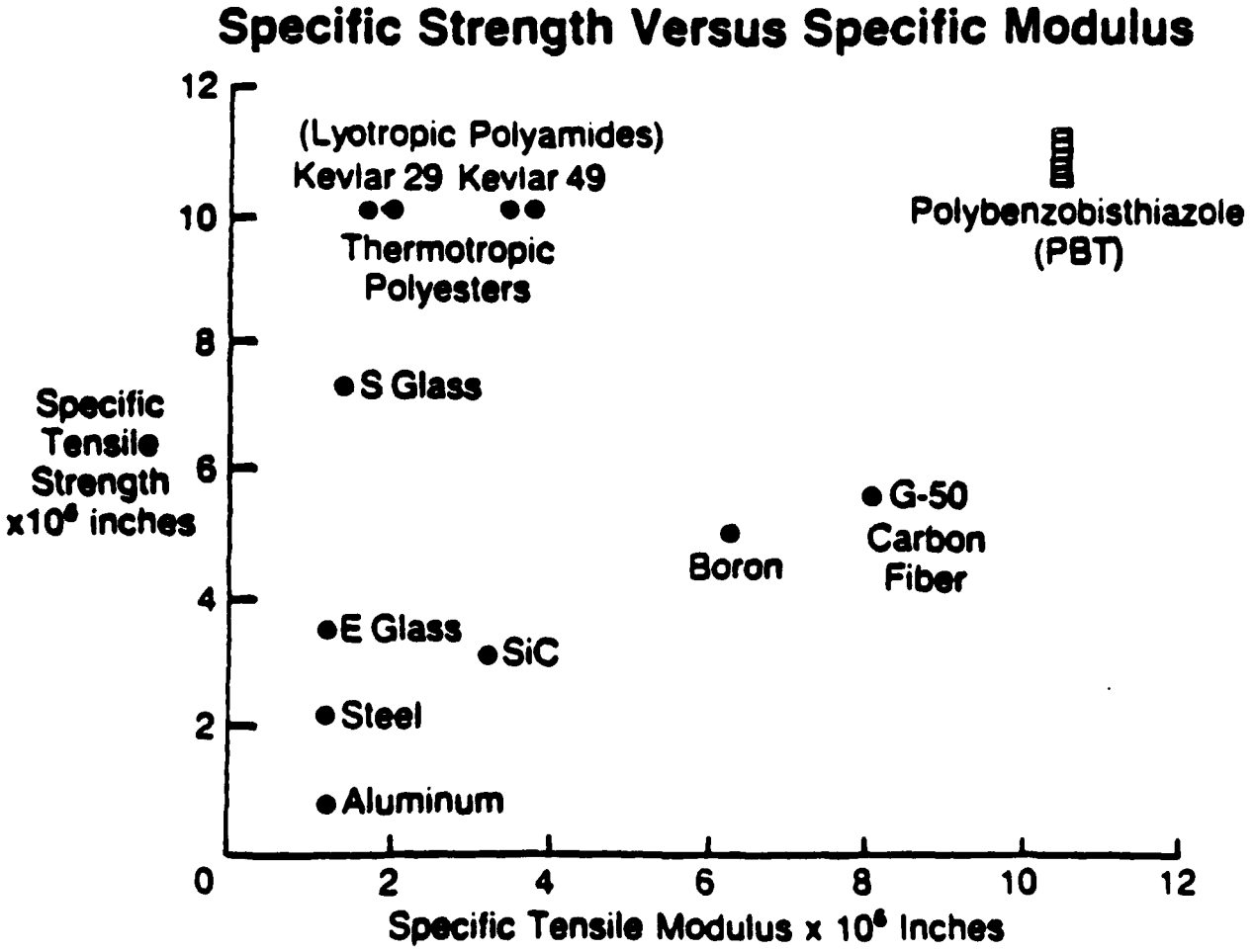
Specific Strength Versus Specific Modulus
(Lyotropic Polyamides)
Kevlar 29 Kevlar 49
Thermotropic
Polyesters
Polybenzobisthiazole
(PBT)
S Glass
G-50
Carbon
Fiber
Boron
E Glass
SiC
Steel
Aluminum
Specific
Tensile
Strength
x10⁶ inches
Specific Tensile Modulus x 10⁶ Inches
0
2
4
6
8
10
12

Figure 2.4.1

ELECTRONIC $\chi^{(3)}(-3\omega;\omega,\omega,\omega)$ OF ORDERED POLYMERS

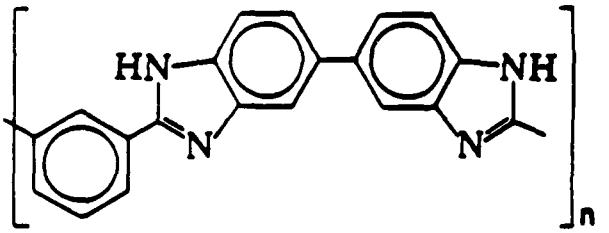

PBI

$\chi^{(3)}(-3\omega;\omega,\omega,\omega)$: $0.8\pm0.5\times10^{-12}$ esu

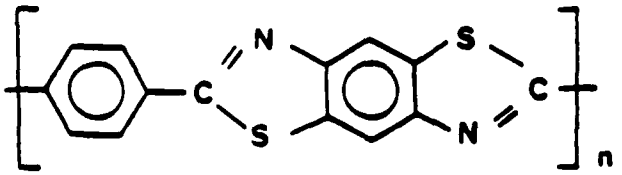

PBT

$\chi^{(3)}(-3\omega;\omega,\omega,\omega)$: $10-100\times10^{-12}$ esu

Figure 2.4.2

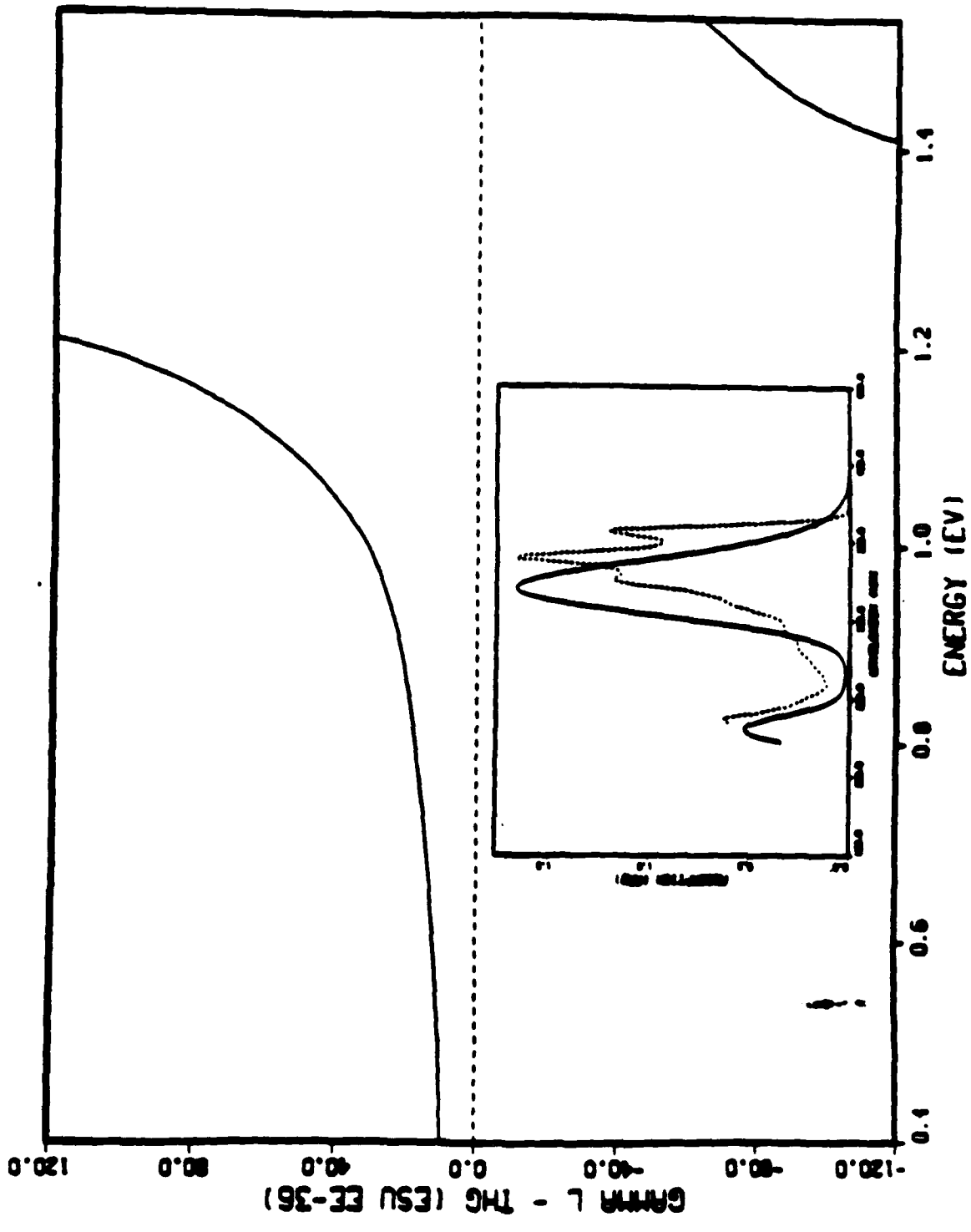

Figure 2.4.3 Calculated frequency dependent $\gamma_L(-3\omega;\omega,\omega,\omega)$. Insert Experimental and calculated optical absorption spectra. Solid Line Theoretical; dotted line: experimental gas phase; dashed line: experimental solution phase in dioxane.

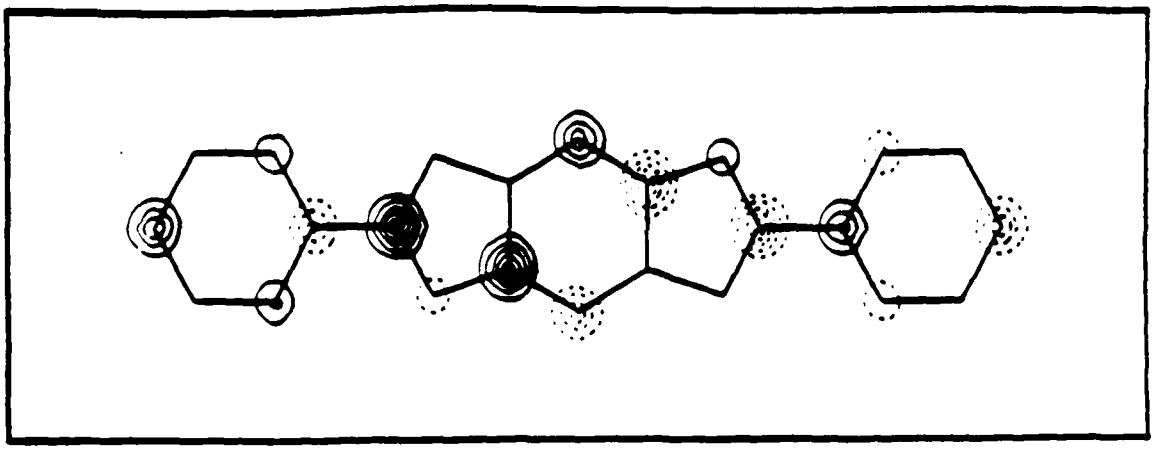

(a)

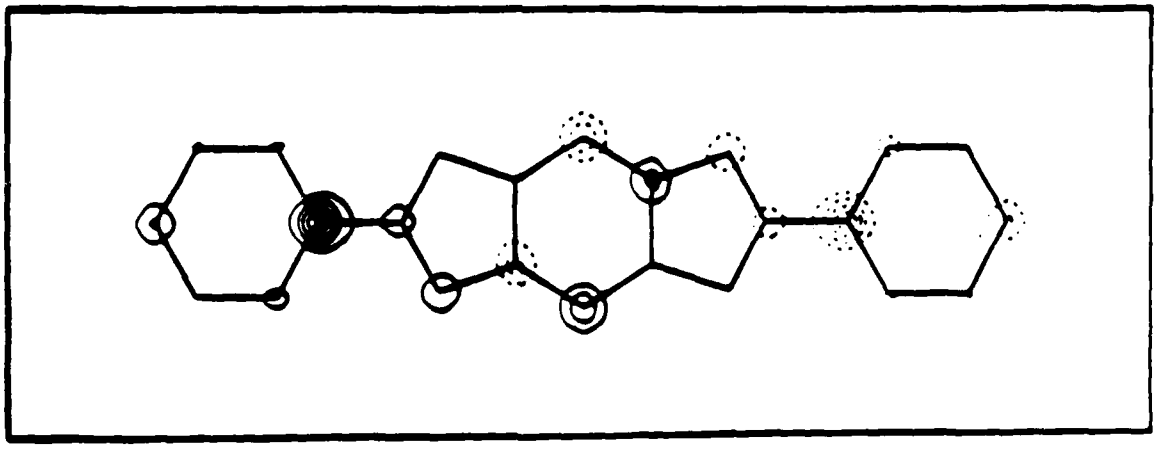

(b)

Figure 2.4.4 Contour diagram of transition density matrix $\rho_{nn'}$ for (a) ^1A_g ground and ^1B_u excited states and (b) ^1B_u one photon and ^1A_g two photon excited states of repeat unit.

V. NONLINEAR OPTICS AND ORIENTATIONAL DISTRIBUTION FUNCTIONS OF NEMATIC LIQUID CRYSTAL PHASES

Relationships between the optical third harmonic susceptibility $\chi^{(3)}_{ijkl}(-3\omega;\omega,\omega,\omega)$ and the nonvanishing order parameters $\langle P_2 \rangle$ and $\langle P_4 \rangle$ for nematic liquid crystals, liquid crystal polymers, and uniaxially aligned polymers have been developed

$$\chi^{(3)}_{zzzz} = N(\delta + 2\xi \langle P_2 \rangle + 8\eta \langle P_4 \rangle) \quad (2.5.1)$$

$$\chi^{(3)}_{xxxx} = N(\delta - \xi \langle P_2 \rangle + 3\eta \langle P_4 \rangle) \quad (2.5.2)$$

$$\chi^{(3)}_{iso} = N\delta \quad (2.5.3)$$

where δ, ξ and η are explicit summations of tensor components of the microscopic susceptibility $\gamma_{ijkl}(-3\omega;\omega,\omega,\omega)$.

Third harmonic generation measurements (Figures 2.5.1 and 2.5.2) were performed on the model system nematic N-(p-methoxybenzylidene)-p-butylaniline (MBBA) using the wedge cell technique as a function of polarization and temperature to demonstrate the simultaneous determination of $\langle P_2 \rangle$ and $\langle P_4 \rangle$ (Figures 2.5.3 and 2.5.4). The results are in agreement with previous experimental results from nuclear magnetic resonance, diamagnetic anisotropy, refractive index, and Raman scattering studies. Thus, we have successfully developed a new theoretical formalism and experimental methodology for understanding and determining the relationships between third order nonlinear optical processes and the orientational distribution functions for nematic liquid crystals, liquid crystal polymers, and uniaxially aligned polymers. Moreover, the formalism and methodology are generalized to large classes of partially ordered phases and to second order nonlinear optical processes.

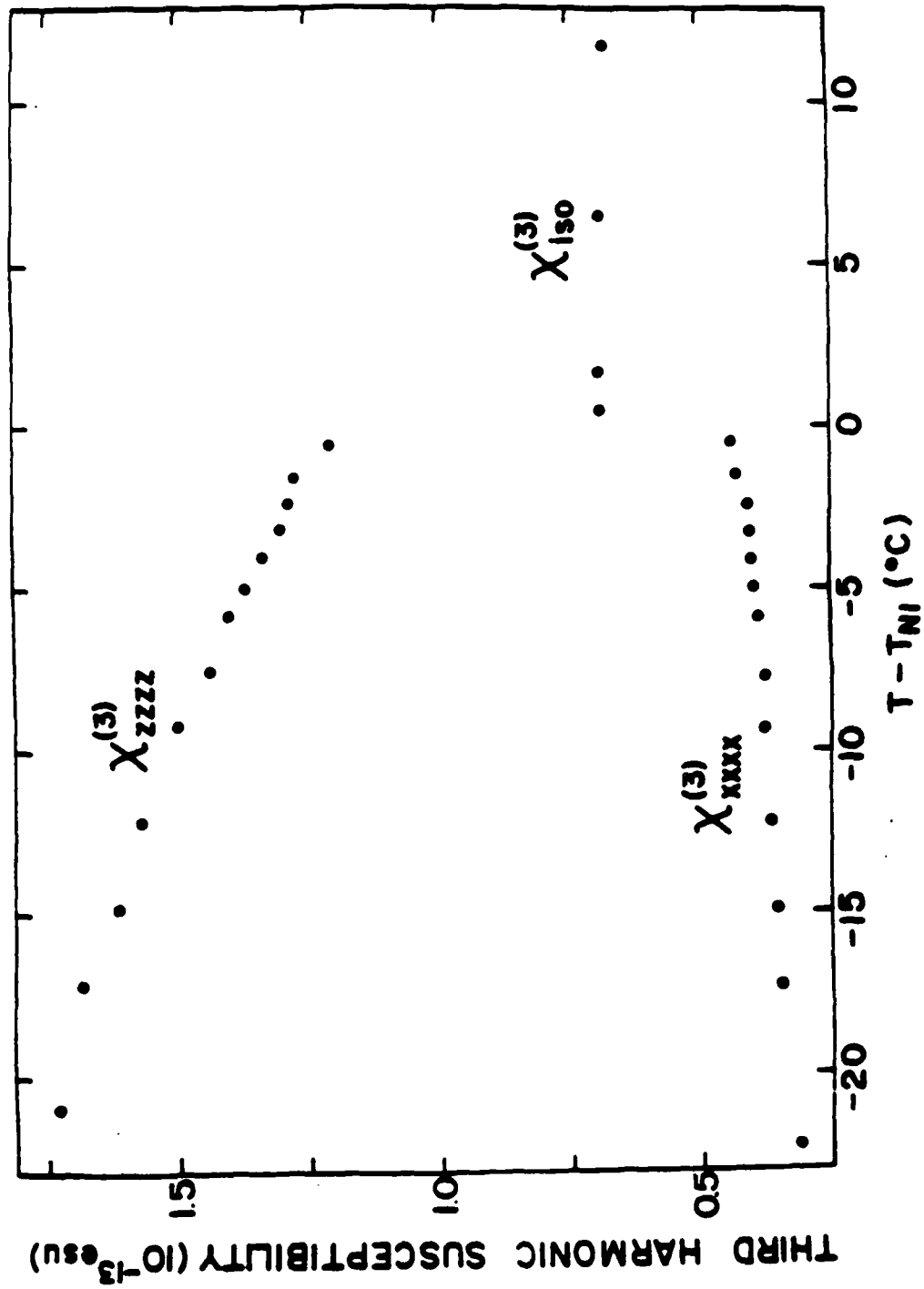
THIRD HARMONIC SUSCEPTIBILITY (10^{-13} esu)
1.5
1.0
0.5
$\chi^{(3)}_{zzzz}$
$\chi^{(3)}_{xxxx}$
$\chi^{(3)}_{iso}$
-20
-15
-10
-5
0
5
10
$T - T_{NI}$ (°C)

Figure 2.5.1

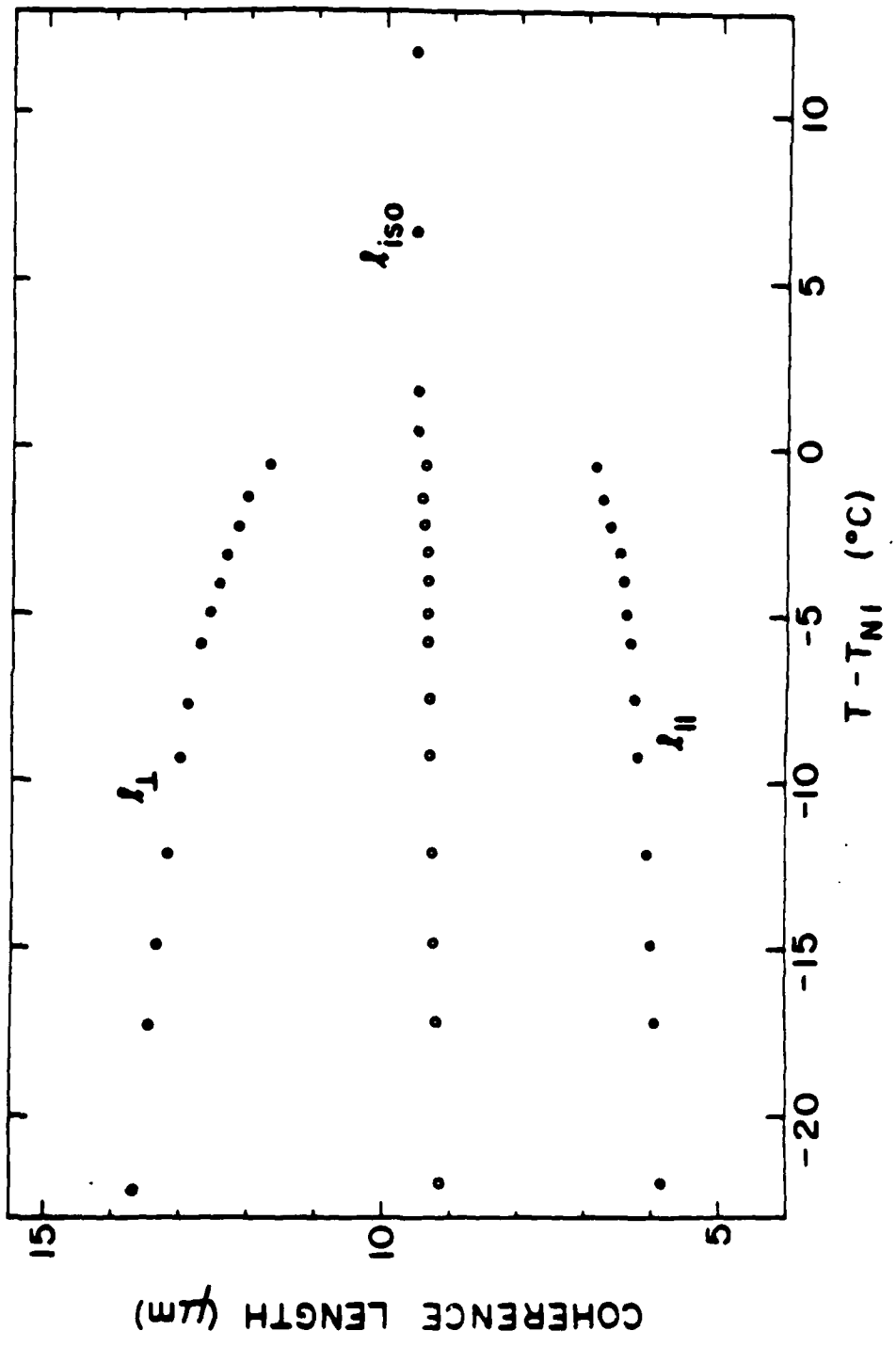
COHERENCE LENGTH (μm)
15
10
5
ℓ_{iso}
ℓ_T
ℓ_{II}
10
5
0
-5
-10
-15
-20
T - T_{NI} (°C)

Figure 2.5.2

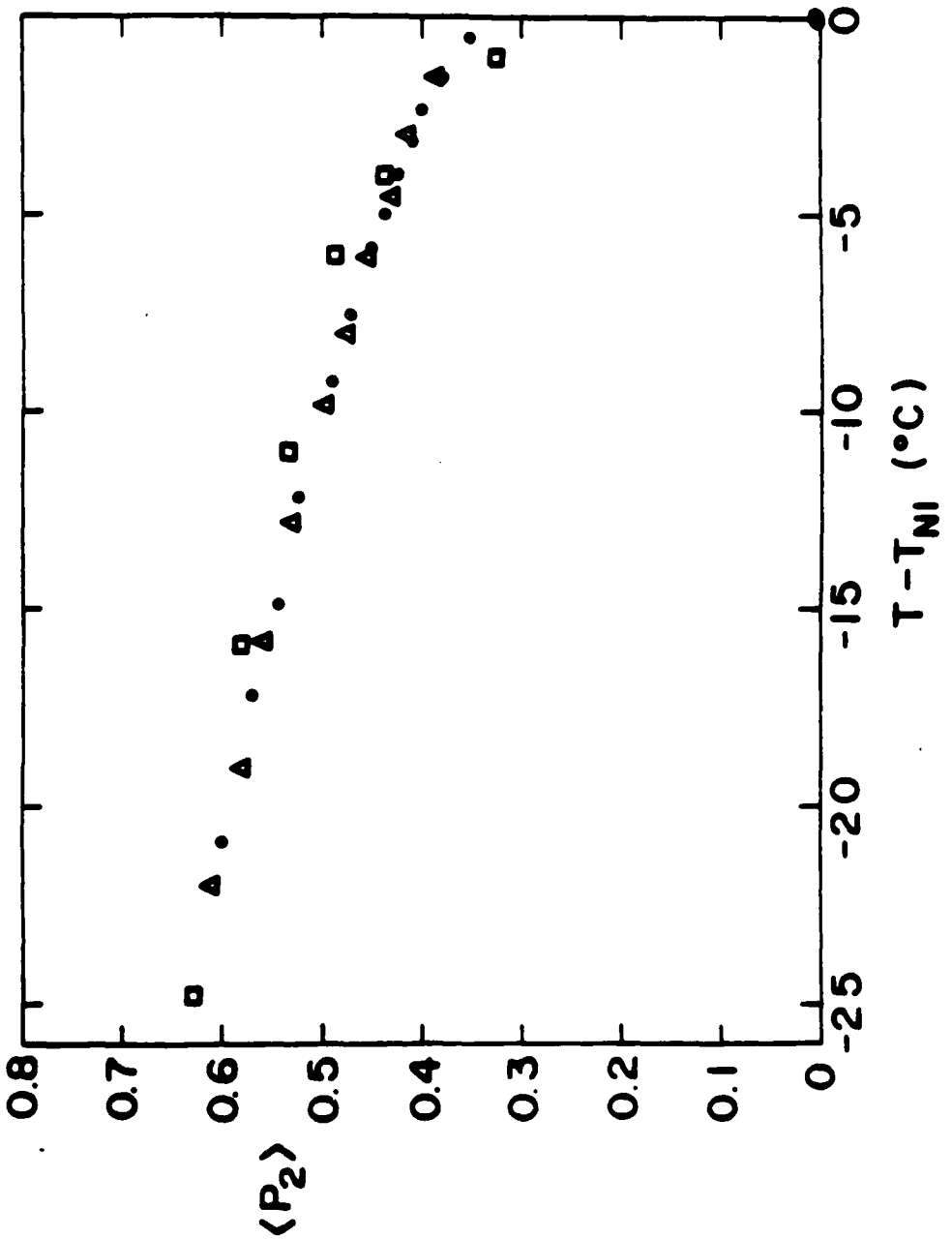

Figure 2.5.3

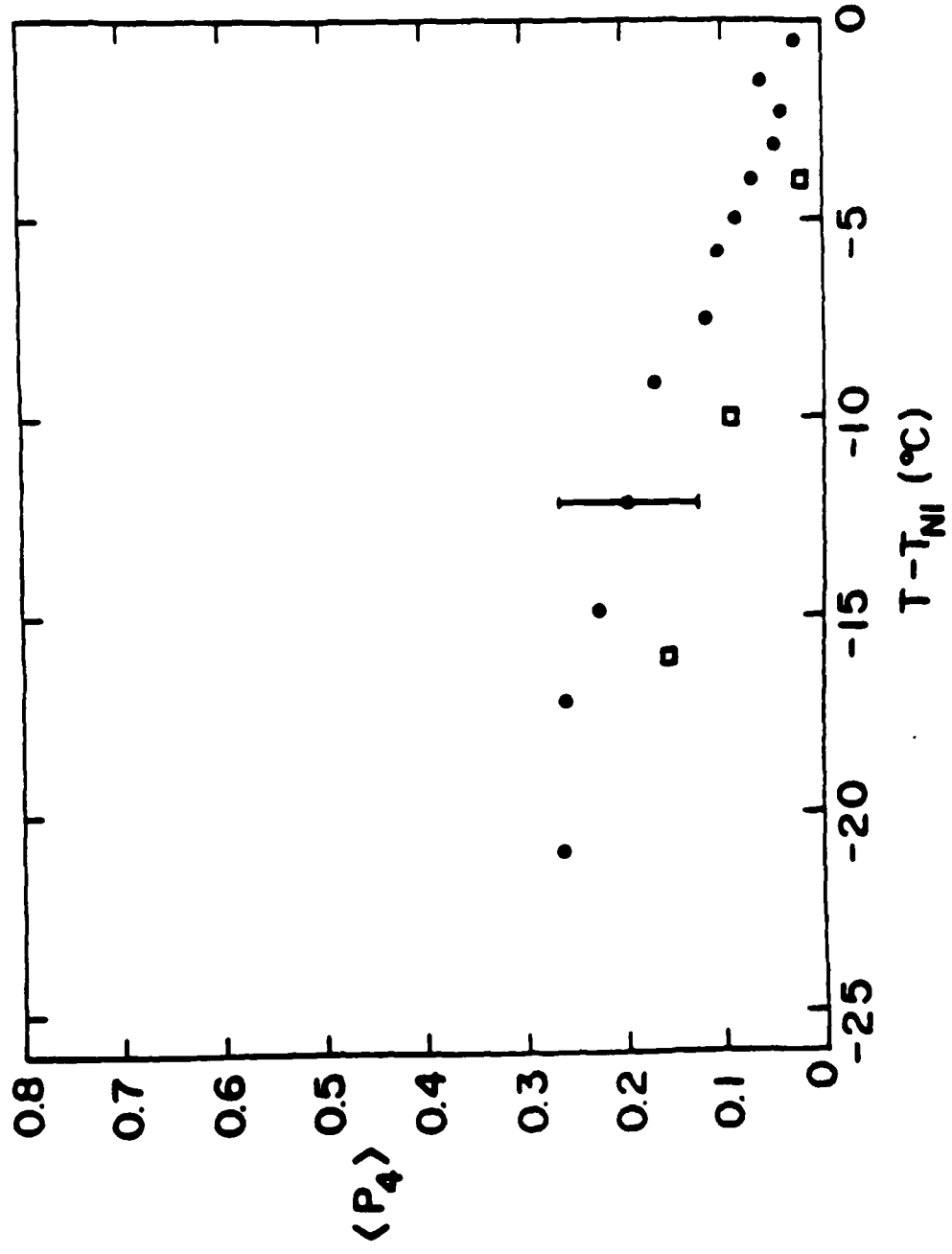

Figure 2.5.4

VI. SECOND HARMONIC GENERATION AT MILLIWATT INCIDENT POWERS IN ORGANIC STRUCTURES

Theoretical and experimental studies have demonstrated the important features of highly charge correlated π-electron states in organic and polymer structures that comprise the microscopic origin of exceptional second order nonlinear optical responses $\chi^{(2)}_{ijk}(-\omega_3;\omega_1,\omega_2)$, particularly as exhibited in second harmonic generation (SHG) and linear electrooptic (LEO) properties. As an important example, we had earlier shown that single crystals of MNA (2-methyl-4-nitroaniline) possess SHG and LEO figures of merit 50 times those of inorganic dielectric insulators such as KDP and 200 times those of semiconductors such as GaAs and that these second order responses are primarily purely electronic at dc and optical frequencies.

More recently we provided detailed theoretical and experimental analyses of the frequency dependent microscopic second order response $\beta_{ijk}(-2\omega;\omega,\omega)$ and the charge correlated π-electron states of MNA. Based on these results, we now report theoretical and experimental results of visually observable phase matched (PM) SHG at low incident power from MNA single crystals. PM SHG measurements at milliwatt incident power were performed on x-y and x-z cut MNA crystals where the x-direction optimizes the microscopic on-site response from the charge correlated p-electron states. For example, for a 60 mm sample interaction length in the x-y configuration, large PM SHG is easily observed at 0.532 μm for incident Nd:YAG (1.064 μm) power as small as 2 milliwatts.

The theoretically calculated PM SHG curves for Type I phase matching shown in Figure 2.6.1a were confirmed by PM SHG experiments at normal incidence (Figure 2.6.1b). The PM SHG curves are represented on a grid of spherical coordinates, θ and ϕ, and the vertical axis is the effective second harmonic component. There is a maximum at the position $\theta = 50.1^\circ$, $\phi = 1.0^\circ$ that was extrapolated to the position $\theta = 51.0^\circ$ and $\phi = 0^\circ$. An MNA crystal was cut and polished such that a polarized fundamental laser beam

at $\lambda = 1.064\ \mu m$ would propagate at this position. The observed PM SHG locus was followed by rotating the crystal through the horizontal and vertical axes.

In addition to fundamental physical understanding, this demonstration of readily observable PM SHG at low incident laser power also serves as proof of principle for applications in optical signal processing, telecommunications, and data storage systems that standardly utilize low power laser diodes as optical sources.

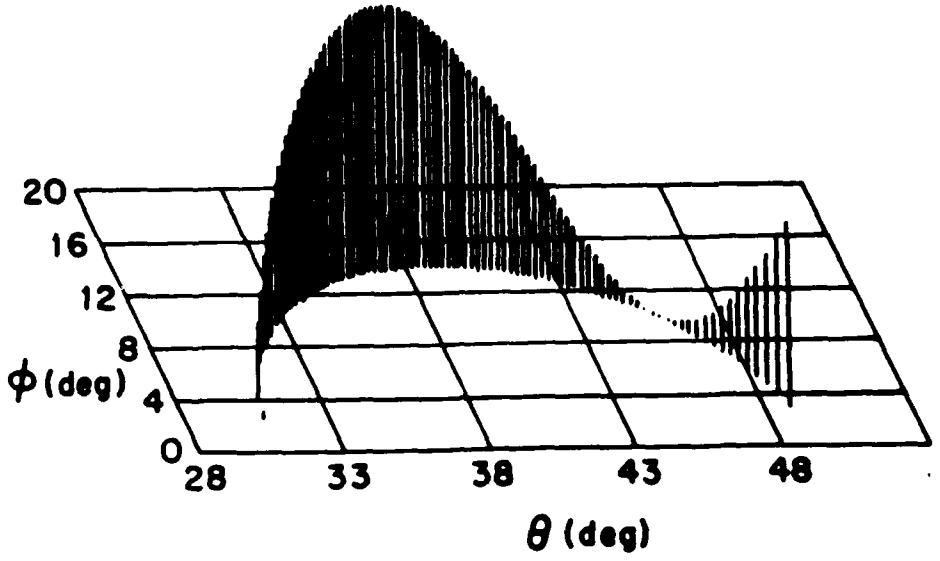

(a)

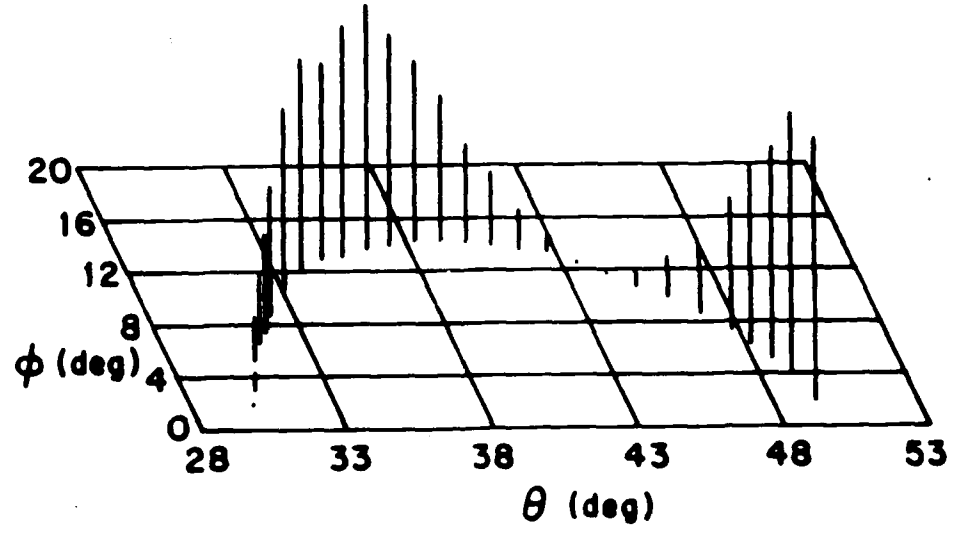

(b)

Figure 2.6.1

VII. TOTAL INTERNAL REFLECTION SPATIAL LIGHT MODULATOR USING ORGANIC ELECTROOPTIC CRYSTAL MNA.

Nonlinear optical organic and polymeric materials, with their exceptionally large nonlinear optical susceptibilities, are superior in many aspects to commonly used inorganic materials. This clearly has provided an exciting prospect for their application in optical devices. To give an initial assessment of the implementation of these organic materials in real devices, we have performed a thorough study of an optical signal processing device, namely, the total internal reflection (TIR) spatial light modulator (SLM) and compare the results with the performance characteristics of this device based on a standard inorganic material as the active medium. The comparison was made between crystal MNA (2-methyl-4-nitroaniline), a well characterized organic electrooptic and nonlinear optical material, and $LiNbO_3$, a widely employed inorganic electrooptic crystal.

The basic structure of TIR SLM is shown in Figure 2.7.1. The device consists of a VLIC integrated circuit having serial-to-parallel addressing electronics that provide data to several thousand drive transistors which then connect to several thousand parallel electrodes on the surface of the chip. This chip is pressed against an electrooptic crystal so that fringing fields existing between electrodes are proximity coupled into the crystal (Figure 2.7.2). These fringing fields change the index of refraction of the crystal through the linear electrooptic effect. To interact with these fringing fields, the device is illuminated with a sheet of light which is collimated in the horizontal axis and brought to a sheet focus on the surface. As the light approaches this surface and recedes from this surface, it picks up a phase shift dependent on the index of refraction change produced by the fringing electric fields. By using a standard Schlieren imaging system, this phase modulated profile can be converted into an optical image intensity profile.

Performance of the TIR SLM is evaluated for MNA and $LiNbO_3$ using reported electrooptic coefficients. Our results demonstrate that to induce the same values of optical phase modulation, the required driving voltage for a TIR device using MNA as the

modulator crystal is reduced by approximately a factor of 2.5, compared with that using $LiNbO_3$ as modulator crystal. Correspondingly, under the same driving voltage pattern, the diffraction efficiency will be enhanced by a factor of more than six for a TIR device using MNA as compared with that using $LiNbO_3$ as modulator crystal. These results for MNA also show that poled electrooptic polymers, which are formed basically to emulate MNA crystals but in polymer form, can additionally be implemented in TIR SLM configurations with figures of merit comparable to and greater than those of an MNA based SLM.

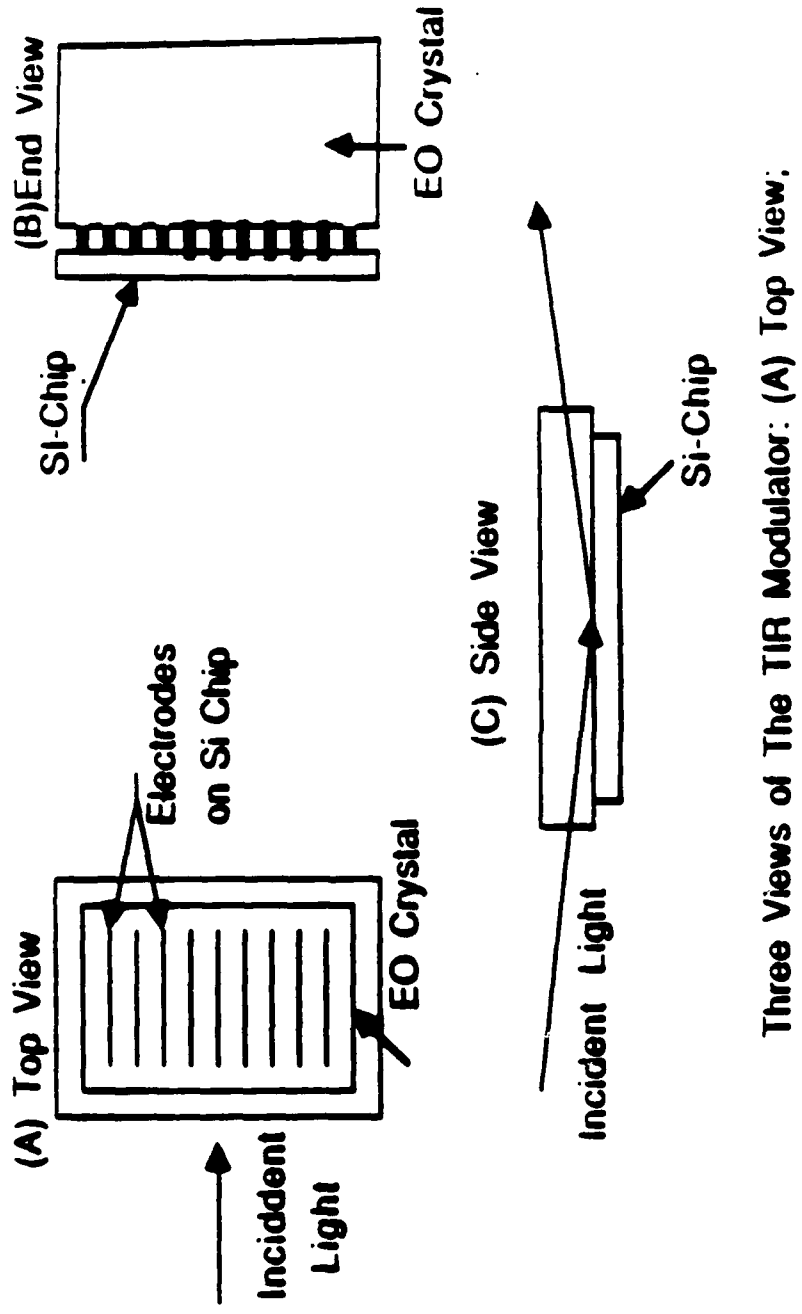

Three Views of The TIR Modulator: (A) Top View;

(B) End View; (C) Side View

Figure 2.7.1

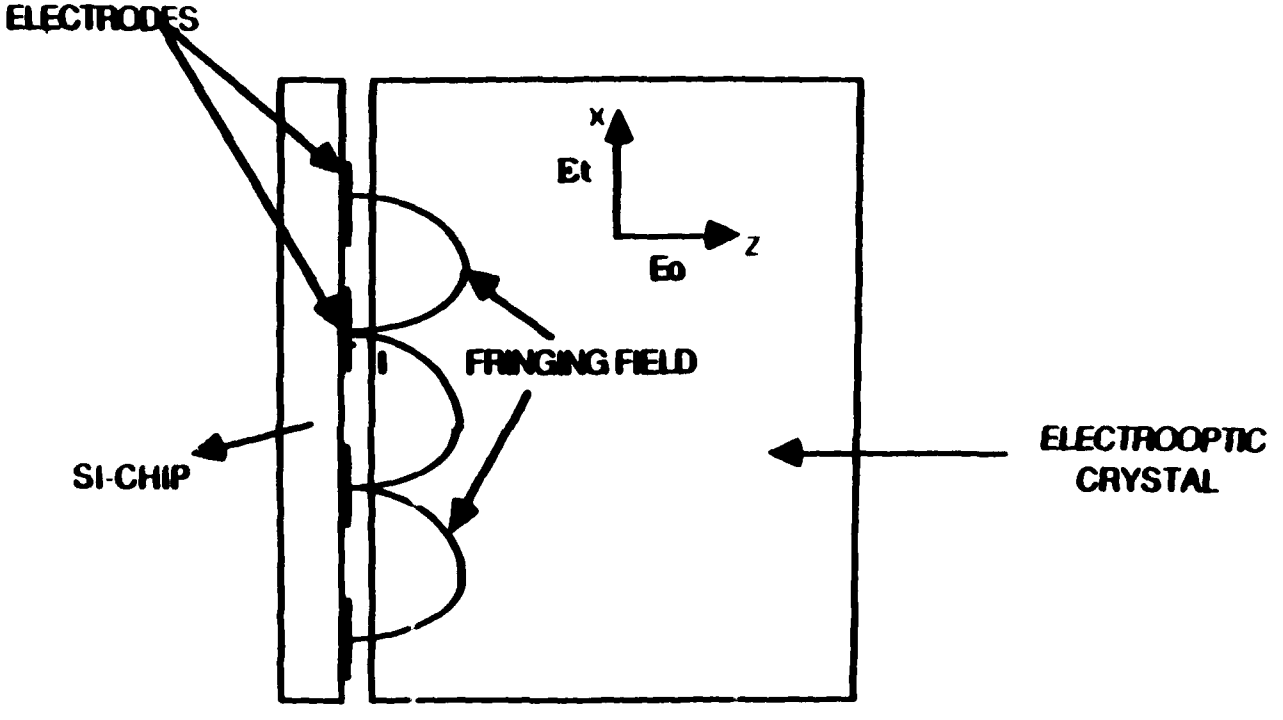

Figure 2.7.2

CRYSTAL/SI-CHIP INTERFACE AND THE FRINGING FIELD

VIII. SYMMETRY-CONTROLLED ELECTRON CORRELATION MECHANISMS OF THIRD ORDER NONLINEAR OPTICAL PROPERTIES OF CONJUGATED LINEAR CHAINS

Third order nonlinear optical polarizations created by interactions between intense laser fields in optical media result in a large variety of self-action phenomena that are important to fundamental physics and materials research as well as optical device technologies. Self-action effects are the basis for controlling light by light in its propagation, polarization, amplitude, and frequency. Important examples include harmonic generation, self-phase modulation, phase conjugate wave generation, and processes such as optical bistability that are important to optical signal processing and data storage.

It is well established that conjugated organic and polymer structures exhibit unusually large, ultrafast third order nonlinear optical properties. These properties arise from virtual p-electron excitations occurring within condensed assemblies of individual molecular, or polymer chain, sites which act as macroscopic sources of nonlinear optical response. However, until the present study, no suitable fundamental understanding existed for these unusual third order properties.

This year through a series of experimental and theoretical studies, we have successfully developed a microscopic description of the mechanism and a corresponding set of physical principles for understanding third order virtual excitation processes that occur in the p-electron states of conjugated linear chains such as polyenes and polyenynes (Figure 2.8.1). We have shown that symmetry controlled correlation effects determine the properties and behavior of the third order nonlinear optical susceptibilities of these structures. The highly correlated nature of the third order virtual excitations for the third harmonic susceptibility $\gamma_{xxxx}(-3\omega;\omega,\omega,\omega)$ for example, is directly represented by contour diagrams of transition density matrices $\rho_{nn'}$. Contour diagrams for $\rho_{nn'}$ of the ground state and highly electron correlated 6^1A_g state with the dominant first one photon 1^1B_u state are shown in Figure 2.8.1 where solid and dashed lines correspond to opposite signs of $\rho_{nn'}$. The contour diagram of $\rho_{g,1^1B_u}$ shows the $g \rightarrow 1^1B_u$ transition results in a

modulated charge redistribution and, correspondingly, a relatively small contribution to γ_{xxxx}. In sharp contrast, $\rho_{6^1A_g, 1^1B_u}$ for the virtual transition between the 6^1A_g and 1^1B_u states produces a large charge separation along the x-chain axis direction and an associated large transition moment of 13.2D that dominates the contributing term to γ_{xxxx}.

The calculated dispersion curve for $\gamma_{xxxx}(-3\omega;\omega,\omega,\omega)$ for a principle example of octatetraene (OT) having eight carbon atom sites (N) is shown in Figure 2.8.1. Over the near infrared and visible ranges, a first peak at 1.47 eV (λ = 0.84 μm) appears due to the 3ω resonance of the 1^1B_u state, and a second peak at 2.08 eV (λ = 0.60 μm) is from the 2^1A_g state which is significant on-resonance even though it makes a very small contribution off-resonance.

The general features of the origin of $\gamma_{ijkl}(-3\omega;\omega,\omega,\omega)$ for OT just described are common to all the chain lengths from N = 4 to 16. Importantly, there is a unifying general result that at fixed frequency, γ_{xxxx} for differing chain lengths exhibits a dramatic but well-defined increase with increased chain length. The theoretical values for γ_{xxxx} at a fundamental photon energy of 0.65 eV (λ = 1.907 μm) are plotted against the number of carbon atom sites N on a log-log scale in Figure 2.8.2 and exhibit a power law dependence upon N with an exponent of 5.4 which results from three length-dependent factors. With increased chain length, there are lower excitation energies, larger transition dipole moments, and increased number of contributing excited state terms.

In summary, we have developed a microscopic mechanism for third order nonlinear optical properties of conjugated linear chains that allow detailed identification of the significant contributions to any third order process. Such a microscopic description further allows development of guidelines for the molecular design of new organic nonlinear optical materials.

MICROSCOPIC ORIGIN OF $\gamma(-3\omega;\omega,\omega,\omega)$ FOR LINEAR CONJUGATED CHAINS

SYMMETRY	ENERGY (eV)	$\mu_{nn'}$(D)
$6\,^1A_g$	7.16	(13.2)
$1\,^1B_u$	4.42	7.8
$2\,^1A_g$	4.15	(2.8)
$1\,^1A_g$		

OT

- $\gamma_{xxxx}(-3\omega;\omega,\omega,\omega,\omega) = 15.5 \times 10^{-36}$ esu
  $\gamma_L(-3\omega;\omega,\omega,\omega) = 3.4 \times 10^{-36}$ esu (ω: 0.65 eV/$\hbar$)
- ONLY CONTRIBUTIONS: $g \rightarrow {}^1B_u \rightarrow {}^1A_g \rightarrow {}^1B_u \rightarrow g$
- ^1A_g STATES: THOSE WITH LARGEST $\mu_{nn'}$ WITH DOMINANT ^1B_u STATE
- 2 PHOTON ^1A_g STATES CRITICAL IN THIRD ORDER PROCESSES

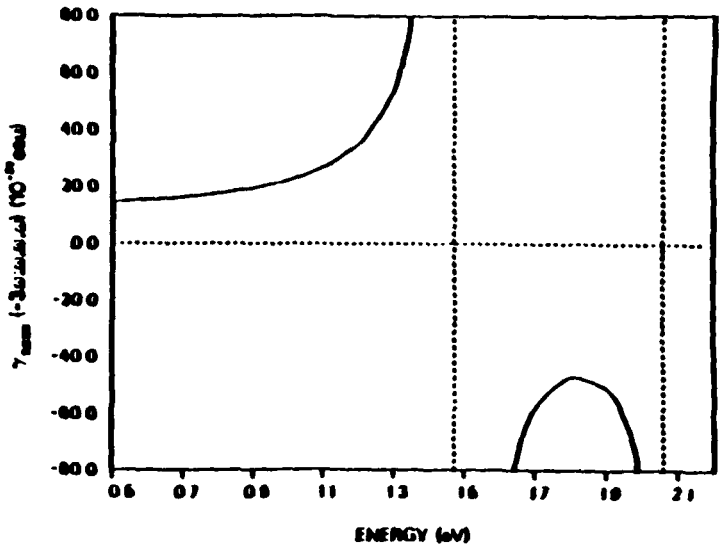

TRANSITION DENSITY MATRIX DIAGRAMS

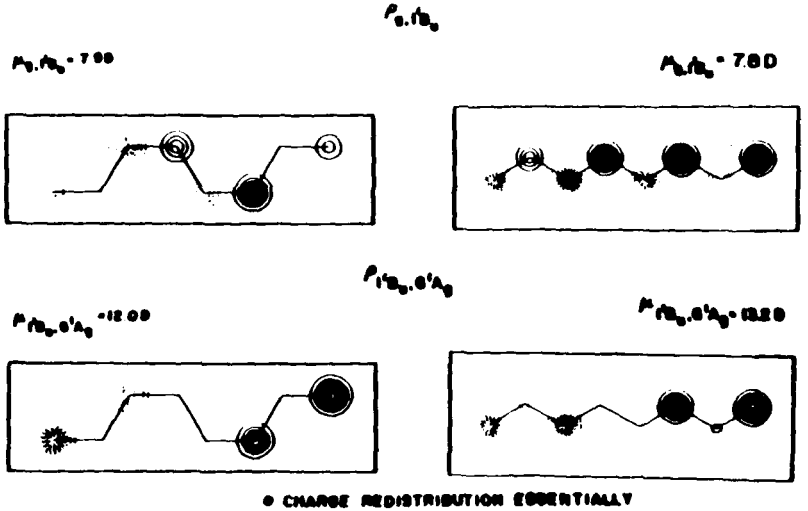

- CHARGE REDISTRIBUTION ESSENTIALLY THE SAME FOR cis AND trans CONFORMATIONS

Figure 2.8.1

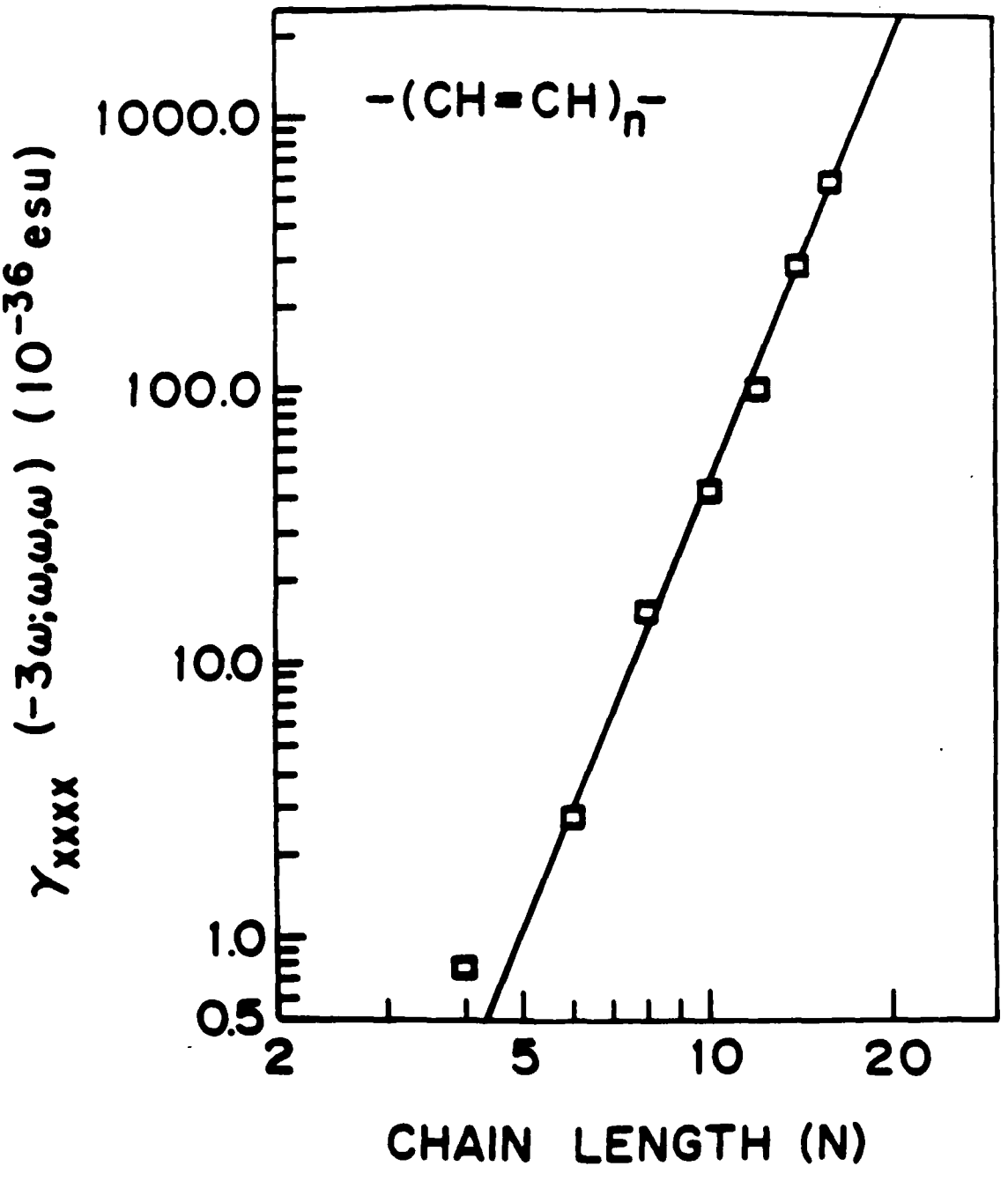
-(CH=CH)n-
1000.0
100.0
10.0
1.0
0.5
2
5
10
20
γxxxx (-3ω;ω,ω,ω) (10-36 esu)
CHAIN LENGTH (N)

Figure 2.8.2

IX. HIGH RESOLUTION STRUCTURAL STUDIES OF ULTRATHIN MULTILAYER FILMS CONTAINING A DISUBSTITUTED DIACETYLENE POLYMER

Disubstituted diacetylenes can be polymerized in the solid state to form long-chain polymers. The extended π-electron system of the conjugated polymer is highly polarizable, and the excited π-electron states give rise to extremely large microscopic nonlinear optical susceptibilities. These microscopic susceptibilities can result in large macroscopic nonlinear optical properties, which mediate the observed nonlinear optical processes of the material medium. Recently, interest has centered on nonlinear optical properties of Langmuir-Blodgett multilayer films of amphiphilic disubstituted diacetylenes because such films provide ordered polymer structures in ultrathin film forms.

We have recently completed high-resolution x-ray scattering structural studies on both periodic and nonperiodic ultrathin multilayer films containing from one to five bilayers, each bilayer of either arachidic acid or pentacosa-10,12-diynoic acid (a disubstituted diacetylene monomer). The monomer was UV-polymerized in the films into either its blue form "DAPb" or its red form "DAPr". Some of the results are summarized in Figure 2.9.1 below.

The figure presents a schematic view of our current knowledge of the structure of periodic, ultrathin multilayer films containing a disubstituted (poly) diacetylene. The double lines running parallel to the plane of the multilayer are intended to represent the backbone of the extended polyene chain, which links adjacent monomeric units together. The first deposited monolayer is depicted as being composed of well-ordered all-trans hydrocarbon chains with their methyl ends distributed over a small distance δ_1 along the z-axis. Once a bilayer has been deposited, the underlying OTS layer is shown as disordered via chain configurations containing "kinks" and "jogs" in such a way that the variable C_{18} chain lengths accommodate the "rough" class surface. The average tilt angle t of the hydrocarbon chain axis, relative to the normal to the layer plane is $\sim 35^{\circ}$ for DAPb and $\sim 0^{\circ}$ for DAPr. Each interior bilayer for the DAPb multilayer is shown as containing well-

ordered, essentially all-trans chains with a small spread of the position of the methyl end groups along the z-axis of δ_1. As a result, the interlayer ordering in both periodic and nonperiodic multilayer films containing DAPb is long-range. The interior bilayers of the DAPr multilayer are shown as having well-ordered all-trans carboxyl end side-chains, while the methyl end side-chains are disordered via "kinks" and "jogs" with their methyl end groups spread over a larger length δ_2. As a result, the interlayer ordering in both periodic and nonperiodic multilayer films containing DAPr is only short-range. The last monolayer is shown with significant disorder of the hydrocarbon chains distributing the methyl end groups over a much larger length e along the z-axis. The double lines representing the polyene backbone are shown as dashed lines for the last monolayer as the degree of disorder may reduce the extent of polymerization.

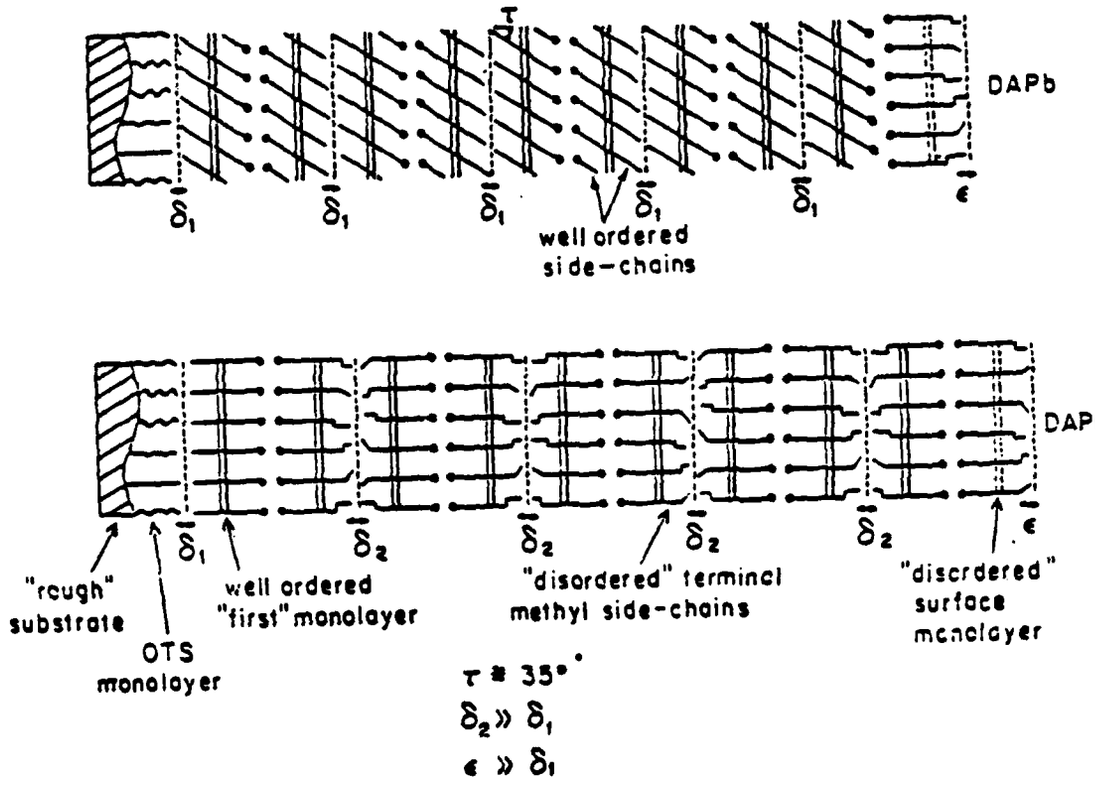
τ
DAPb
δ1
δ1
δ1
δ1
δ1
ε
well ordered
side-chains
DAPr
δ1
δ2
δ2
δ2
δ2
ε
"rough"
substrate
OTS
monolayer
well ordered
"first" monolayer
"disordered" terminal
methyl side-chains
"disordered"
surface
monolayer
τ ≅ 35°
δ2 » δ1
ε » δ1

Figure 2.9.1

X. FREQUENCY DEPENDENCE OF THE OPTICAL KERR EFFECT AND THIRD ORDER ELECTRONIC NONLINEAR OPTICAL PROCESSES OF ORGANIC SYSTEMS.

Self-action effects in third order nonlinear optical processes provide the basis for controlling light with light and are, thereby, important to both fundamental physics and optical device technologies. Third order nonlinear optical processes include third harmonic generation, optical Kerr effect, phase conjugate wave generation, and optical bistability.

In material media, mechanisms involving electronic, lattice, and thermal excitations all contribute in experimental determinations of macroscopic $\chi^{(3)}_{ijkl}$. These contributions occur over a broad frequency range extending from the near infrared to the ultraviolet. Highly precise experimental methods are therefore required for accurately determining each term possibly contributing in a $\chi^{(3)}_{ijkl}$ experiment. Third harmonic generation (THG) for example, measures only the electronic term and is severely limited in frequency range because either the fundamental, the generated wave, or both often are absorbed by nearby one or two photon resonances. Degenerate four wave mixing (DFWM) configurations are fixed, single frequency measurements, and the output signal includes all contributing terms that are not resolved unambiguously even down to subpicosecond timescales. Thus, $\chi^{(3)}_{ijkl}$ values determined by THG or DFWM methods are severely limited and oftentimes unreliable.

We have developed new experimental methods based on the frequency dependence of the optical Kerr effect and nonlinear optical interferometry for accurately determining the magnitude, sign, and dispersion of $\chi^{(3)}_{ijkl}$. This year we have completed an extensive series of experimental and theoretical studies of the frequency dependent optical Kerr effect that enables frequency dependent $\chi^{(3)}_{ijkl}$ results to be accurately obtained from optimized pump-probe techniques.

The optical Kerr effect (OKE) is a four wave mixing process in which an intense optical pump beam of frequency ω_1 induces depolarization in a probe beam of frequency

ω_2 because of the third order nonlinear optical polarization, $P_i^{(3)}(\omega_2)$. In an isotropic medium, $P_i^{(3)}(\omega_2)$ is expressed as

$$P_i^{(3)}(\omega_2) = \chi_{ijkl}^{(3)}(-\omega_2;\omega_1,-\omega_1,\omega_2)\, E^{\omega_1} E^{\omega_1} E^{\omega_2} \qquad (2.10.1)$$

where $\chi_{ijkl}^{(3)}$ is the third order nonlinear optical susceptibility and E^{ω_1} and E^{ω_2} are the pump and probe fields respectively. At frequencies well above molecular vibration and rotation modes but below electronic resonances, $\chi_{ijkl}^{(3)}(-\omega_2;\omega_1,-\omega_1,\omega_2)$ has contributions due to both electronic excitations and lattice displacements which in the Born-Oppenheimer approximation is expressed as the sum of the quantum averages σ_{ijkl} and d_{ijkl},

$$\chi_{ijkl}^{(3)} = \sigma_{ijkl} + d_{ijkl} \qquad (2.10.2)$$

where σ_{ijkl} and d_{ijkl} are the third order electronic and lattice contributions, respectively; both terms are assumed to be fast relative to experimental time scales. In such a frequency regime, because of nearby electronic resonances at higher frequency, the dominant frequency-dependent term is the ultrafast electronic contribution, and, hence, frequency-dependent measurements of the total OKE response allow direct determination of the electronic and lattice contributions to $\chi^{(3)}$ from OKE data alone.

In our experimental studies, the OKE coefficient is measured utilizing a pump-probe configuration with the pump and probe beam polarization oriented at 45° with respect to each other (see Figure 2.10.1). The pump beam induces a refractive index anisotropy in the Kerr medium, thus resulting in a rotated elliptical polarization for the probe beam. The polarization change is detected using an appropriate arrangement of cross polarizers. In the experiment, the pump beam employed is a pulsed Nd:YAG laser (1.064 μm) while the

probe beam is an argon ion laser or a cw ring dye laser to permit tunability and thus facilitating a dispersion measurement. An optical gate system was designed to reduce the background noise to the PMT detector system due to the cw source.

The frequency dispersion of the OKE susceptibility $\chi^{(3)}_{ijkl}(-\omega_2;\omega_1,-\omega_1,\omega_2)$ was measured for a number of systems. Results for the model Kerr liquids benzene and nitrobenzene are shown in Figure 2.10.2 . In general, the $\chi^{(3)}_{ijkl}(-\omega_2;\omega_1,-\omega_1,\omega_2)$ is composed of a resonant term and a nonresonant term. The resonant term is due to the two-photon resonance of the sum $(\omega_1+\omega_2)$ or difference $(\omega_1-\omega_2)$ frequency of the pump (ω_1) and probe (ω_2) beam, while the nonresonant term is in part due to the molecular reorientation contribution. We have demonstrated for the first time that since the experiment measures the absolute value of the $\chi^{(3)}_{ijkl}(-\omega_2;\omega_1,-\omega_1,\omega_2)$, interference between the resonant and the nonresonant terms gives rise to a characteristic Fano-like resonance peak, as can be seen in the experimental data of Figure 2.10.2. From comparison with gas phase linear absorption data and theoretical calculations of $\chi^{(3)}_{ijkl}(-\omega_2;\omega_1,-\omega_1,\omega_2)$ the observed dispersion data can be thoroughly understood and the resonant electronic contribution determined. OKE measurements have the principal advantage that since both the pump and the probe frequencies are far off resonance, negligible single photon absorption occurs and there is little or no depletion of either beam. This allows a thorough study of the resonant electronic contributions to $\chi^{(3)}_{ijkl}(-\omega_2;\omega_1,-\omega_1,\omega_2)$.

In summary, an experimental and theoretical study of OKE dispersion in isotropic media has been developed. A theoretical analysis based on Maxwell's equations provides the connection between experimentally measured quantities and $\chi^{(3)}_{ijkl}(-\omega_2;\omega_1,-\omega_1,\omega_2)$. An optimized pump-probe depolarization technqiue was developed, and conventional theoretical approximations thoroughly studied. The OKE dispersion data is used to determine the electronic and lattice contributions to $\chi^{(3)}_{ijkl}(-\omega_2;\omega_1,-\omega_1,\omega_2)$ near sum-frequency electronic resonances and can show the relative strength of the electronic term,

σ_{ijkl}, from different excited states. The dispersion results for π-electron systems with electronic transitions probed in the presence of a continuum background provided the first observation of a characteristic Fano-like peak due to interference between resonant and nonresonant terms. The general formalism presented in this study can be adopted for the study of resonant and nonresonant $\chi^{(3)}$ processes in any other media of interest; and, the experimental data can be compared to microscopic description based upon many-electron theory and calculations.

Experimental layout where HWP1 is a half wave plate at 1.06μm, P1 and P2 polarizers, A1 and A2 analizers, BS1 and BS2 beamsplitters, MDM1 and MDM2 a motor driven mirror, KDP a KDP mixing crystal, PD a photodiode, F1 and F2 filters and PMT's are photomultiplier tubes.

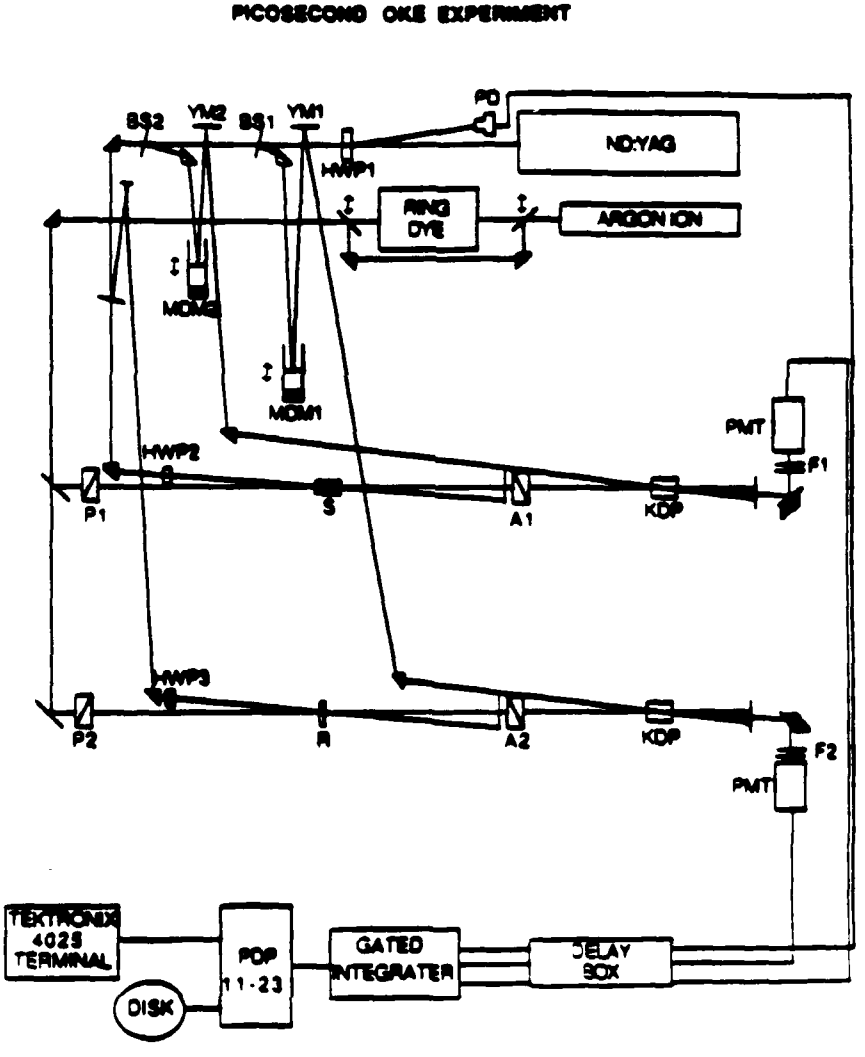

Figure 2.10.1

Dispersion data for nitrobenzene is given by the solid points (scale on left ordinate) and benzene data is given by the open points (scale on right ordinate).

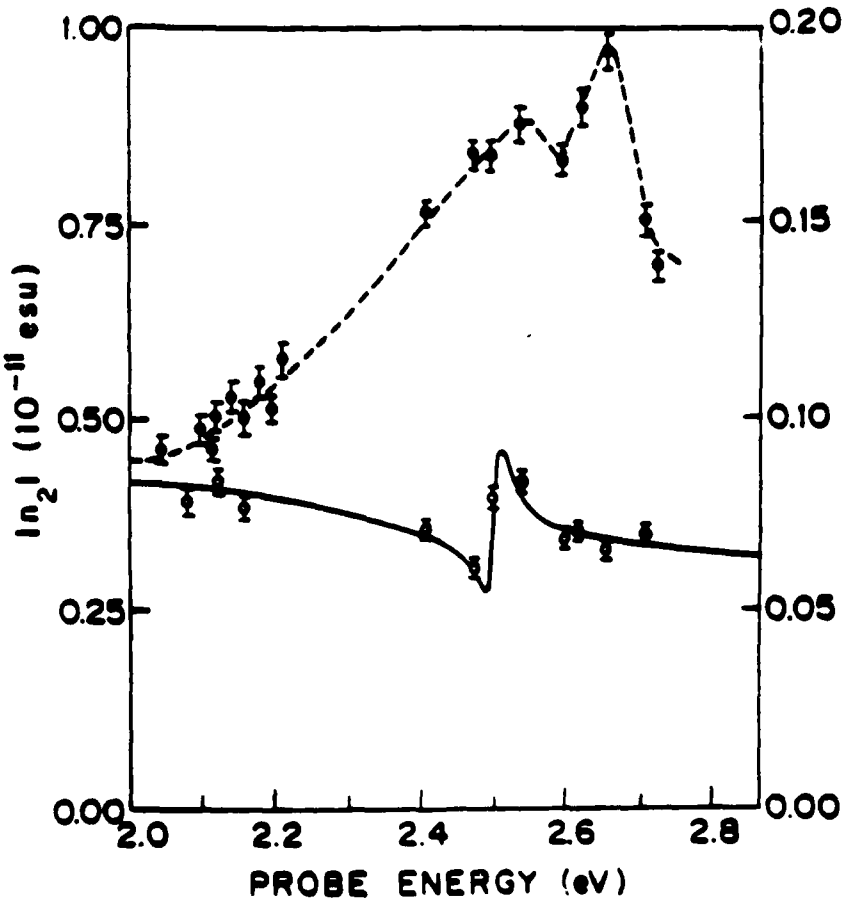

Figure 2.10.2

XI. TUNABLE COHERENT LASER SOURCE FROM STIMULATED ROTATIONAL RAMAN SCATTERING

We have completed a detailed study of stimulated rotational Raman scattering (SRRS) using a Nd:YAG laser and demonstrated that it can be used as a convenient, low cost coherent light source from 0.4 μm to 2.2 μm. Stimulated Raman scattering (SRS) is widely used to frequency shift the 1.064 μm output from the Nd:YAG laser using, for example, hydrogen gas where the vibrational excited state provides an energy shift of 4155 cm^{-1} that results in four additional coherent sources in the visible and near infrared regions (1.907, 0.737, 0.564 and 0.457 μm). The rotational Raman shift, being much smaller in energy, results in more closely spaced lines. The rotational level spacing ΔE of a diatomic molecule can be obtained by considering a quantum vibrating rotator, and is given approximately by the expression

$$\Delta E = [B_e - \alpha_e(v+1/2)]J(J+1) - [D_e - \beta_e(v+1/2)]J^2(J+1)^2 \qquad (2.11.1)$$

where J is the total angular momentum, v the oscillator quantum number, and B_e, α_e, D_e and β_e are constants for the molecule. With the selection rule ΔJ=2, the energy spacing for the rotational levels is 586.9 cm^{-1}. This effect, in combination with the vibrational Raman lines, produces closely spaced discrete lines spanning from 0.4 mm in the visible to 2.2 μm in the near infrared.

A high power pulsed Nd:YAG laser was used to pump a high pressure H_2 gas cell. With the appropriate input polarization up to five Stoke lines can be easily observed using a moderate input power. This effect, together with the vibrational Raman lines produces more than 20 discrete, well-defined new frequency lines in the visible-near infrared region using only a single frequency pump source. In one demonstration, we have utilized these SRRS lines in measurements of the dispersion of second and third harmonic generation in organic systems. Results of experimental studies of the power dependence of the SRRS

lines at various frequencies on gas pressure, polarization, and power of the input source are shown in Figures 2.11.1 to 2.11.3. The simplicity and reliability of SRRS makes it a convenient, low cost, tunable source of visible and near infrared coherent radiation. The ease of operation, for instance, may be important to issues of sensor protection.

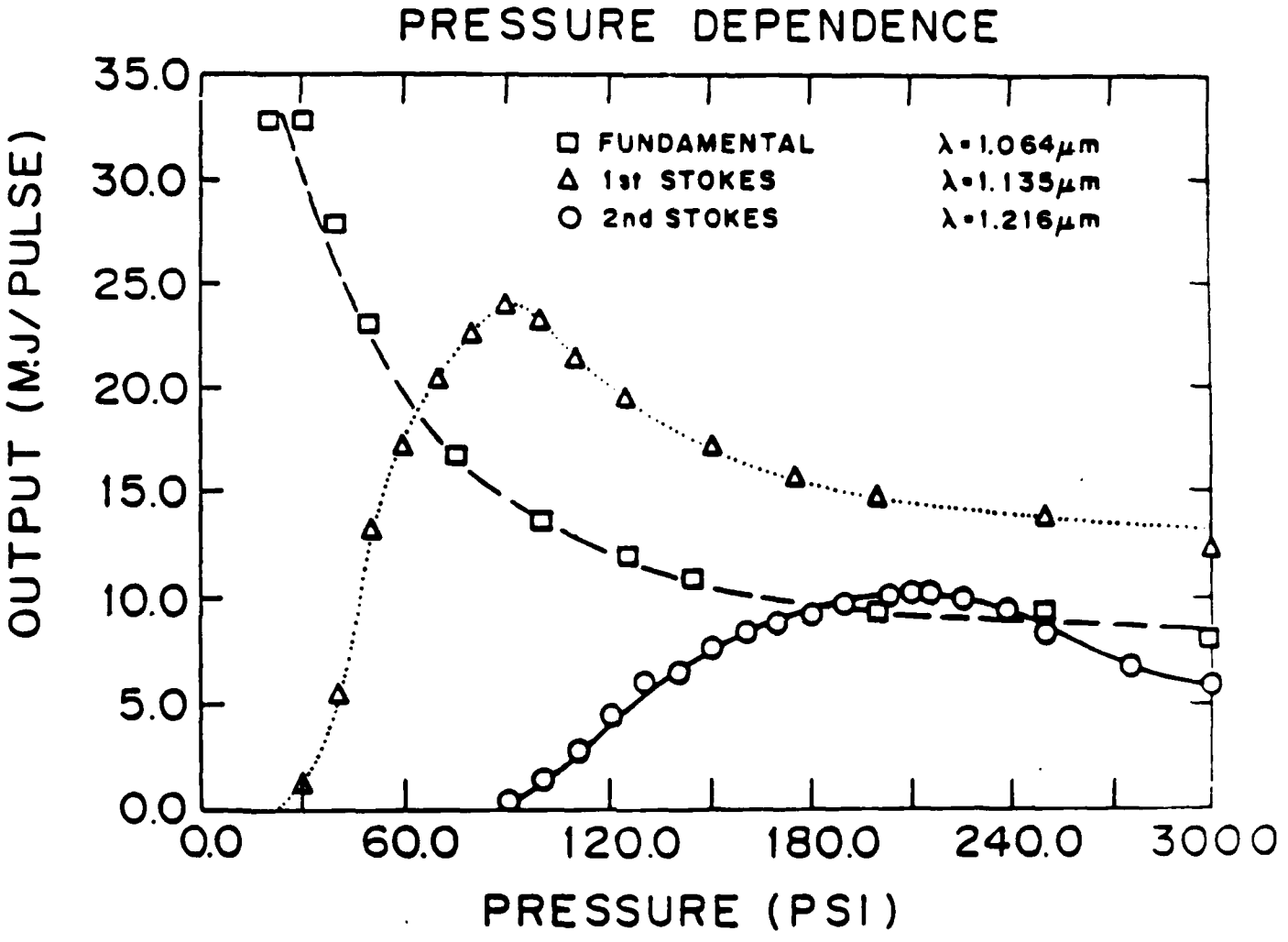
PRESSURE DEPENDENCE
FUNDAMENTAL λ=1.064μm
1st STOKES λ=1.135μm
2nd STOKES λ=1.216μm
OUTPUT (MJ/PULSE)
35.0
30.0
25.0
20.0
15.0
10.0
5.0
0.0
0.0
60.0
120.0
180.0
240.0
300
PRESSURE (PSI)

Figure 2.11.1

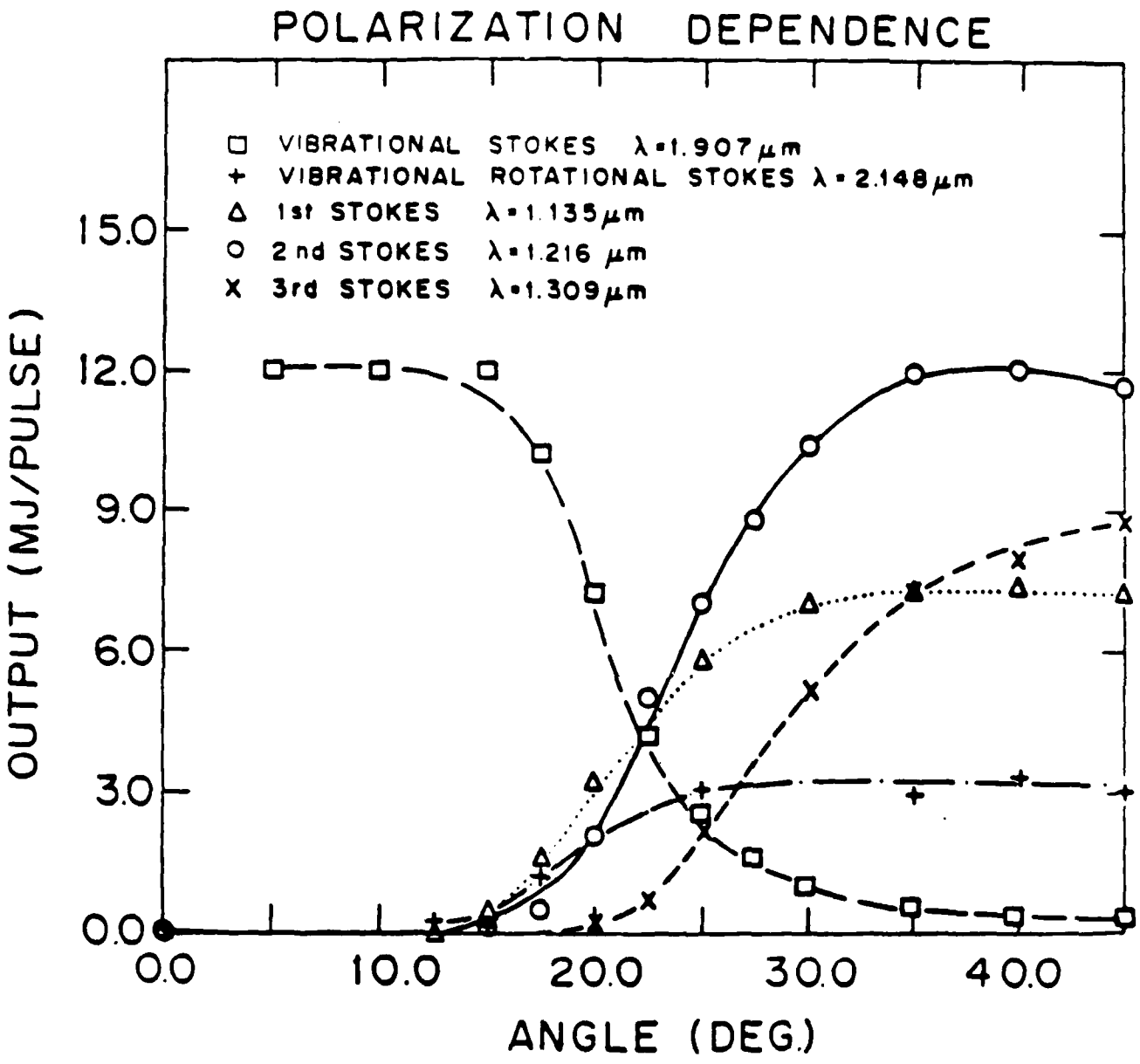
POLARIZATION DEPENDENCE
VIBRATIONAL STOKES λ=1.907μm
VIBRATIONAL ROTATIONAL STOKES λ=2.148μm
1st STOKES λ=1.135μm
2nd STOKES λ=1.216 μm
3rd STOKES λ=1.309μm
OUTPUT (MJ/PULSE)
15.0
12.0
9.0
6.0
3.0
0.0
0.0
10.0
20.0
30.0
40.0
ANGLE (DEG.)

Figure 2.11.2

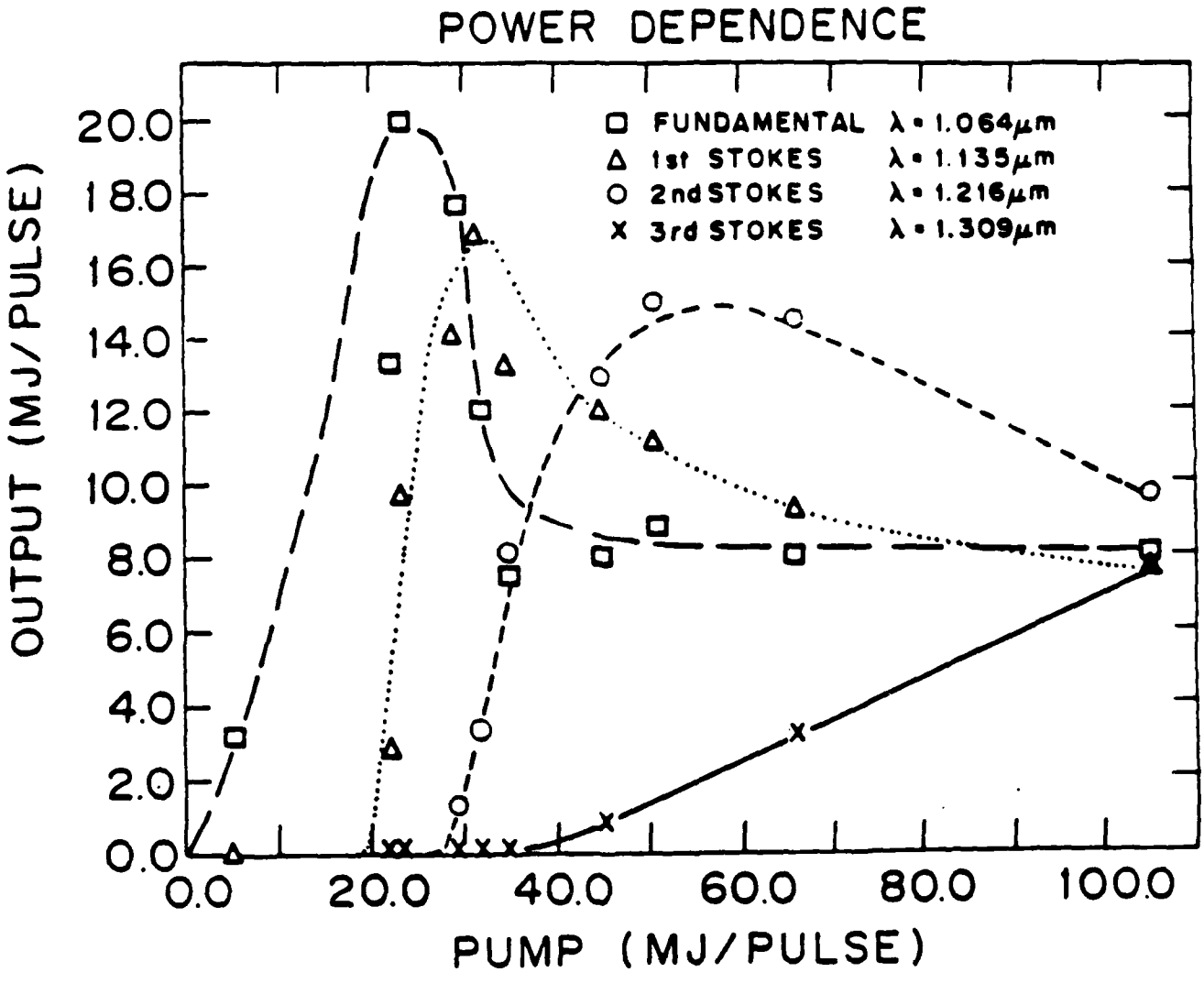
POWER DEPENDENCE
FUNDAMENTAL λ = 1.064μm
1st STOKES λ = 1.135μm
2nd STOKES λ = 1.216μm
3rd STOKES λ = 1.309μm
OUTPUT (MJ/PULSE)
20.0
18.0
16.0
14.0
12.0
10.0
8.0
6.0
4.0
2.0
0.0
0.0
20.0
40.0
60.0
80.0
100.0
PUMP (MJ/PULSE)

Figure 2.11.3

III EXTENDED DESCRIPTION

I. NONLINEAR OPTICAL PROCESSES IN LOWER DIMENSIONAL CONJUGATED STRUCTURES

1. INTRODUCTION

Conjugated π-electron organic and polymer structures are now well-known to exhibit unusually large nonresonant macroscopic second order $\chi^{(2)}_{ijk}(-\omega_3;\omega_1,\omega_2)$ and third order $\chi^{(3)}_{ijkl}(-\omega_4;\omega_1,\omega_2,\omega_3)$ nonlinear optical susceptibilities,[1] and their microscopic origin and mechanism can be successfully described by quantum field theory of many-electron systems in one and two dimensions.[2] - [11] In this description, as the spatial dimensionality of the many-electron system is effectively lowered, the motion among the many-electrons becomes highly correlated.[12] Electron correlation plays a major role in determining $\chi^{(2)}_{ijk}$ and $\chi^{(3)}_{ijkl}$ in conjugated π-electron systems, and, as we shall review, its effects cannot be neglected in properly accounting for the nonlinear optical properties of conjugated structures.

Reduced dimensionality and quantum confinement occur in material structures having effective confinement length scales L of less than one to several tens of nanometers. The opposite limit occurs in regular three dimensional bulk structures where L > 100 nm, and the electrons behave as a Fermi gas of weakly interacting particles. In this case, the electron motions are usually weakly correlated and well described by single-particle theory in the effective mass approximation.

Conjugated π-electron organic and polymer structures are viewed as lower dimensional systems in which quantum confinement effects are important. For instance, in conjugated linear chains, the many-electron system is confined in two dimensions with L < 0.5 nm transverse to the linear chain axis, and thus the π-electrons are delocalized in their motion only in one dimension along the longitudinal chain axis. As a result, the repulsive Coulomb interactions between electrons are strong, and electron motion becomes highly correlated

wherein the motion of any single electron depends on all the other remaining many electrons. The origin of the nonresonant $\chi^{(3)}_{ijkl}$ for these and related polymer structures then appears to reside in strong correlation behavior in virtual two-photon π-electron states.[9] - [11] This microscopic many-electron correlation description of nonlinear optical properties of conjugated structures is described in section 2 of this paper. We first review the nonlinear optical properties of linear polyenes both as a function of conformation and length as prototype one dimensional conjugated chains. The nonresonant microscopic nonlinear optical susceptibility is a strong function of the length of the polyene chain and not significantly dependent on structural conformation.

The role of dimensionality in nonlinear optical properties is further examined by a theoretical study of a two dimensional conjugated cyclic structure with L < 0.5 nm perpendicular to the molecular plane. Through comparison with the linear chain results, the microscopic origin of the nonlinear optical properties is shown to be similar for the two cases. A remarkable effect of increased dimensionality, however, is the decrease of the isotropically averaged third order susceptibility due to an actual reduction in the effective length available for the π-electrons to respond to an applied optical electric field.

In section 3, we present experimental measurements of the resonant nonlinear optical properties of thin films formed of large, two dimensional conjugated cyclic structures. Saturable absorption is observed in spin coated thin films of a naphthalocyanine derivative having an exceptionally large Q-band π-electron absorption (α of 1 x 10^5 cm^{-1}) centered at 810 nm. No unsaturable absorption background is observed. For laser frequencies near 810 nm, we find an intensity dependent refractive index (n_2) of 1 x 10^{-4} cm^2/kW. Based on the

results of the saturable absorption studies, we then demonstrate electronic absorptive optical bistability in a thin film Fabry-Perot etalon at nanosecond time scales.

2. MICROSCOPIC DESCRIPTION OF NONRESONANT $\gamma_{ijkl}(-\omega_4;\omega_1,\omega_2,\omega_3)$ FOR ONE AND TWO DIMENSIONAL STRUCTURES

The macroscopic nonlinear optical properties of organic molecular and polymer structures in condensed states are best described starting from the individual responses of isolated molecular or polymer chain units.[1] This approach, which clarifies the origin of $\chi^{(2)}_{ijk}$ and $\chi^{(3)}_{ijkl}$, is, however, not applicable to other material classes, such as inorganic semiconductors, where it is difficult to identify analogous microscopic sources of nonlinear polarization. For the moment neglecting intermolecular interactions, if the nonlinear susceptibility of an isolated molecule is known, then $\chi^{(2)}_{ijk}$ or $\chi^{(3)}_{ijkl}$ of the macroscopic ensemble of molecules is determined by the orientational distribution function of the independent units. Local field factors must also be included to account for the effect of the dielectric environment on the electric field strength at the molecular site. The macroscopic frequency-dependent second and third order susceptibilities $\chi^{(2)}_{ijk}(-\omega_3;\omega_1,\omega_2)$ and $\chi^{(3)}_{ijkl}(-\omega_4;\omega_1,\omega_2,\omega_3)$ can then be expressed in terms of the molecular susceptibilities $\beta_{ijk}(-\omega_3;\omega_1,\omega_2)$ and $\gamma_{ijkl}(-\omega_4;\omega_1,\omega_2,\omega_3)$ as[13]

$$\chi^{(2)}_{ijk}(-\omega_3;\omega_1,\omega_2) = N_u \sum_{s=1}^{c} R^{s}_{im'} R^{s}_{jn'} R^{s}_{ko'} f^{\omega_3}_{m'i'} \beta^{s}_{i'j'k'}(-\omega_3;\omega_1,\omega_2) f^{\omega_1}_{j'n'} f^{\omega_2}_{k'o'} \qquad (1)$$

and

$$\chi^{(3)}_{ijkl}(-\omega_4;\omega_1,\omega_2,\omega_3) = N_u \sum_{s=1}^{c} R^{s}_{im'} R^{s}_{jn'} R^{s}_{ko'} R^{s}_{lp'} f^{\omega_4}_{m'i'} \times \gamma^{s}_{i'j'k'l'}(-\omega_4;\omega_1,\omega_2,\omega_3) f^{\omega_1}_{j'n'} f^{\omega_2}_{k'o'} f^{\omega_3}_{l'p'} \quad (2)$$

where N_u is the number of unit cells per unit volume, the summation is over all molecules in the unit cell, R is a rotation matrix describing the orientation of each molecule in the unit cell, and f is the frequency dependent local field factor. The description of the macroscopic nonlinear optical response is thus reduced to an understanding of the microscopic second and third order susceptibilities β_{ijk} and γ_{ijkl} and knowledge of the orientational distribution of the molecular units in the condensed phase. As special cases, isotropic gases and liquids reduce Eqs. (1) and (2) to simpler forms. For example, for an isotropic ensemble

$$\chi^{(3)}_{1111}(-\omega_4;\omega_1,\omega_2,\omega_3) = N f^{\omega_4} f^{\omega_1} f^{\omega_2} f^{\omega_3} \gamma_g(-\omega_4;\omega_1,\omega_2,\omega_3) \quad (3)$$

where N is the number density of molecules and γ_g is the isotropically averaged susceptibility defined by

$$\gamma_g = \frac{1}{5}\left[\sum_{1} \gamma_{iiii} + \frac{1}{3}\sum_{i\neq j} (\gamma_{iijj} + \gamma_{ijij} + \gamma_{ijji})\right] \quad (4)$$

where the indices i and j represent the Cartesian coordinates x, y, and z.

The above formalism is strictly appropriate only for gases such that the mean intermolecular distance is large enough for the interaction between molecules to be negligible. In condensed states, some modifications are required to include the effects of intermolecular

interactions. In order to account for residual interactions with neighboring molecules, $\beta_{ijk}(-\omega_3;\omega_1,\omega_2)$ and $\gamma_{ijkl}(-\omega_4;\omega_1,\omega_2,\omega_3)$ can be "dressed" to extend their applicability beyond isolated molecular units. For instance, in dc-induced second harmonic generation (DCSHG) studies of dilute solutions,[3],[4] it was found that inclusion of dipole-mediated interactions between solvent and solute molecules provided excellent agreement of the theoretical values for an otherwise independent molecule with experimental measurements made in solution. In a more recent study[14],[15] of phase-matched second harmonic generation in single crystals of 2-methyl-4-nitroaniline (MNA), the existence of closely oriented pairs of molecules in the unit cell crystal structure required treatment of an MNA-MNA pair as the fundamental source of second order response. Because of the strong mutual effect of each molecule on the electronic structure of the other, calculation of $\beta_{ijk}(-2\omega;\omega,\omega)$ for an appropriately oriented pair of MNA molecules was necessary in order to obtain agreement with experiment. In any case, the fact that the intramolecular interaction energy is much stronger than the intermolcular interaction energy in organic molecular crystals, liquids, solutions, and polymer thin films means that the starting point for understanding the macroscopic nonlinear optical properties of these various condensed phases lies in an accurate description of the microscopic response from an isolated molecular unit.

The general theoretical expression for the components of the microscopic third order susceptibility tensor $\gamma_{ijkl}(-\omega_4;\omega_1,\omega_2,\omega_3)$ is derived from time-dependent, quantum electrodynamic perturbation theory. In order to avoid secular divergences that would occur when any subset of the input frequencies sums to zero, one employs the Bogoliubov-Mitropolsky method of averages.[16],[17] Owing to dispersive effects, $\gamma_{ijkl}(-\omega_4;\omega_1,\omega_2,\omega_3)$ is dependent on the input and output frequencies involved for each of the various possible

nonlinear optical phenomena. For the particular case of third harmonic generation, for example, one obtains

$$\gamma_{ijkl}(-3\omega;\omega,\omega,\omega) = \frac{1}{3!}\left(\frac{e^4}{4\hbar^3}\right)\Big[\sum_{n_1 n_2 n_3}{}' \Big\{ \frac{P_{jkl}[r^i_{gn_3}\,\bar{r}^j_{n_3n_2}\,\bar{r}^k_{n_2n_1}\,r^l_{n_1g}]}{(\omega_{n_3g}-3\omega)(\omega_{n_2g}-2\omega)(\omega_{n_1g}-\omega)}$$

$$+ \frac{P_{jkl}[r^j_{gn_3}\,\bar{r}^i_{n_3n_2}\,\bar{r}^k_{n_2n_1}\,r^l_{n_1g}]}{(\omega_{n_3g}+\omega)(\omega_{n_2g}-2\omega)(\omega_{n_1g}-\omega)} + \frac{P_{jkl}[r^j_{gn_3}\,\bar{r}^k_{n_3n_2}\,\bar{r}^i_{n_2n_1}\,r^l_{n_1g}]}{(\omega_{n_3g}+\omega)(\omega_{n_2g}+2\omega)(\omega_{n_1g}-\omega)}$$

$$+ \frac{P_{jkl}[r^j_{gn_3}\,\bar{r}^k_{n_3n_2}\,\bar{r}^l_{n_2n_1}\,r^i_{n_1g}]}{(\omega_{n_3g}+\omega)(\omega_{n_2g}+2\omega)(\omega_{n_1g}+3\omega)} \Big\}$$

$$- \sum_{n_1 n_2}{}' \Big\{ \frac{P_{jkl}[r^i_{gn_2}\,r^j_{n_2g}\,r^k_{gn_1}\,r^l_{n_1g}]}{(\omega_{n_2g}-3\omega)(\omega_{n_2g}-\omega)(\omega_{n_1g}-\omega)}$$

$$+ \frac{P_{jkl}[r^j_{gn_2}\,r^i_{n_2g}\,r^k_{gn_1}\,r^l_{n_1g}]}{(\omega_{n_2g}-\omega)(\omega_{n_1g}+\omega)(\omega_{n_1g}-\omega)} + \frac{P_{jkl}[r^j_{gn_2}\,r^k_{n_2g}\,r^i_{gn_1}\,r^l_{n_1g}]}{(\omega_{n_2g}+3\omega)(\omega_{n_2g}+\omega)(\omega_{n_1g}+\omega)}$$

$$+ \frac{P_{jkl}[r^j_{gn_2}\,r^k_{n_2g}\,r^l_{gn_1}\,r^i_{n_1g}]}{(\omega_{n_2g}+\omega)(\omega_{n_1g}-\omega)(\omega_{n_1g}+\omega)} \Big\} \Big] \qquad (5)$$

where $r^i_{n_1n_2}$ is the matrix element $\langle n_1|\, r^i\, |n_2\rangle$ ($\bar{r}^i = r^i - \langle r^i\rangle_{gg}$), $\hbar\omega_{ng}$ is the excitation energy of state n, the prime on the summations indicates the ground state is omitted, and P_{jkl} denotes the sum over all permutations of those three indices. We will be concerned here with the case where all of the optical frequencies are above the molecular vibrational and rotational modes but below the electronic excitation energies so that the nonlinear optical response is strictly electronic in origin. In addition, for conjugated organic structures, γ is dominated by the delocalized π-electron contributions which in general have both larger transition dipole moments and lower transition energies than the σ-electron excitations. Thus, with accurate

description of both the excitation energies and transition moments of the π-electron manifold, one can calculate the frequency dependence of each of the different third order nonlinear optical processes using expressions such as Eq. (5).

The theoretical method employed to achieve proper description of the π-electron manifold of conjugated organic molecular structures for calculation of $\gamma_{ijkl}(-\omega_4;\omega_1,\omega_2,\omega_3)$ has been described previously.[10] It consists of a multiply-excited configuration interaction calculation (SCF-MO-SDCI) performed on a molecular orbital basis obtained through self-consistent field theory in the rigid lattice CNDO/S approximation. This method, which has previously been proven successful in calculations of $\beta_{ijk}(-\omega_3;\omega_1,\omega_2)$ for a variety of conjugated structures will not be discussed here other than to re-emphasize the many-electron nature of the general problem. Because of the reduced dimensionality, Coulomb interactions among π-electrons result in marked electron correlation effects which render independent particle theories incomplete for description of nonlinear optical properties. This has already been demonstrated in the comparison of experimental and theoretical determinations of $\beta_{ijk}(-2\omega;\omega,\omega)$, where calculations involving both single and double-excited configuration interactions (SDCI) result in good agreement with experiment, whereas calculations with only single-excited configuration interactions (SCI) differ by as much as 50%. In the case of γ_{ijkl} for linear polyenes to be discussed below, independent particle models fare even worse, resulting not only in different magnitudes but also opposite sign than SDCI calculations and existing experimental data. Because independent particle results are not only quantitatively incorrect but also miss some important qualitative features of β_{ijk} and γ_{ijkl}, it is essential to take account of electron correlations through multiple-excited configuration interactions in descriptions of nonlinear optical processes.

A. One Dimension: Conjugated Linear Chains

We briefly review here the origin of the microscopic third order susceptibility $\gamma_{ijkl}(-\omega_4;\omega_1,\omega_2,\omega_3)$ in prototype conjugated linear chains as revealed by the above theoretical method.[9] - [11] In particular, we consider the linear polyenes which are hydrocarbon chains in which each carbon site is covalently bonded to a hydrogen and its two nearest neighbor carbons. The remaining valence electron of each carbon atom contributes to a delocalized, strongly correlated π-electron distribution along the carbon chain. The ground state of this system is a spin-singlet, broken-symmetry state in which the carbon lattice possesses a single-bond/double-bond alternation. We have performed calculations on polyenes ranging in length from four to sixteen carbon sites (N = 4 to 16) in both the all-*trans* and *cis-transoid* conformations.

Although the self-consistent field calculation of the ground state includes all of the valence shell electrons for each atom in the molecule, CI theory needs only to consider π-electron orbitals since the low-lying excitations are $\pi \rightarrow \pi^*$ transitions and for conjugated systems the π-electron contributions to $\gamma_{ijkl}(-\omega_4;\omega_1,\omega_2,\omega_3)$ dominate those from σ-electrons. Because the polyenes are members of the C_{2h} symmetry group, all of the π-electron states must possess either A_g or B_u symmetry. Within the centrosymmetric C_{2h} group, these two symmetries are of opposite parity leading to optical dipole selection rules. The ground state is always ^1A_g, and therefore the ^1B_u states are one-photon allowed transitions observable in the linear absorption spectrum. The excited ^1A_g states, on the other hand, are one-photon forbidden but two-photon allowed. Experimental and theoretical studies[18] - [24] of one-

photon and two-photon resonant processes in finite polyenes have shown that below the first optically allowed, dominant 1^1B_u state is located a strongly electron correlated two-photon 2^1A_g state.

Because the π-electron distribution is easily deformable along the conjugation axis by a perturbing optical electric field but is strictly confined in the two transverse directions, it is to be expected that the dominant tensor component of γ_{ijkl} will be γ_{xxxx} for which all of the electric fields are along the axis of conjugation. We define the x-axis as along the chain and the y-axis as the perpendicular direction within the molecular plane. In all of our calculations of varying chain length and conformation of linear polyenes, the γ_{xxxx} component was indeed found to be far larger than any of the others. As an example, for the specific case of *trans*-octatetraene (*trans*-OT) (Figure 1a) consisting of eight carbon sites (N=8), the independent, nonvanishing tensor components of the third harmonic susceptibility $\gamma_{ijkl}(-3\omega;\omega,\omega,\omega)$ at a nonresonant fundamental photon energy of 0.65 eV (λ=[1] 907 μm) are γ_{xxxx}=15.5, γ_{xyyx} = 0.6, γ_{yxxy}=0.5, and γ_{yyyy}=0.2 x 10^{-36} esu. All components involving the z-component necessarily vanish because of the symmetry constraints of the π-electron orbitals.

The symmetries, energies, and relevant transition dipole moments of the ten lowest calculated excited states of *trans*-OT are listed in Table I. All 153 of the calculated states are included in the calculation of $\gamma_{i,j=1}$, but Table I serves to illustrate the important points. The columns $\mu^x_{n,g}$ and $\mu^x_{n,1B}$ refer to the x-components of the transition dipole moment of each state with the ground state and with the 1^1B_u state, respectively. The optical selection rules are observed in the vanishing transition moments $\mu^x_{n,g}$ for all the ^1A_g states and $\mu^x_{n,1B}$ for all the ^1B_u states. It is also seen that the 1^1B_u state has by far the largest $\mu^x_{n,g}$ and the 6^1A_g state has

the largest $\mu^{x}_{n,1B}$. As a result, these two are the primary contributors to γ_{xxxx} as will be described below.

It is instructive to consider the individual terms in the sum over states perturbation expansion. Based on Eq. (5) and the symmetry selection rules described above, it is evident that the π-electron states in a third order process must be connected in the series $g \rightarrow {}^1B_u \rightarrow {}^1A_g \rightarrow {}^1B_u \rightarrow g$. For centrosymmetric structures, third order processes necessarily involve virtual transitions to both one-photon and two-photon states. For *trans*-OT, there are $(153)^3$ terms involved in the summations of Eq. (5). However, two of these terms are an order of magnitude larger than all the others and constitute 70% of γ_{xxxx}. The remaining terms to a large extent cancel one another resulting in a much smaller net contribution. In both of the dominant terms, the only ${}^1B_u$ state involved is the dominant low-lying one-photon $1{}^1B_u$ π-electron excited state. In addition to its low excitation energy, this state is important because its 7.8 D transition dipole moment with the ground state is more than three times larger than any other ground state transition moment. One of the two major terms comes from the double sum of Eq. (5) with both of the intermediate states being the $1{}^1B_u$. In the case of the double sum, the middle intermediate state is always the ground state. This term makes a negative contribution to γ_{xxxx} below resonance, since both the numerator and denominator are positive but the double sum has an overall negative contribution. The other major term is from the triple sum with the $6{}^1A_g$ state as the middle intermediate. This state, calculated at 7.2 eV, has a large transition moment with $1{}^1B_u$ of 13.2 D. This term makes a positive contribution to γ_{xxxx} and is larger than the first leading to an overall positive value for γ_{xxxx}. Importantly, the $6{}^1A_g$ consists of 60% double-excited configurations indicating it is highly correlated. SCI

calculations obtain a negative value for γ_{xxxx} because they do not adequately describe this state and therefore omit its large contribution.

Figure 2 displays the calculated dispersion curve for $\gamma_{xxxx}(-3\omega;\omega,\omega,\omega)$ of *trans*-OT as a function of the input photon energy. The first resonance, located at 1.47 eV (λ=0.84 μm) and indicated by the vertical dash in the figure, is due to the 3ω resonance of the 1^1B_u state. The second singularity, located at 2.08 eV (λ=0.6 μm), is from the 2ω resonance of the 2^1A_g state. As seen in Eq. (5), the ^1B_u states will have both 3ω and ω resonances in third harmonic generation, whereas the ^1A_g states will have only 2ω resonances. Other third order processes have different resonance selection rules. For example, in DCSHG both the ^1B_u and ^1A_g states (or, more generally, both one-photon and two photon states) have 2ω and ω resonances while there are no 3ω resonances. It should also be noted that in real systems natural broadening of electronic states will prevent divergence at the resonances. This is accounted for theoretically by making the excitation energies in Eq. (5) complex with the inclusion of an imaginary damping term. Unfortunately, damping constants cannot be reliably calculated, and one must therefore use empirical values.

In order to determine the influence of structural geometry on nonlinear optical properties, we have also calculated γ_{ijkl} for the *cis-transoid* (*cis*) conformation of polyenes (Figure 1b) over the same range of chain lengths. The results for the *cis* conformations are in direct analogy to those for *trans* indicating that geometry is not a predominant factor. For the range of chain lengths we have considered, we find that the transition energies of the 1^1B_u and 2^1A_g states of the *cis* conformation are just slightly red-shifted from the values for *trans* by 0.02 to 0.10 eV. For example, for *trans*-OT the 1^1B_u state is calculated at 4.42 eV and the 2^1Ag at 4.16 eV while for *cis*-OT the values are 4.37 eV and 4.11 eV, respectively.

Furthermore, just as for *trans*, the dominant tensor component of $\gamma_{ijkl}(-\omega_4;\omega_1,\omega_2,\omega_3)$ is γ_{xxxx}, and the most significant virtual transitions and the dispersion are essentially the same as discussed above. The mechanism for $\gamma_{ijkl}(-\omega_4;\omega_1,\omega_2,\omega_3)$ is still a symmetry-dictated virtual excitation process involving strongly correlated π-electron states. The calculated dispersion of $\gamma_{xxxx}(-3\omega;\omega,\omega,\omega)$ for *cis*-OT is compared to that of *trans*-OT in Figure 2. The two curves are very similar, and the most significant difference is the smaller nonresonant value in the case of *cis*-OT. Because of the nearly equal excitation energies, the first two resonances occur at very near the same energies for the two different structural conformations.

The similarity between the two conformations is further emphasized in the transition density matrix contour diagrams that graphically illustrate the electron redistribution upon virtual excitation. The transition density matrix $\rho_{nn'}$ is defined through the expression

$$\langle \mu_{nn'} \rangle = -e \int r\, \rho_{nn'}(r)\, dr \tag{6}$$

with

$$\rho_{nn'}(r_1) = \int \psi_n^*(r_1,r_2,\ldots r_M)\ \psi_{n'}(r_1,r_2,\ldots r_M)\, dr_2 \ldots dr_M \tag{7}$$

where M is the number of valence electrons included in the molecular wavefunction ψ. Contour diagrams for $\rho_{nn'}$ of the ground and 6^1A_g states with the 1^1B_u state for both the *cis* and *trans* forms of OT are compared in Figure 3, where solid and dashed lines correspond to increased and decreased charge density. The contour cut is taken 0.4 Å above the molecular plane since π orbitals vanish on the atoms. The antisymmetry of $\rho_{nn'}$ is a requirement for a

one-photon transition, and for a large transition dipole moment $\mu_{nn'}$ the contours should have well separated increased and decreased densities with particularly large magnitudes towards the ends. Of course, the actual charge density of any state, given by ρ_{nn}, must be symmetric because of the centrosymmetry of the molecule so that all states will have vanishing dipole moments. In Figure 3, the (a) *cis* and (b) *trans* virtual $g \rightarrow 1^1B_u$ transition results in a somewhat modulated redistribution of charge with transition moment x-components of 7.9 and 7.8 D, respectively. For the $1^1B_u \rightarrow 6^1A_g$ transition, however, there results a highly separated charge distribution in the (c) *cis* and (d) *trans* conformations. The corresponding transition moments are 12.0 and 13.2 D for the *cis* and *trans* cases, respectively.

There is very little experimental data available for $\gamma_{ijkl}(-\omega_4;\omega_1,\omega_2,\omega_3)$ of finite polyenes. Our calculations compare quite well with the experimental values that have been reported[25] for two of the shortest polyenes. Accounting for the proper fundamental photon energy, isotropic orientational averaging, and the small estimated σ-electron contribution, our results are in good agreement[10] with the gas phase DCSHG measurements of butadiene (N=4) and hexatriene (N=6) by Ward and Elliott. Comparison of calculated results with experimental measurement of both the sign and magnitude of γ is obviously an important test of the validity of a theoretical method, but it has all too often been neglected in recent literature.

Analysis of the chain length dependence of γ_{xxxx} for the *trans* and *cis* conformations shows that the two are further unified by a common power law dependence of γ_{xxxx} on L, defined as the distance in the x-direction between the two end carbon sites. The power law exponent was found to be 4.6 ± 0.2 with several common features leading to this rapid growth of γ_{xxxx} with chain length. First, the excitation energies decrease with increased chain length Second, the magnitudes of transition dipole moments along the chain axis increase steadily

with chain length. Third, while for OT and the shorter chains the nonlinear susceptibility is almost entirely composed of the contributions from only a few states, longer chains have significant contributions from an increasingly larger number of both ^1B_u and ^1A_g states.

B. Two Dimensions: Conjugated Cyclic Chains

In this section, we extend the microscopic description of γ_{ijkl} for one dimension to two dimensions and consider a specific example within the class of conjugated cyclic structures known as annulenes. As a major case, we consider the planar structure of cyclo-octatetraene (COT), the cyclic analog to OT with N=8, illustrated schematically in Figure 4. Although the geometrically-relaxed ground state of COT is known to be a non-planar, bent structure, we will examine only the planar structure of COT in this section. The purpose is to explore the effect of dimensionality on the microscopic features of $\gamma_{ijkl}(-\omega_4;\omega_1,\omega_2,\omega_3)$. Because the inclusion of the geometrically-relaxed distortions of the physically observed COT structure unnecessarily complicates comparison of cyclic structure results with those described above for linear chains, we consider only the planar structure. Analogies and contrasts between linear and cyclic structures are clearest when the only distinction is the increase in dimensionality from one to two so that one need not be concerned with decoupling dimensionality from non-planarity effects.

For linear chains, since the x-component of the transition dipole moments is much larger than the y- and z-components, the isotropically averaged susceptibility γ_g is effectively determined by the γ_{xxxx} component while all components involving transverse fields make negligible contributions. This reduces Eq. (4) to

$$\gamma_g = \frac{1}{5}\,\gamma_{xxxx} \ . \qquad (8)$$

But for cyclic structures, since the in-plane x- and y-directions are equivalent, γ_{xxxx} and γ_{yyyy} should be of equal magnitude. Furthermore, components such as γ_{xxyy} will also be significant since they involve these two directions as well. The corresponding non-negligible terms of Eq. (4) are

$$\gamma_g = \frac{1}{5}[\,\gamma_{xxxx} + \gamma_{yyyy} + \frac{1}{3}\,(\gamma_{xxyy} + \gamma_{xyxy} + \gamma_{xyyx} + \gamma_{yyxx} + \gamma_{yxyx} + \gamma_{yxxy})] \ . \qquad (9)$$

It seems, therefore, that one might be able to enhance γ_g by moving from linear to cyclic conjugated structures and opening pathways for new components of the γ_{ijkl} tensor to contribute. We shall demonstrate below, however, a most striking, opposite finding. We show that, because of the relevant length scales involved in the two problems, the conjugated cyclic structure will necessarily have a smaller γ_g than the corresponding conjugated linear chain with an equal number of carbon sites.

Our planar model of COT is a member of the dihedral D_{4h} symmetry group which is non-Abelian and, hence, has two-dimensional irreducible representations denoted as E classes. The allowed state symmetries for π-electron excitations are A_{1g}, A_{2g}, B_{1g}, B_{2g}, and E_u. Of these, only states of ^1E_u symmetry are one-photon allowed excitations from the $^1A_{1g}$ ground state. The ^1E_u states are doubly degenerate with the two representations related by a $\pi/2$ rotation about the z-axis perpendicular to the molecular plane. All of the remaining symmetries listed above describe nondegenerate, two-photon states. A typical feature of conjugated cyclic

molecules, including phthalocyanines and porphyrins, is the existence of a relatively low frequency absorption in the visible or near ultraviolet and a higher frequency absorption deeper in the ultraviolet.[26] This feature appears in our model COT with the weak low frequency $1\,^1E_u$ state at 4.4 eV and the much stronger higher frequency $2\,^1E_u$ state at 6.5 eV. In the case of phthalocyanines, however, it is always the low frequency band which is stronger.

In Table II we list the symmetries, energies, and relevant transition dipole moments for the eight lowest calculated excited states of COT. Again, a total of 153 states are calculated. The third and fourth columns list the x and y-components, respectively, of the transition moment between a given state and the ground state while the column labeled $\mu^x_{n,2E}$ lists the x-component of the transition moments of that state with the two degenerate representations of the $2\,^1E_u$ state; the y-components are given in the $\mu^y_{n,2E}$ column. Although the x- and y-directions are equivalent in COT, it is seen in the Table that these components of the transition moments are not always equal, and this is a direct result of the double degeneracy of the E_u states. Transition moments involving any degenerate pair of ^1E_u states with a two-photon state are clearly related by a $\pi/2$ rotation or $x \rightarrow y$, $y \rightarrow -x$. Thus, the appearance of negative signs in some of the transition moments merely reflects the choice of basis in Hilbert space and has no absolute physical meaning. By choosing an appropriate basis for the degenerate pair, the magnitudes of the x and y components can be made equal, although this is not necessary as illustrated in Table II.

The first one-photon doubly degenerate $1\,^1E_u$ state has very small transition moments with the ground state and a correspondingly small oscillator strength. The $2\,^1E_u$ doubly degenerate state, on the other hand, has a maximum transition moment of 4.6 D in this x-y basis and is a large oscillator strength one-photon state in analogy to the $1\,^1B_u$ state of OT.

Thus, the transition moments of the two-photon states with the 2^1E_u state determine their importance for $\gamma_{ijkl}(-\omega_4;\omega_1,\omega_2,\omega_3)$ and are also listed in Table II for the lowest-lying states.

Analysis of the various terms in the summations of Eq. (5) for COT reveals much similarity to the linear chain analog. As in OT, there is one dominant term in the double summation which is due to the state with the largest oscillator strength, in this case, the 2^1E_u state. The dominant contributions from the triple sum also all involve the 2^1E_u state, but rather than just one term, there are several significant contributions for COT. Each one is smaller than the dominant negative term from the 2^1E_u state, but together they again lead to positive values for the nonresonant tensor components γ_{ijkl}. The significant contribution from several terms involving different intermediate two-photon states is similar to what was found for the linear polyenes longer than OT.

In Figure 5, the transition density matrix $\rho_{nn'}$ is shown for the ground state with the two representations of the 2^1E_u state. The $\pi/2$ rotational relationship of the two representations of 2^1E_u is also clear here as in Table II. The charge redistribution for this transition is fairly modulated as it is for the linear chains. In the particular basis shown for the representation of the doubly degenerate 2^1E_u state, the transition moments along the x and y directions are comparable as seen in the Figure.

The calculated dispersion of the isotropic third order susceptibility $\gamma_g(-3\omega;\omega,\omega,\omega)$ is given in Figure 6. The nonresonant value is quite small compared to the linear chains. Very sharp resonances occur at 1.47 eV due to a 3ω resonance to 1^1E_u and 1.60 eV due to a 2ω resonance with 2^1A_{1g}. Since both of these states have very small transition moments in Table II, they only make significant contributions directly on resonance. Calculations including imaginary damping terms to account for the finite width of the electronic excitations show that

these resonances become completely washed out and the dispersion remains flat in this part of the spectrum. Experimental dispersion measurements, therefore, likely would not observe significant resonant enhancement until the 3ω resonance to the 2^1E_u state which occurs at 2.16 eV.

The calculated values of $\gamma_{ijkl}(-3\omega;\omega,\omega,\omega)$ for COT at the nonresonant fundamental photon energy of 0.65 eV are γ_{xxxx}=0.75 and γ_{xxyy}=0.21 x 10^{-36} esu. Because of the D_{4h} symmetry, $\gamma_{xxxx}=\gamma_{yyyy}$ and γ_{xxyy} is equal to all other components that involve two x-component fields and two y-component fields. This equivalence between the x and y-directions is in contrast to the linear polyene case where the γ_{xxxx} component dominates all others. Furthermore, the γ_{xxxx} component of OT (15.5 x 10^{-36} esu) is far larger than any of the components of COT. However, since COT has significant components in both the x and y directions, it is more reasonable to compare values of the isotropically averaged susceptibility. For COT, γ_g = 0.38 x 10^{-36} esu as compared to 3.4 x 10^{-36} esu for *trans*-OT. As in the case of comparing values for the *trans* and *cis* conformations of linear polyenes, here also we must consider the actual length scale involved in the problem.

The important length for nonlinear optical responses is the largest length over which charge can be separated due to the presence of an optical electric field. For the linear polyenes, that length is the distance along the conjugation axis separating the end carbons. For COT, the equivalent length is between two points on either end of a diameter of the ring. Additionally, since π-electron motion is constrained along the carbon lattice, the relevant length is one-half of the circumfence of the molecular structure. This distance is 5.3 Å for COT. For comparison, for *trans*-HT (N=6) γ_g = 0.75 x 10^{-36} esu at $\hbar\omega$=0.65 eV and the end-to-end length L is 6 Å. Thus, for these two very different structures where the relevant lengths are

nearly equal, we find that the calculated values of γ_g are also comparable. In the case of cyclic structures, the length which determines the magnitude of γ_g appears to be one-half of the circumference, and this is a general finding in calculations we have performed for other size rings which will be published separately.

3. RESONANT $\chi^{(3)}$ MEASUREMENTS IN QUASI-TWO DIMENSIONAL RING STRUCTURES: SATURABLE ABSORPTION AND OPTICAL BISTABILITY

We have shown in the previous section that increased dimensionality from linear to cyclic chains leads to a decrease in the isotropic susceptibility γ_g rather than an enhancement as one might first expect. This is due to an effective reduction in the length available for the π-electrons to respond to an applied optical electric field. There are, however, other compelling reasons to investigate conjugated cyclic structures for their nonlinear optical properties. Primary among these is the presence of optically intense low and high frequency bands in the visible and ultraviolet generally observed in large diverse classes of related ring structures that, in addition, exhibit important secondary material properties such as thermal and chemical stability and ease of fabrication and processing. Among such classes are the well-known, large ring porphyrin and phthalocyanine structures which exhibit well-defined intense Q and Soret bands in the visible and near uv, respectively. Free base porphyrin, for example, has long been identified as an analog of 18-annulene which possesses nine double bonds.[27] Although, in general, we expect the nonresonant $\chi^{(3)}_{ijkl}$ of ring structures not to be very large, porphyrin-like structures provide many attractive features for studying resonant $\chi^{(3)}_{ijkl}$ processes.

Optical bistability in saturable absorbers has long been under intense study,[28] first, to understand bistable phenomena and their relationships to the mediating intensity dependent refractive index n_2, and, second, to develop thin film nonlinear optical devices. Based on the microscopic descriptions discussed in the previous section, we have selected phthalocyanine structures [29][30] in order to conduct saturable absorption and optical bistability studies in quasi-two dimensional conjugated ring structures. We have succeeded in designing ultrathin naphthalocyanine films possessing large resonant n_2 values and in implementing wide aperture Fabry-Perot thin film etalons for optical bistability st dies. In addition to primary nonlinear optical properties, the design of the thin film etalons incorporated important secondary material properties: (i) large saturable absorption with zero unsaturable background; (ii) saturable absorption centered in the spectral range of operating laser diodes; (iii) thin film formation; (iv) spin coatable films and high through-put fabrication; and (v) photolithographic properties for micron size pattern features.

A first major example is the silicon naphthalocyanine oligomer(SINC) with the molecular structure shown in Figure 7. Both pure SINC and SINC solid solution ultrathin films were directly fabricated by spin coating techniques. The films were homogeneous and of high optical quality with typical thickness of 80nm and 420nm for pure dye and solid solution, respectively. Figure 8 shows the linear absorption spectra of the pure SINC film(solid line) and a solid solution film of SINC in PMMA(dashed line). The optical spectrum exhibits an intense Q-band centered in the near infrared at 810nm (1.53 eV) for the pure dye and 774nm (1.60 eV) for the solid solution, with a linewidth(FWHM) of 0.1 eV and linear absorption coefficient α of 1×10^5 cm^{-1}. The molecular symmetry of SINC is D$_{4h}$

and the doubly degenerate Q-band is analogous to the $1^1A_{1g} \rightarrow 1^1E_u$ π-electron transition of COT described in the previous section.

We first present a physical model for the optical excitations of the thin film and then present saturable absorption studies. A Maxwell-Bloch two-level model is used for the dependence of the saturation threshold power on pulse duration, and the experimental results support this simple picture. For laser frequencies near the absorption maximum, we find an effective n_2 of 1×10^{-4} cm^2/kW. Based on the saturable absorption behavior, electronic absorptive optical bistability at nanosecond time scales is then observed in thin film Fabry-Perot etalons. Bistability behavior is studied as a function of longer pulse duration purposely to distinguish thermally-induced bistable effects.

A. Glassy Polymer Dye Model and Saturable Absorption

In this section we present a physical model for optical excitations in the SINC ultrathin films. The films obtained by spin coating do not possess either positional or orientational long range order. Because of this random distribution of SINC molecules in the films, the excitations are strictly on-site π-electron transitions, which have a typical absorption coefficient α of 10^5 cm^{-1}. The on-site π-electron optical excitations in an isolated molecule have an intrinsic, temperature independent natural linewidth on the order of 0.1 to 1 GHz with corresponding radiative decay lifetime of 1 to 10 ns.

The large linewidth of the Q-band observed in Figure 8 is primarily due to inhomogeneous broadening. This site broadening in the thin film has a Gaussian shape which is a consequence of the statistical distribution of resonance frequencies of the optical centers due to a variation in local environment in the polymer matrix. Within the inhomogene-

broadened Gaussian envelope of the Q-band are a series of narrow homogeneous broadened resonances where the characteristic temperature dependence of the linewidth depends on the microscopic broadening mechanism. The linewidth of the homogeneous broadening in amorphous media can be accounted for [31][32] using the TLS(two level system)-glass models [33] introduced by Anderson, Halperin and Varma which have been fairly successful in accounting for many of the physical properties (e.g. specific heat, thermal conductivity, ultrasonic absorption) of disordered systems such as glasses and polymer-like matrices. The Hamiltonian of the glassy polymer dye thin film on a substrate can be written as [34]

$$H = H_0 + H_{12} + H_{23} \tag{10a}$$

$$H_0 = \varepsilon_0 \Psi_0^\dagger \Psi_0 + \varepsilon_1 \Psi_1^\dagger \Psi_1 + \frac{1}{2} E \sigma^z + \sum_q \hbar \omega_q (n_q + \frac{1}{2}) \tag{10b}$$

$$H_{12} = \frac{1}{2} \sum_\alpha V_0^\alpha \Psi_0^\dagger \Psi_0 \sigma^\alpha + \frac{1}{2} \sum_\alpha V_1^\alpha \Psi_1^\dagger \Psi_1 \sigma^\alpha \tag{10c}$$

$$H_{23} = \frac{1}{2} \sum_\alpha f^\alpha \epsilon \sigma^\alpha \tag{10d}$$

where H_0 is the noninteracting Hamiltonian of the molecule (the difference $\varepsilon_1 - \varepsilon_0$ corresponding to the Q-band absorption), the TLS, and the phonons; H_{12} is the electrostatic dipole interaction between the molecule and the TLS; and H_{23} is the interaction between the TLS and the phonons, i.e., the strain field ϵ is coupled to the TLS.

Each homogeneous line under the Gaussian envelope is approximated by a Lorentzian function, and the width is related to the temperature dependent population and phase relaxation rate of the excited state by Fourier transformation. The amorphous material surrounding an optical site can be considered as an ensemble of noninteracting TLS

flopping between two eigenstates as they emit or absorb acoustic phonons. The homogeneous line broadening in amorphous media comes from the dipole coupling of the optical sites with the TLS's, and the line width can be expressed in terms of TLS the lifetime (or flip-flopping rate), the temperature dependence of which is determined from the coupling between the TLS and the strain field manifested as acoustic phonons. In this way, the line width of optical sites in the amorphous media is predicted to have $T^{1+\delta}$ ($0< \delta \leq 1$) dependence, and the absolute magnitude can be obtained once all the physical parameters for the TLS are known. For various organic molecules in different polymeric matrices, the theoretically predicted temperature dependence of the homogeneous linewidth is in good agreement with spectral hole burning data. [35][36] According to photochemical hole burning data on porphyrins and phthalocyanines in various glasses and polymeric matrices, [37] the homogeneous linewidth of the naphthalocyanine oligomer at room temperature is estimated to be between 10 and 100 GHz. For SINC films, comparison of the homogeneous linewidth (100 GHz) with the inhomogeneous width (0.1 eV) shows that the Gaussian envelope contains on the order of ten thousand Lorentzian broadened resonances. [38][39]

Saturable absorption behavior within the Q-band of the thin pure-SINC and SINC solid-solution films was investigated as a function of pulse duration and wavelength of the incident beam. A methane Raman cell pumped by fundamental or doubled Nd:YAG output was used to produce Stokes radiation near the peak maximum of the Q-band; at 813nm for a pure SINC thin film and 770nm for a SINC solid solution thin film. The methane Raman cell pumped by a Quantel Nd:YAG picosecond laser system provided 30GHz bandwidth 30 ps pulses of 200 μJ per pulse that were easily focused to give light intensities exceeding

MW/cm^2. Nanosecond pulses of 30 GHz bandwidth with an energy of 20 μJ per pulse were obtained in the same way by using a Quanta-Ray DCR Nd:YAG laser system to provide an incident intensity of 500 kW/cm^2. Figure 9 shows the incident intensity dependence of the absorption αL for 30 ps (circles: pure-SINC, triangles: SINC solid-solution) and 10 ns (squares: pure-SINC) pulses, respectively. The change in the absorption was reproducible through many cycles of increased and decreased incident light intensity. Data points for 10 ns are more scattered owing simply to power fluctuations in the Nd:YAG pump laser. In the case of the pure SINC film, if the light intensity was increased more than the maximum of the data points, i.e., 30 MW/cm^2 for 30 ps pulses and 200 KW/cm^2 for 10 ns pulses, an irreversible, simple melt phase change was observed in the film. But for the solid solution film, no irreversible change was observed up to an incident intensity of 4GW/cm^2, and furthermore, the saturation behavior was almost identical to that of the pure SINC film.

The solid lines in Figure 9 are least squares curves to a Bloch-type saturable absorption

$$\alpha(I)L = \frac{\alpha_0 L}{1 + I/I_0} + \alpha_B L \qquad (11)$$

where I_0 is the threshold power for the saturation, α_0L gives the low intensity linear absorption, and α_BL is the unsaturable background absorption. Importantly, α_BL was found to be zero for both the pure SINC and solid solution films. In the case of the pure SINC film, the threshold powers for saturation were 100MW/cm^2 and 440kW/cm^2 for 30ps and 10ns pulses, respectively. The threshold power for 10ns pulse is lower than that for 30ps pulse, but this trend saturates at or near the 10μs scale. Importantly, for the SINC solid solution thin film, the threshold power for 30ps pulse was also 100MW/cm^2, the same

value as that of the pure SINC film. The fact that the saturable absorption behavior is identical for both pure SINC and solid solution film is quite striking, and can be accounted for by the absence of any positional and orientational order between molecular sites in the thin film phase; thus, there is no phase coherence between optical sites. From this we can conclude that the on-site π-electron excitations of the Q-band in individual molecular sites are responsible for the large resonant nonlinear optical response.

The pulse duration dependence of the saturation absorption threshold power is well explained in terms of a two-level optical system interacting with the resonant incident light[40][41]. The dynamic transmission can be described by two coupled rate equations,

$$\frac{\partial n(x,t)}{\partial t} = -I(x,t)\sigma[n(x,t) - \{N_0 - n(x,t)\}] - \frac{n(x,t)}{\tau_s} \tag{12}$$

$$\frac{\partial I(x,t)}{\partial x} = -I(x,t)\sigma[\{N_0 - n(x,t)\} - n(x,t)] \tag{13}$$

where N_0 is the total number of molecules per unit volume, $n(x,t)$ is the number of molecules in the excited state at depth x and time t, σ is the absorption cross section per molecule, and τ_s is the radiative decay time of the excited state. Now let the incident pulse shape $f(t)$ be normalized by the incident light intensity,

$$I(0,t) = I_0 f(t) \tag{14}$$

As the light pulse passes through the absorbing molecule, the pulse is distorted as well as attenuated. The change in the pulse shape can be expressed in terms of a transmission function $T(x,t)$ at depth x and time t, defined as

$$I(x,t) = I_0 f(t) T(x,t)$$

The two equations (12) and (13) can be reduced to one equation for the transmission $T(x,t)$:

$$\frac{\partial \ln T(x,t)}{\partial(t/\tau_s)} + \ln T(x,t) = 2\sigma\tau_s I_0 f(t)(1 - T(x,t)) + \ln T_0 \qquad (16)$$

where I_0 is the incident light intensity, T_0 is the low intensity transmission, and $f(t)$ is the incident light pulse profile. From numerical simulation of Eq.(16), the saturation threshold intensity I_s can be obtained for a given pulse width and excited state lifetime τ_s. Furthermore, the ratio of saturation threshold for two given pulse widths can be used to uniquely determine τ_s. Using 230 as the ratio of threshold powers at 30 ps and 10 ns as determined from our experiment, we find the excited state lifetime to be 5 ns, in good agreement with previous independent relaxation measurements on related structures [30][42].

From the saturable absorption measurement, [28] we can also estimate the nonlinear refractive index n_2. The nonlinear optical susceptibility $\chi(\omega)$ for a Bloch type system is given by

$$\chi(\omega) = (\frac{\alpha_0 c}{4\pi\omega})(\frac{\Delta + i}{1 + \Delta^2 + I/I_s}) \qquad (17)$$

where α_0 is the linear absorption coefficient, Δ is the detuning $(\omega - \omega_0)/\Gamma$, and I_s is the saturation power. The nonlinear refractive index n_2 is the derivative of the intensity dependent refractive index n with respect to the inensity I, so for this model

$$n_2 = \frac{1}{3}(\frac{4\pi}{n_0})^2 \chi^{(3)} = -(\frac{\alpha_0 \lambda}{4\pi I_s})(\frac{\Delta}{(1 + \Delta^2)^2}) \qquad (18)$$

From this expression, we obtain a value of n_2 for the pure-SINC thin film of 1×10^{-4}cm^2/W.

To fully characterize the nonlinear absorption properties of the pure SINC film, we measured the dispersion of the Q-band nonlinear absorption. A Spectra-Physics 380B cw ring dye laser using LDS 821 dye and tunable between 790 nm and 860 nm was used as the light source with typical peak powers of 150 mW. The cw dye output of 5 MHz bandwidth was chopped by an acousto-optic modulator (AOM), so that 10 μs pulses were produced at a low duty cycle (10^{-4}) to eliminate any heating effects. A light intensity of approximately 80 kW/cm^2 was obtained by focusing the laser output directly onto the sample with a microscope objective lens.

The dispersion of the nonlinear absorption of the thin film is compared in Figure 10 with the linear absorption spectrum. It is clear that the change in absorption is maximum on resonance and decreases in moving away from the peak. The dashed lines are a least squares fit to a Gaussian envelope model for the linear absorption, and the dispersion was derived from the Kramers-Kronig relations. The dotted lines are the fitted curves for the nonlinear absorption and dispersion. We can see that the maximum change of refractive index as obtained from Eq.(18) occurs at 776 nm, and the maximum n_2 at 776 nm results from a linear superposition of the refractive index changes of each homogeneously broadened resonance within the inhomogeneously broadened envelope.

B. Optical Bistability

SINC thin films can be employed as the nonlinear medium in Fabry-Perot etalons for optical bistability studies. The etalon was formed by spin coating a wide area (2 - 5 in diameter) thin film of approximately 80 nm thickness on the front mirror of two high reflecting dielectric mirrors of a Burleigh RC-110 Fabry-Perot interferometer. The

spectral range of the cavity was adjustable and set at 12.5 GHz. Initial cavity detuning was adjusted by varying the high voltage applied to a PZT annular ring that held the output mirror (the PZT had total motion of 2.21 μm/1000 V), and when this output mirror was scanned, a Fabry-Perot interference pattern with a finesse of 2 was obtained with the sample in the cavity.

The optical bistability experimental layout (Figure 11) was basically the same as the arrangement used for measuring the dispersion of saturable absorption. The laser output was partially reflected by a pellicle beam splitter to a reference silicon detector, and the transmitted beam was tightly focused on the thin film which had been spin coated directly onto the front mirror. The output fringes were collimated and passed through a 500 μm pinhole, and a sample silicon detector monitored the intensity at the central part of the Bull's eye interference fringe. Silicon PIN photodiodes were used for reference and sample arms, and the output intensity versus input intensity was directly displayed on a 1 GHz oscilloscope operating in the x-y mode and externally triggered. At nanosecond time scales, initial measurements were attempted at 813 nm using the output from the Nd:YAG pumped methane Raman cell as the laser source, but later, more stable amd smooth pulses at 799 nm from a single-mode pulsed Ti:Al_2O_3 laser pumped by a frequency doubled Nd:YAG laser were used. Figure 12 shows the bistable hysteresis behavior observed when 40 ns pulses with intensity 160 kW/cm^2 at 799 nm were incident on the nonlinear F-P. It was found that for zero cavity detuning (ϕ=0.0) the bistable behavior was the largest, and when the cavity was detuned ($\phi=\pi$), the shape of the hysteresis curve changed and the effect became much smaller. In each case, the data were reproducible through many cycles

of increased and decreased incident light intensity. Further, the data were also reproducible when focussing at different areas of each film sample. This kind of initial cavity detuning dependence is typical of absorptive OB, which results from saturable absorption and a subsequent change in the loss of the F-P cavity, enabling higher transmission than is possible at low light levels. However, the greatly reduced effects observed for nonzero cavity detuning indicate a very small dispersive contribution.

The incident laser wavelength was moved to 780 nm corresponding to near optimum conditions for possible dispersive contributions to the bistability. The same measurements were repeated, and under all conditions no bistable behavior was observed (Figure 13). The absence of any bistable behavior at 780nm, where a large dispersive effect is expected from the Kramers-Kronig relation analysis, means simply that the relatively broad Q-band is not one single homogeneously broadened line but an inhomogeneously broadened envelope for many homogeneous lines, and supports the microscopic picture of the glassy polymer SINC film. Thus, near maximum saturable absorption at 810 nm, naphthalocyanine thin films exhibit primarily absorptive optical bistability at nanosecond time scales. The above analysis is based on steady state conditions for optical bistability because of the relevant time scales (pulse width: 40ns; relaxation time: 5ns; and cavity roundtrip time: 1ns) but transient effects may also play some role in the observed hysteresis behavior, which continues to be examined in on-going studies.

Since purely absorptive optical bistability is rarely observed, a systematic series of studies of possible thermally-induced refractive index changes in the thin films were performed as a function of increased pulse duration from 10^{-6} to 2 seconds. The laser sour-

used in these studies was the AOM chopped, Spectra-Physics cw ring dye laser described above. Figure 14 shows an example of the optical bistability observed; the pulse width was 2.0 sec and the duty cycle 20%. When the cavity was tuned on resonance with the incident light wavelength (ϕ=0.0, lower right in Figure 14), no hysteresis loop was observed, indicating the lack of an absorptive bistability effect, and this was true even when the dye laser output frequency was resonant with the linear absorption peak of the sample. However, for a negative ϕ (-1.0, left in Figure 14), bistable hysteresis with a counterclockwise circulation was observed, and for a positive ϕ (0.75, upper right in Figure 14), the bistable hysteresis had clockwise circulation. With the pulse width and the resonant wavelength near the linear absorption peak of 810 nm, the bistable behavior is due to a thermally-induced dispersive intensity dependent refractive index change. Most importantly, this behavior is distinctly different from the fast pulse bistability observed at nanosecond timescales.

For both electronic absorptive and thermal dispersive optical bistability, the hysteresis loops do not show a complete switching on and switching off. The reason for this is that eventhough the resonant n_2 value of the SINC thin film is fairly large, the film thickness (80 nm) is so small that the nonlinear phase shift experienced by the light inside the etalon is not large enough for complete switching to occur. Thicker SINC containing films have been prepared in our continuing studies.

4. CONCLUSION

Electron correlation effects markedly determine the virtual electronic excitation processes and nonlinear optical properties of the low dimensional structures of conjugated linear and cyclic chains. Microscopic understanding of the the origin of the large...

fast nonresonant $\chi^{(2)}_{ijk}(-\omega_3;\omega_1,\omega_2)$ and $\chi^{(3)}_{ijkl}(-\omega_4;\omega_1,\omega_2,\omega_3)$ of these materials is obtained through many-electron calculations of the molecular susceptibilities $\beta_{ijk}(-\omega_3;\omega_1,\omega_2)$ and $\gamma_{ijkl}(-\omega_4;\omega_1,\omega_2,\omega_3)$ and direct comparison with available experimental results. Details of the mechanism for $\gamma_{ijkl}(-\omega_4;\omega_1,\omega_2,\omega_3)$ of one dimensional conjugated linear chains have been explained in terms of virtual transitions among highly correlated π-electron states, and contour diagrams of transition density matrices $\rho_{nn'}$ provided direct illustration of the most significant virtual transitions. The dependences of $\gamma_{ijkl}(-\omega_4;\omega_1,\omega_2,\omega_3)$ on chain length and structural conformation have been examined, and conformation was found to be only significant in as much as it affects the actual physical length of the chain. Results for the all-*trans* and *cis-transoid* conformations of polyenes are unified by a power law dependence of the dominant tensor component $\gamma_{zzzz}(-3\omega;\omega,\omega,\omega)$ on the chain length L with an exponent of 4.6±0.2.

A theoretical study of $\gamma_{ijkl}(-\omega_4;\omega_1,\omega_2,\omega_3)$ in a two dimensional conjugated cyclic structure allowed examination of the role of dimensionality in the nonlinear optical properties of conjugated systems. The origin of $\gamma_{ijkl}(-\omega_4;\omega_1,\omega_2,\omega_3)$ in this case was found to be very similar to that for the one dimensional case, but the magnitudes of the various components of γ_{ijkl} are all smaller than the γ_{zzzz} component of the one dimensional chain with an equal number of carbons. More important, the isotropically averaged third order susceptibility γ_g is also much less for the two dimensional structure as compared to the one dimensional chain. Our analysis shows that this is a result of a reduction in the effective length over which π-electrons can respond to an applied optical electric field. For two dimensional cyclic structures, this length is one-half of the circumference of the ring.

compared to the full end-to-end chain length in one dimensional structures. As a general rule, two dimensional conjugated cyclic structures are therefore expected to have smaller nonresonant $\chi^{(3)}_{ijkl}(-\omega_4;\omega_1,\omega_2,\omega_3)$ values than their one dimensional analogs.

The presence of large oscillator strength π-electron bands in the visible and near ultraviolet characteristic of conjugated quasi-two dimensional structures provides attractive conditions for studying resonant $\chi^{(3)}$ processes, especially in phthalocyanine-related structures which also possess outstanding secondary material properties. We have demonstrated that such two dimensional structures can be designed as wide area, spin coatable nonlinear optical films and that these can be represented as a microscopic composite system of molecular optical sites in a TLS-glass random medium. The resonant nonlinear optical properties of homogeneously broadened lines contained in the inhomogeneously broadened Gaussian envelope were directly investigated by standard saturable absorption measurements. These results showed for the SINC films that saturable absorption occurs at the peak maximum of the low frequency Q- band near 810 nm with essentially zero unsaturable absorption background and that on-site π-electron excitations of the Q- band in individual molecular sites are responsible for the large resonant nonlinear optical response n_2 of 1×10^{-4} cm^2/kW at 810 nm.

A careful study of optical bistability in thin film etalons demonstrated that near the peak maximum of the saturable Q-band centered at 810 nm, SINC thin films exhibit primarily electronic absorptive optical bistability at fast time scales (nanoseconds). At long timescales (seconds), thermally-induced dispersive bistability occurs which is entirely different and distinct from the observed fast time behavior.

The present results represent a first report on studies centering on conjugated quasi-two dimensional structures. Futher theoretical and experimental studies of larger ring structures and micron thick films of naphthalocyanines for their resonant and nonresonant $\chi^{(3)}$ behavior have been completed and will be reported separately.

References

[1] See, for example, *Nonlinear Optical Properties of Organic and Polymeric Materials*, D.J. Williams, ed., ACS Symp. Series, Vol. 233 (American Chemical Society, Washington, D. C., 1983).

[2] S.J. Lalama and A.F. Garito, Phys. Rev. **A20**, 1179 (1979).

[3] K. D. Singer and A. F. Garito, J. Chem. Phys. **75**, 3572 (1981).

[4] C.C. Teng and A.F. Garito, Phys. Rev. Lett. **50**, 350 (1983); Phys. Rev. **B28**, 6766 (1983).

[5] A.F. Garito, K.D. Singer and C.C. Teng, in Ref. 1, Chap. 1.

[6] A.F. Garito, C.C. Teng, K.Y. Wong and O. Zamani-Khamiri, Mol. Cryst. Liq. Cryst. **106**, 219 (1984).

[7] A.F. Garito, Y.M. Cai, H.T. Man and O. Zamani-Khamiri, in *Crystallographically Ordered Polymers*, D.J. Sandman, ed., ACS Symp. Series, Vol. 337 (American Chemical Society, Washington, D. C., 1987), Chap. 14.

[8] A.F. Garito, K.Y. Wong and O. Zamani-Khamiri, in *Nonlinear Optical and Electroactive Polymers*, D. Ulrich and P. Prasad, eds. (Plenum, New York, 1987).

[9] J.R. Heflin, K.Y. Wong, O. Zamani-Khamiri, and A.F. Garito, J. Opt. Soc. Am. B **4**, 136 (1987).

[10] J.R. Heflin, K.Y. Wong, O. Zamani-Khamiri and A.F. Garito, Phys. Rev. **B38**, 1573 (1988).

[11] A. F. Garito, J.R. Heflin, K.Y. Wong, and O. Zamani-Khamiri, in *Nonlinear Optical Properties of Polymers*, A.J. Heeger, D. Ulrich, and J. Orenstein, eds. (Mater. Res. Soc. Proc. **109**, Pittsburgh, PA, 1988), pp. 91-102; Mol. Cryst. Liq. Cryst. **160**, 37 (1988).

[12] See, for example, J. Solyom, Adv. in Phys. **28**, 201 (1979) and references therein.

[13] A. F. Garito and K. Y. Wong, Polymer J. **19**, 51 (1987).

[14] C. H. Grossman, Ph. D. Thesis, University of Pennsylvania (1987).

[15] C. H. Grossman, J. R. Heflin, K. Y. Wong, O. Zamani-Khamiri, and A. F. Garito, in *Nonlinear Optical Effects in Organic Polymers*, F. Kajzar and J. Messier, eds. (in press).

[16] N.N. Bogoliubov and Y.A. Mitropolsky, *Asymptotic Methods in the Theory of Nonlinear Oscillations* (Gordon and Breach,1961) translated from Russian.

[17] B.J. Orr and J.F. Ward, Mol. Phys. **20**, 513 (1971).

[18] B.S. Hudson and B.E. Kohler, J. Chem. Phys. **59**, 4984 (1973).

[19] See, for example, B.S. Hudson, B.E. Kohler, and K. Schulten, in *Excited States*, Vol. 6, E.C. Lim, ed. (Academic Press, New York, 1982), p. 1 and references therein.

[20] A. A. Ovchinnikov, I. I. Ukrainski, and G. V. Kuentsel, Soviet Phys. Uspekhi **15**, 575 (1973) and references therein.

[21] K. Schulten, I. Ohmine, and M. Karplus, J. Chem. Phys. **64**, 4422 (1976).

[22] K. Schulten, U. Dinur and B. Honig, J. Chem. Phys. **73**, 3927 (1980).

[23] Z.G. Soos and S. Ramasesha, Phys. Rev. B**29**, 5410 (1984).

[24] P. Tavan and K. Schulten, Phys. Rev. B**36**, 4337 (1987).

[25] J.F. Ward and D.S. Elliott, J. Chem. Phys. **69**, 5438 (1978).

[26] R. P. Linstead, J. Chem. Soc. 2873 (1953).

[27] M. Gouterman, J. Mol. Spect. **6**, 138 (1961).

[28] See, for example, H. M. Gibbs, *Optical Bistability: Controlling Light with Light* (Academic, Orlando, 1985).

[29] J.A. Amstrong, J. Appl. Phys. **36**, 471 (1965).

[30] W.F. Kosonocky and S.E. Harrison, J. Appl. Phys. **37**, 4789 (1966).

[31] A.G.Redfield, Adv. Magnetic Resonance **1**, 1 (1968).

[32] See, for example, K.E. Jones and A. H. Zewail in *Springer Series in Chemical Physics, vol.3: Advances in Laser Chemistry*, A. Zewail, ed. (Springer, New York, 1978).

[33] P. W. Anderson, B. I. Halperin, C. Varma, Philo. Mag. **25**, 1 (1972).

[34] S. K. Lyo and R. Orbach, Phys. Rev. 22, 4223 (1980).

[35] A. Gutierrez, G. Castro, G. Schulte and D. Haarer, in *Organic Molecular Aggregates*, P. Reineker, H. Haken and H. C. Wolf, eds. (Springer, New York, 1983).

[36] R. M. Macfarlane and R. M. Shelby, J. of Lumin. **36**, 179 (1987).

[37] S. Volker and R. M. Macfarlane, IBM J. Res. Develop. **23**, 547 (1979).

[38] A. M. Stoneham, Rev. Mod. Phys. **41**, 82, (1969).

[39] M. Romagnoli, W.E. Moerner, F.M. Schellenberg, M.D. Levenson and G.C. Bjorklund, J. Opt. Soc. Am. **B 1**, 341 (1984).

[40] P. Gires and F. Combaud, J. Phys. **26**, 325 (1965).

[41] A.C. Seldon, Brit. J. Appl. Phys. **18**, 743 (1967).

[42] J. McVie, R.S. Sinclair, and T.G. Truscott, J. Chem. Soc. Faraday Trans. 2 **74**,1870 (1978).

Table I. The symmetries, energies and selected transition dipole moments of the calculated low-lying states of *trans*-octatetraene.

Symmetry	Energy (eV)	$\mu^{x}_{n,g}$ (D)	$\mu^{x}_{n,1B}$ (D)
2^1A_g	4.15	0.00	2.82
1^1B_u	4.42	7.81	0.00
2^1B_u	4.79	0.86	0.00
3^1A_g	5.19	0.00	0.07
4^1A_g	6.00	0.00	2.84
5^1A_g	6.07	0.00	1.11
3^1B_u	6.47	0.01	0.00
4^1B_u	7.01	1.11	0.00
6^1A_g	7.16	0.00	13.24
5^1B_u	7.30	1.14	0.00

Table II. The symmetries, energies, and selected transition dipole moments of the calculated low-lying states of cyclo-octatetraene.

Symmetry	Energy (eV)	$\mu^{x}_{n,g}$(D)	$\mu^{y}_{n,g}$(D)	$\mu^{x}_{n,2E}$(D)	$\mu^{y}_{n,2E}$(D)
1^1A_{2g}	2.24	0.00	0.00	-1.60, 2.40	-2.40, -1.60
2^1A_{1g}	3.19	0.00	0.00	0.14, 0.09	-0.09, 0.14
1^1E_u	4.41	0.05	-0.03	0.00, 0.00	0.00, 0.00
1^1E_u	4.41	0.03	0.05	0.00, 0.00	0.00, 0.00
1^1B_{2g}	5.21	0.00	0.00	-0.33, 0.50	0.50, 0.33
1^1B_{1g}	5.94	0.00	0.00	1.03, 0.68	0.68, -1.03
2^1E_u	6.48	4.58	-3.04	0.00, 0.00	0.00, 0.00
2^1E_u	6.48	3.04	4.58	0.00, 0.00	0.00, 0.00

Figure 1. Schematic diagrams of the molecular structures for (a) all-*trans* and (b) *cis-transoid* polyenes.

Figure 2. Calculated dispersion of $\gamma_{xxxx}(-3\omega;\omega,\omega,\omega)$ for *trans*-OT (solid curve). The vertical dashes locate the 3ω resonance to the 1^1B_u state and the 2ω resonance to the 2^1A_g state. The dotted curve shows the analogous calculated dispersion for *cis*-OT.

Figure 3. Transition density matrix diagrams for (a) *cis*-OT and (b) *trans*-OT ground states with the 1^1B_u state and (c) *cis*-OT and (d) *trans*-OT 6^1A_g states with the 1^1B_u state. In both cases, these are the most important virtual transitions for $\gamma_{xxxx}(-\omega_4;\omega_1,\omega_2,\omega_3)$. The corresponding x-components of the transition dipole moments are 7.9, 7.8, 12.0, and 13.2 D, respectively.

Figure 4. Schematic diagram of the molecular structure of planar cyclo-octatetraene (COT).

Figure 5. Transition density matrix diagrams for the ground state of COT with each of the two representations of the doubly degenerate 2^1E_u state. The $\pi/2$ rotational relationship between the two representations is clear. In this basis for the 2^1E_u degenerate pair, the x and y-components of the transition dipole moments are 4.6 and -3.0 D for (a) and 3.0 and [illegible] D for (b), respectively. Other choices for the 2^1E_u basis will result in different values for the individual components of the transition dipole moments, but the magnitude of the transition dipole moment vector must remain invariant.

Figure 6. Calculated dispersion of the isotropically averaged third order susceptibility $\gamma_g(-3\omega;\omega,\omega,\omega)$ for COT.

Figure 7. Schematic diagram of the molecular structure of silicon-naphthalocyanine oligomer (SINC).

Figure 8. Linear absorption spectra of pure SINC (solid curve) and SINC solid solution (dashed curve) thin films. The large oscillator strength Q-band absorption peaks at 1.53 eV (810 nm) in pure SINC film and 1.60 eV (774 nm) in SINC solid solution film.

Figure 9. Saturable absorption data and least squares fit to Eq. (11). Squares are data for pure SINC film at pulse width τ_p= 10 ns; circles, pure SINC film at τ_p= 30 ps; and triangles, SINC solid solution film at τ_p= 30 ps. αL is reflection calibrated and the low intensity limit is αL= 1.40.

Figure 10. Dispersion of saturable absorption between 1.45 eV and 1.55 eV measured with 10 μs pulse. The solid line is the linear absorption curve. The dashed line is the Gaussian function least squares fit curve of the linear absorption, and the dotted line is a similar least squares fit of the nonlinear absorption. The curves with maxima occurring at λ= 776 nm correspond to the real parts of the refractive indices obtained from the Kramers-Kronig relations.

Figure 11. Schematic diagram of optical bistability experiment for the pulse widths 10^{-6} to 2.0 sec (AOM : acousto-optic modulator, PH : pinhole, PD : photodiode). For nanosecond pulse width measurements, a single-mode Ti:Al_2O_3 laser replaced the Ar^+ laser, ring dye laser, and AOM configuration.

Figure 12. Absorptive optical bistability observed for polymer dye etalon with pulse width τ_p= 40 ns and wavelength λ=799 nm. In (a) the initial cavity detuning ϕ_0 is set at 0, and in (b) the initial cavity detuning ϕ_0 is set at π.

Figure 13. No optical bistability observed for polymer dye etalon with pulse width τ_p= 40 ns and wavelength λ=780 nm for initial cavity detuning ϕ_0 set at either 0 or π.

Figure 14. Thermal dispersive optical bistability observed for polymer dye etalon with pulse width τ_p= 2 sec and wavelength λ=810 nm. The lower right curve is for the initial cavity detuning ϕ_0= 0.0, the left curve for ϕ_0= -1.0, and the upper right curve for ϕ_0= 0.75.

(a) (b)

Figure 1

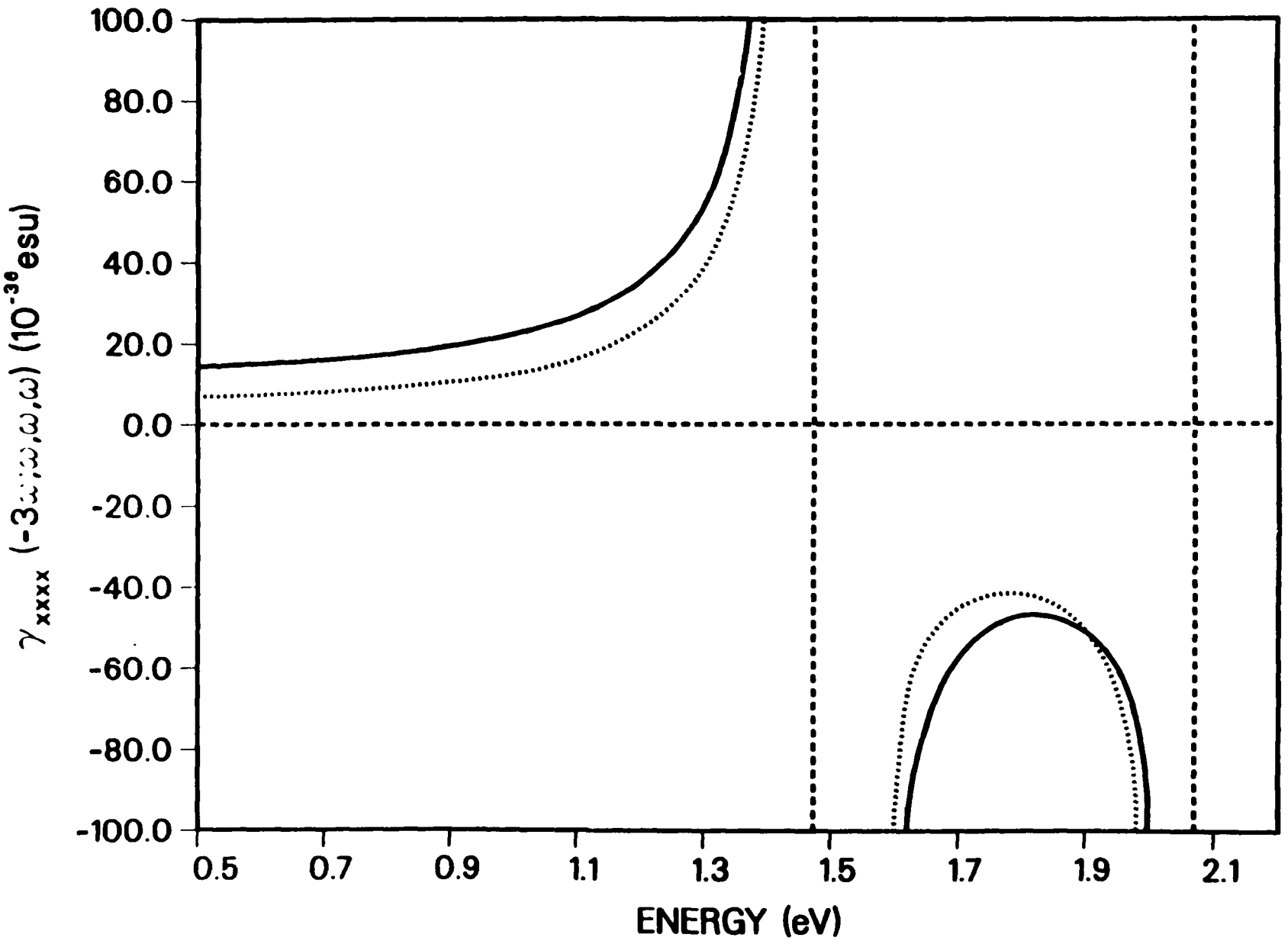
100.0
80.0
60.0
40.0
20.0
0.0
-20.0
-40.0
-60.0
-80.0
-100.0
0.5
0.7
0.9
1.1
1.3
1.5
1.7
1.9
2.1
ENERGY (eV)
γ_{xxxx} (-3ω;ω,ω,ω) (10^{-36}esu)

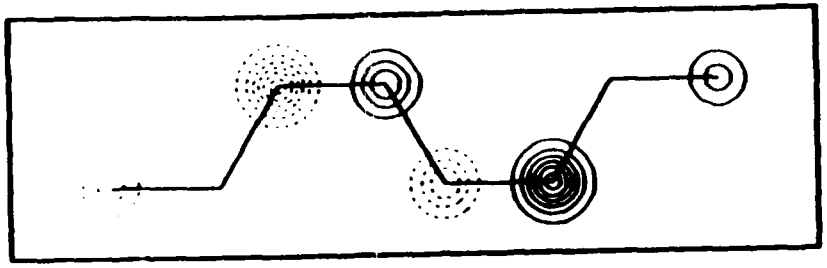

(a)

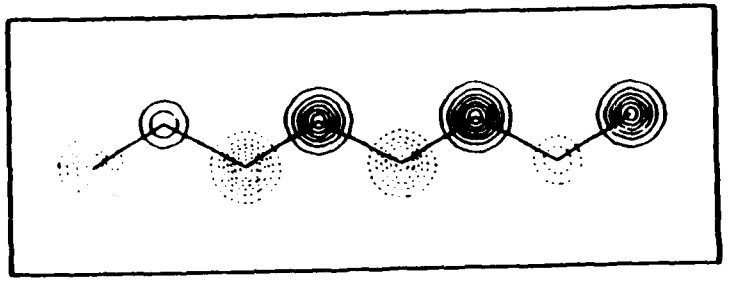

(b)

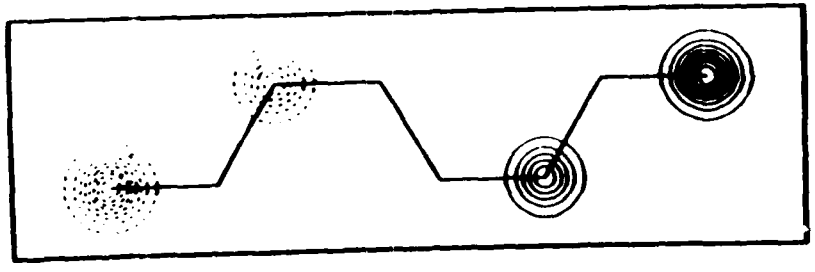

(c)

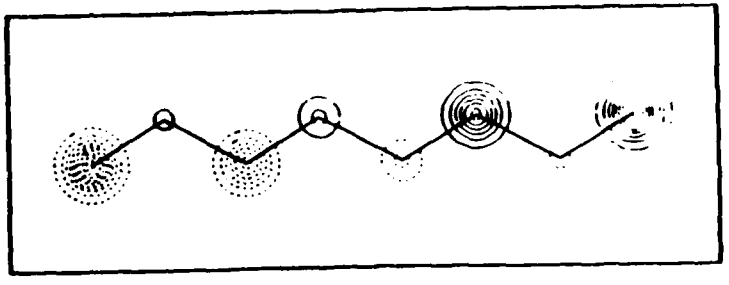

(d)

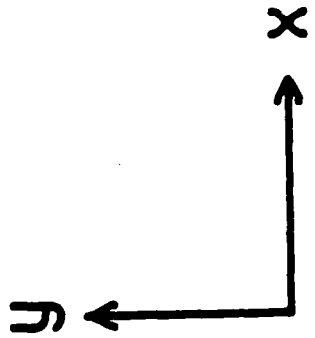
x

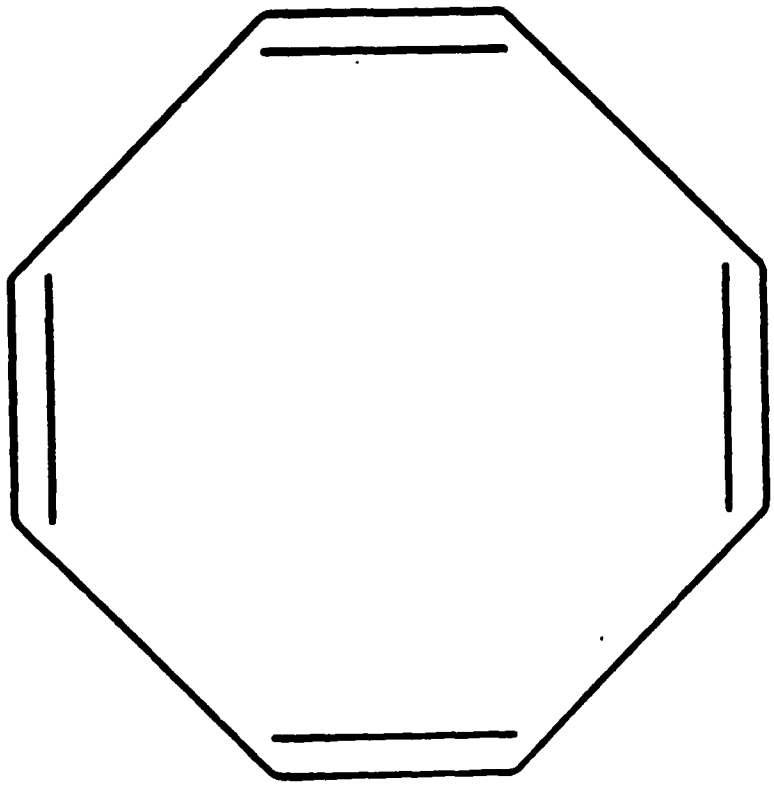

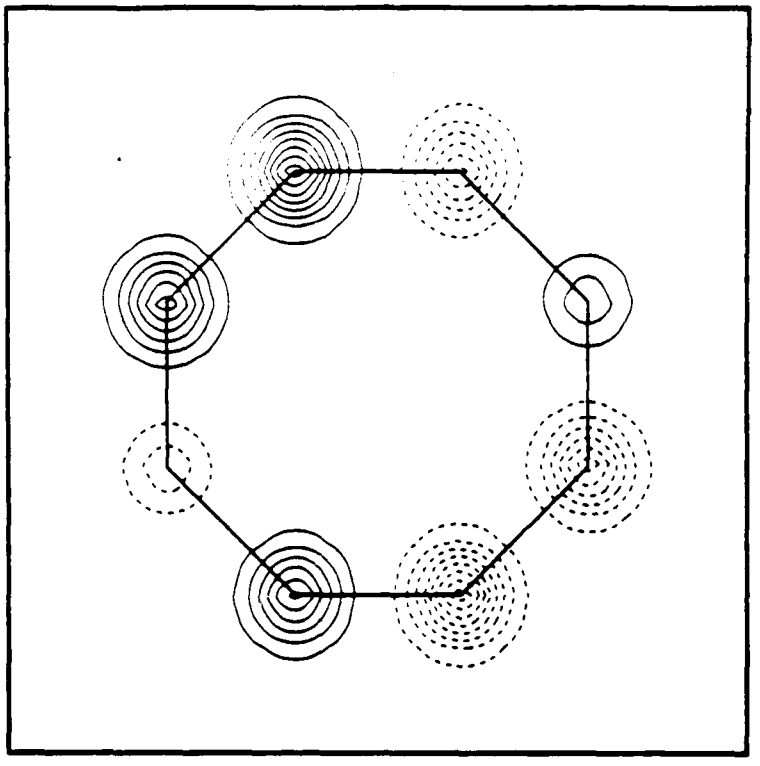

(a)

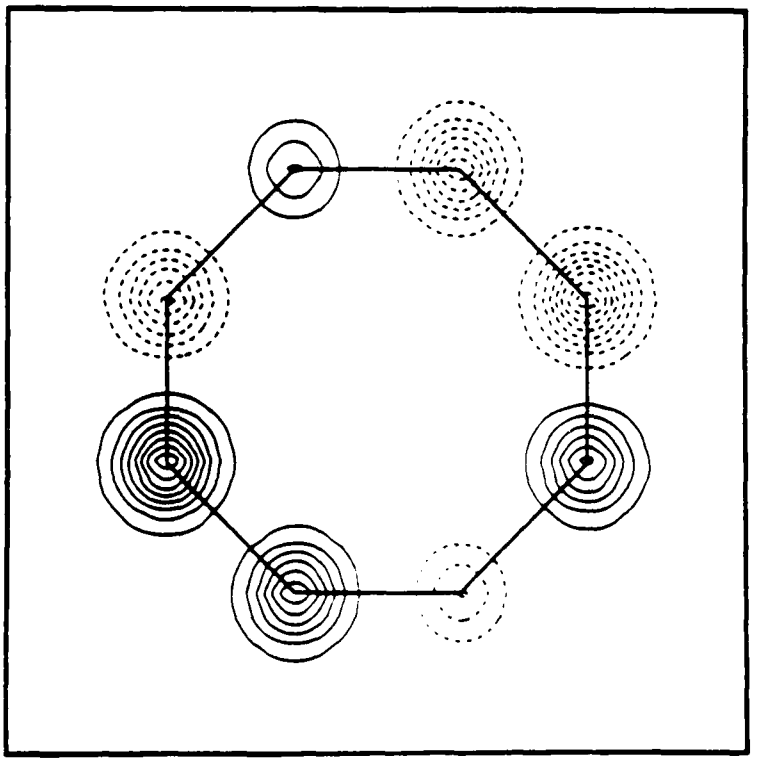

Figure 5

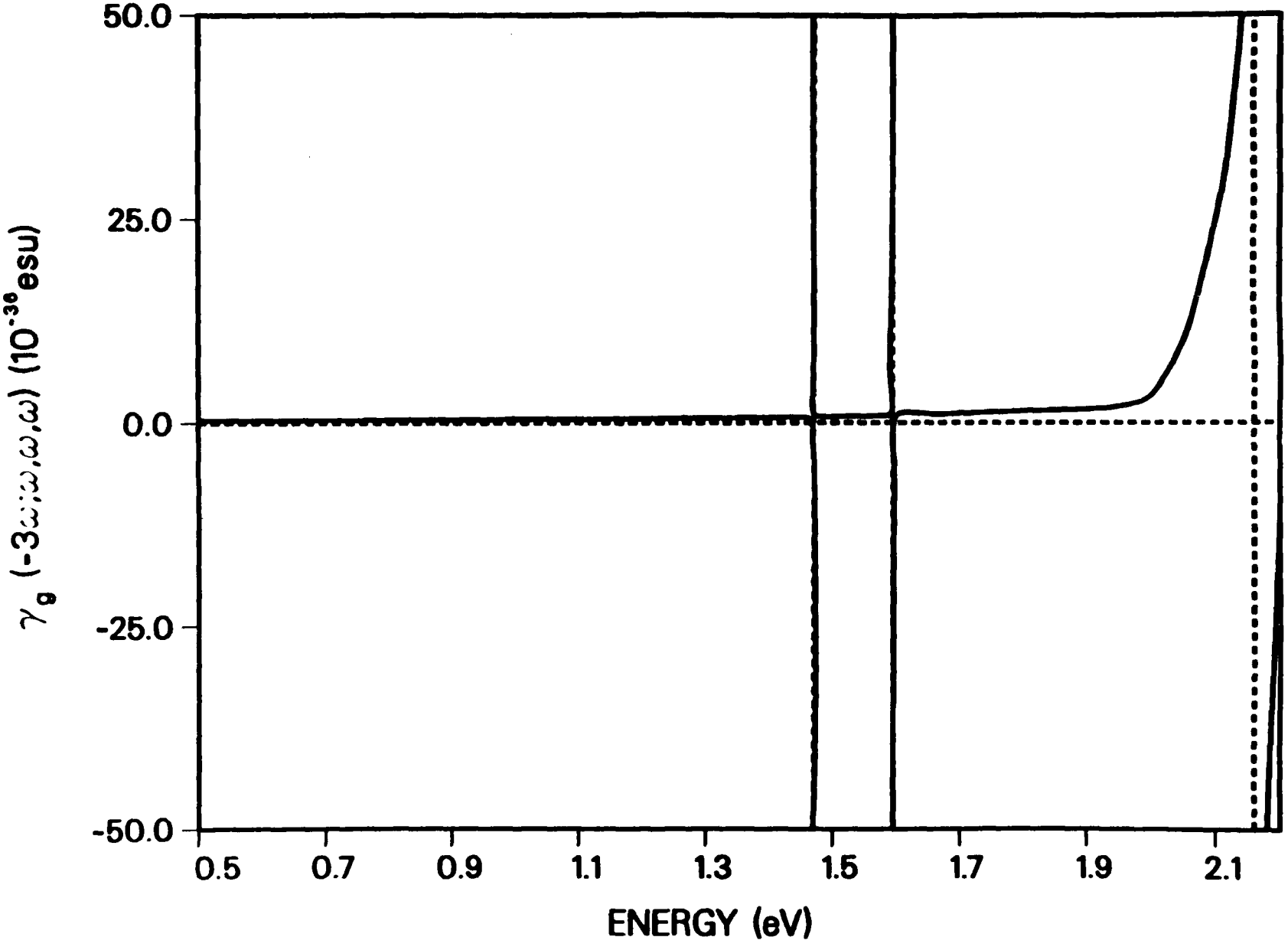
50.0
25.0
0.0
-25.0
-50.0
0.5
0.7
0.9
1.1
1.3
1.5
1.7
1.9
2.1
ENERGY (eV)
γ_g (-3ω;ω,ω,ω) (10^{-30}esu)

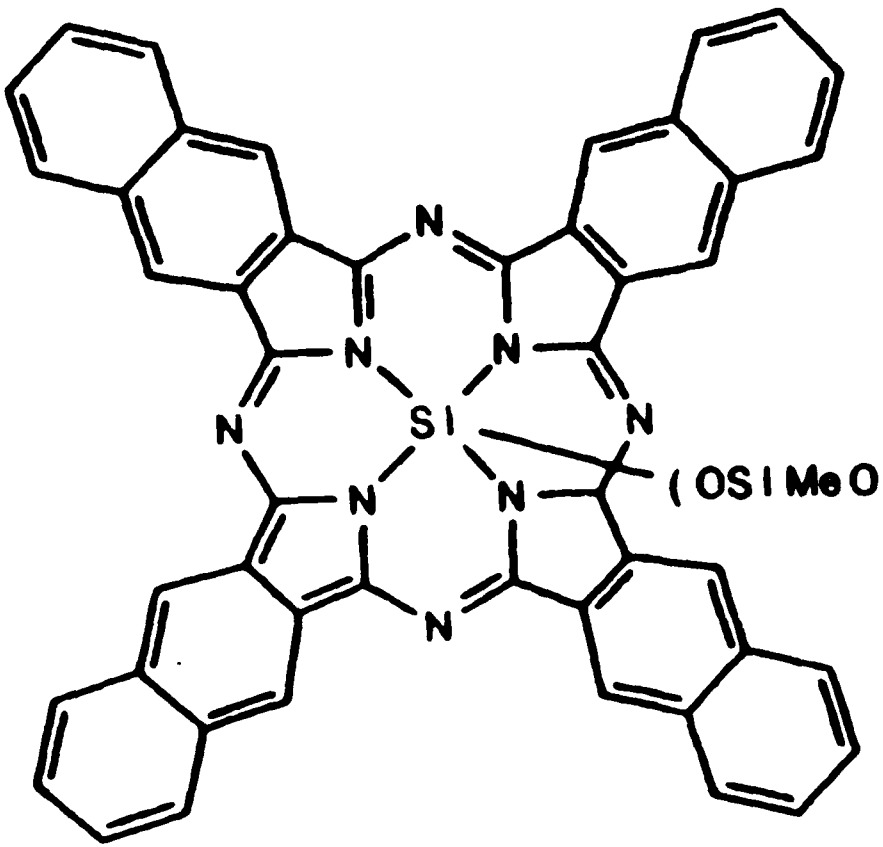

$$(OSiMeO(CH_2)_3NHC(=O)(CH_2)_8C(=O)NH(CH_2)_3OH)_2$$

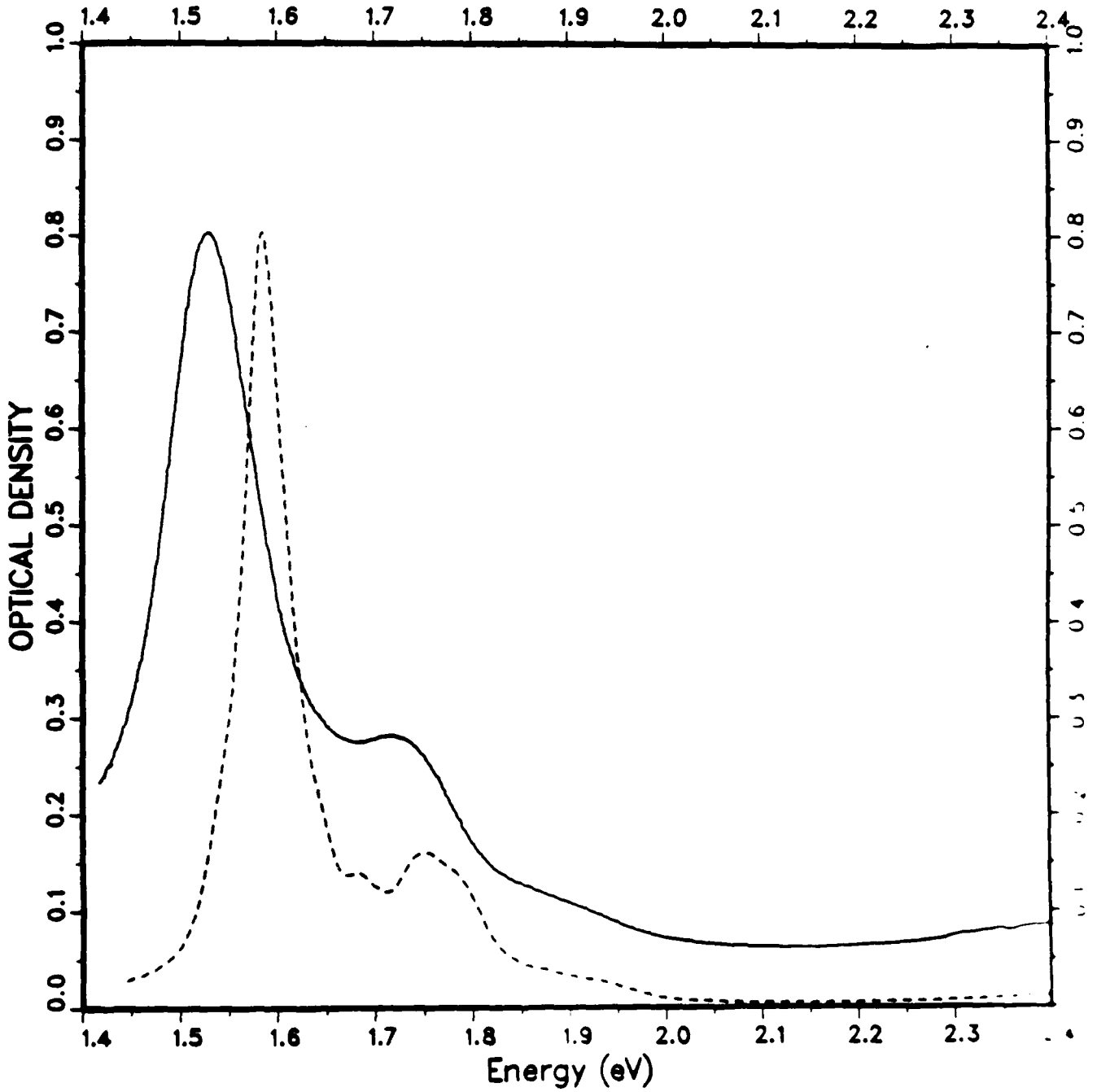
OPTICAL DENSITY
Energy (eV)
1.4
1.5
1.6
1.7
1.8
1.9
2.0
2.1
2.2
2.3
2.4
0.0
0.1
0.2
0.3
0.4
0.5
0.6
0.7
0.8
0.9
1.0

Figure

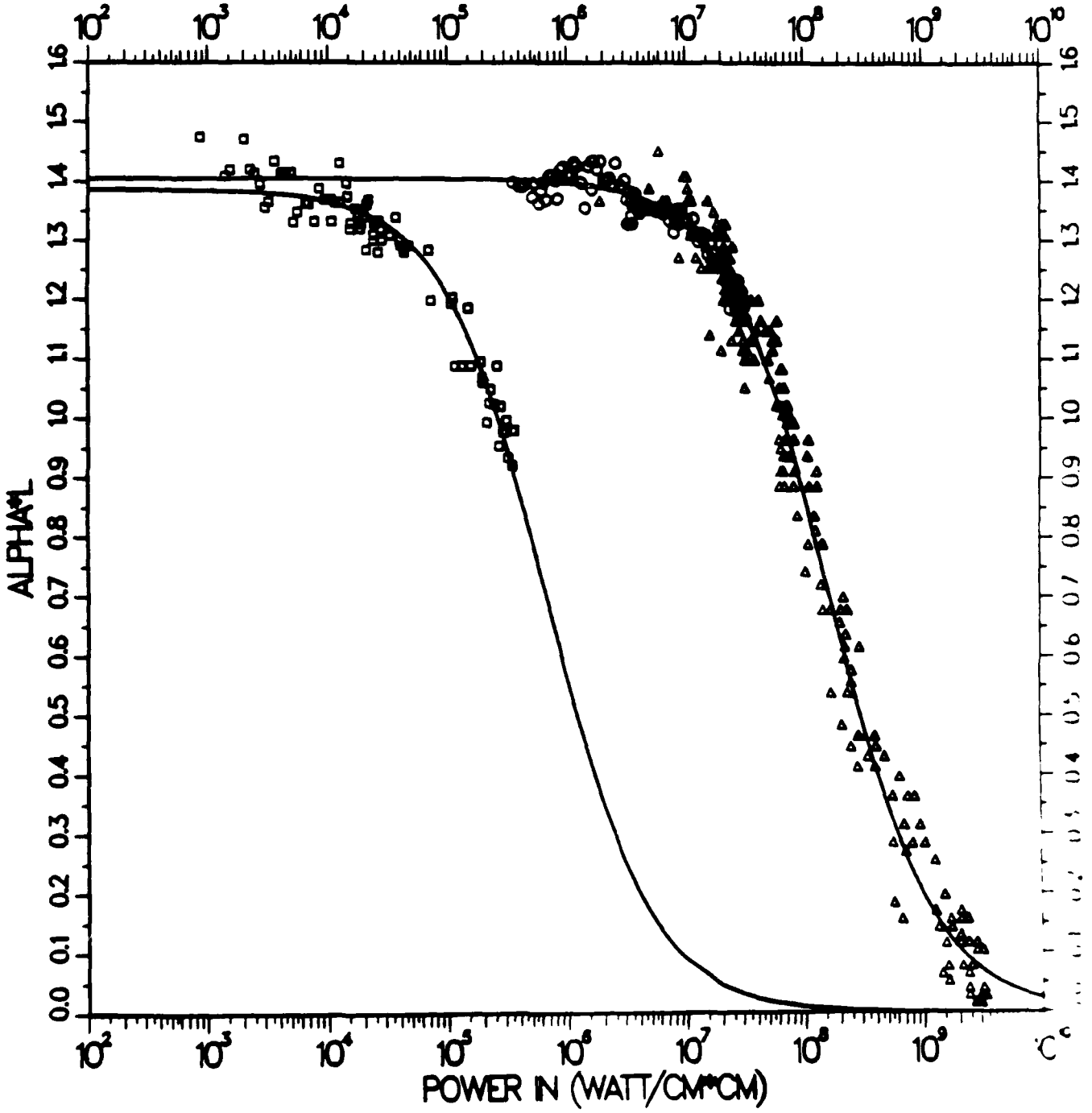

Figure 1

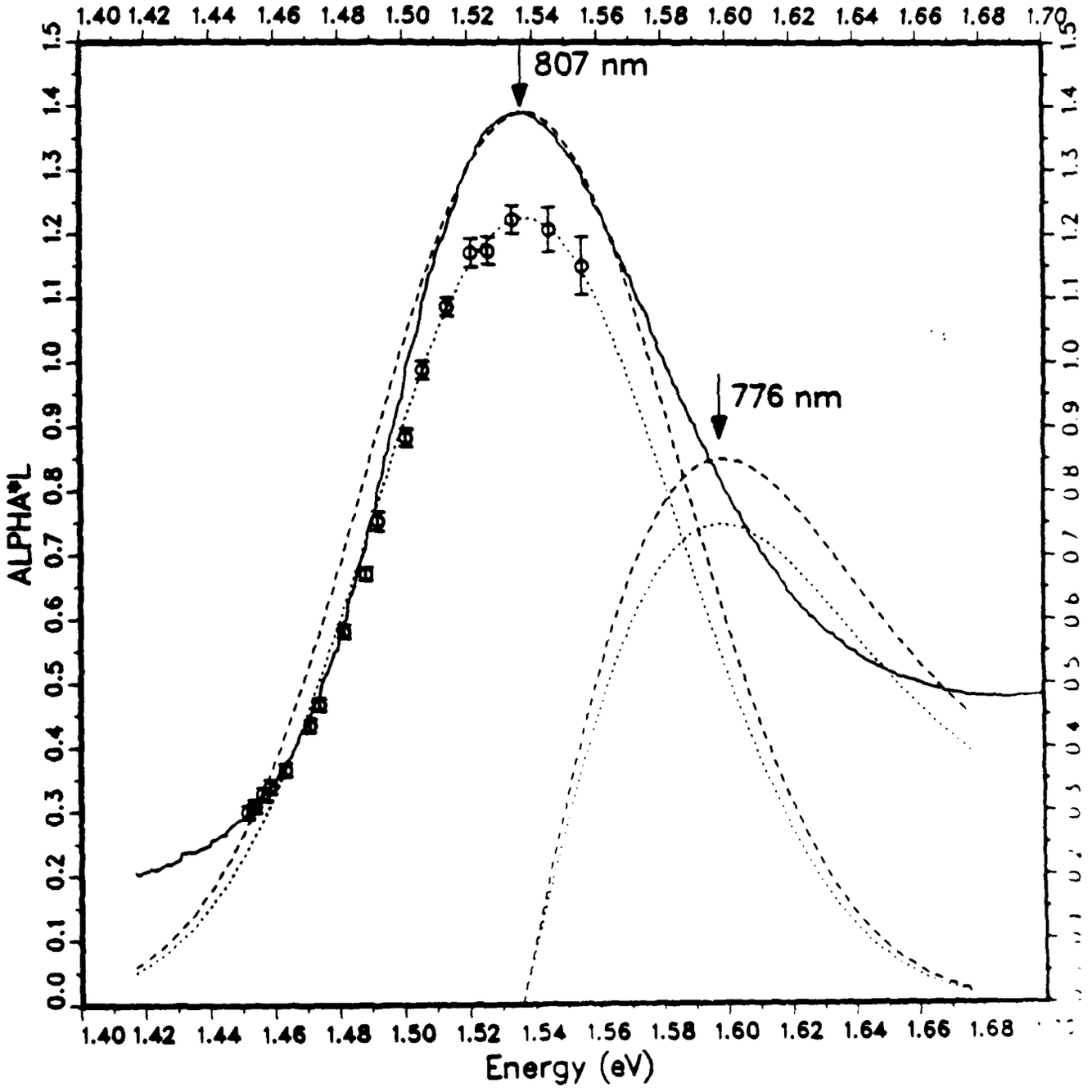
807 nm
776 nm
ALPHA*L
Energy (eV)
1.40 1.42 1.44 1.46 1.48 1.50 1.52 1.54 1.56 1.58 1.60 1.62 1.64 1.66 1.68 1.70
0.0 0.1 0.2 0.3 0.4 0.5 0.6 0.7 0.8 0.9 1.0 1.1 1.2 1.3 1.4 1.5

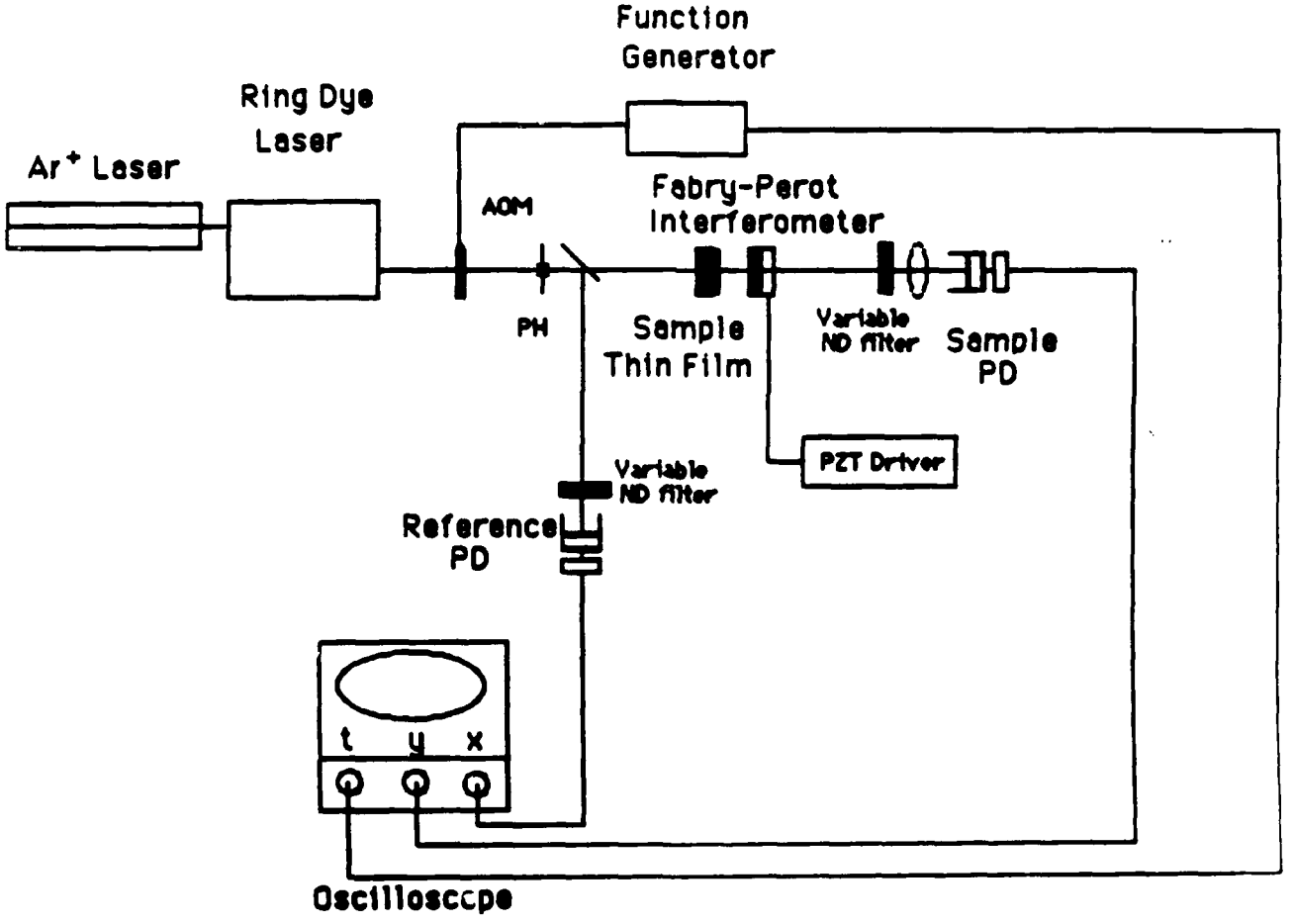
Function
Generator
Ring Dye
Laser
Ar+ Laser
AOM
Fabry-Perot
Interferometer
PH
Sample
Thin Film
Variable
ND filter
Sample
PD
PZT Driver
Variable
ND filter
Reference
PD
t
y
x
Oscilloscope

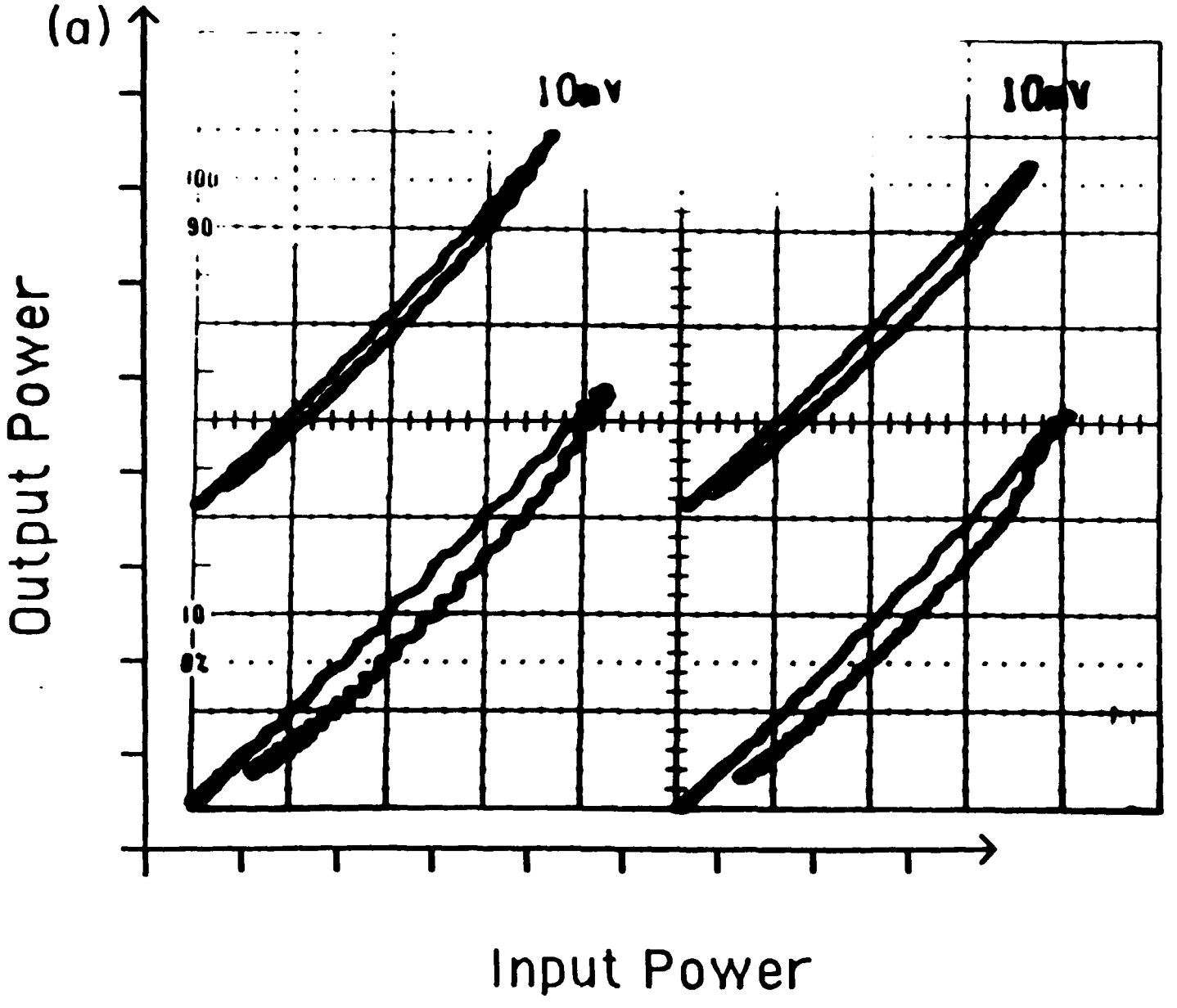
(a)
10mV
10mV
100
90
10
0
Output Power
Input Power

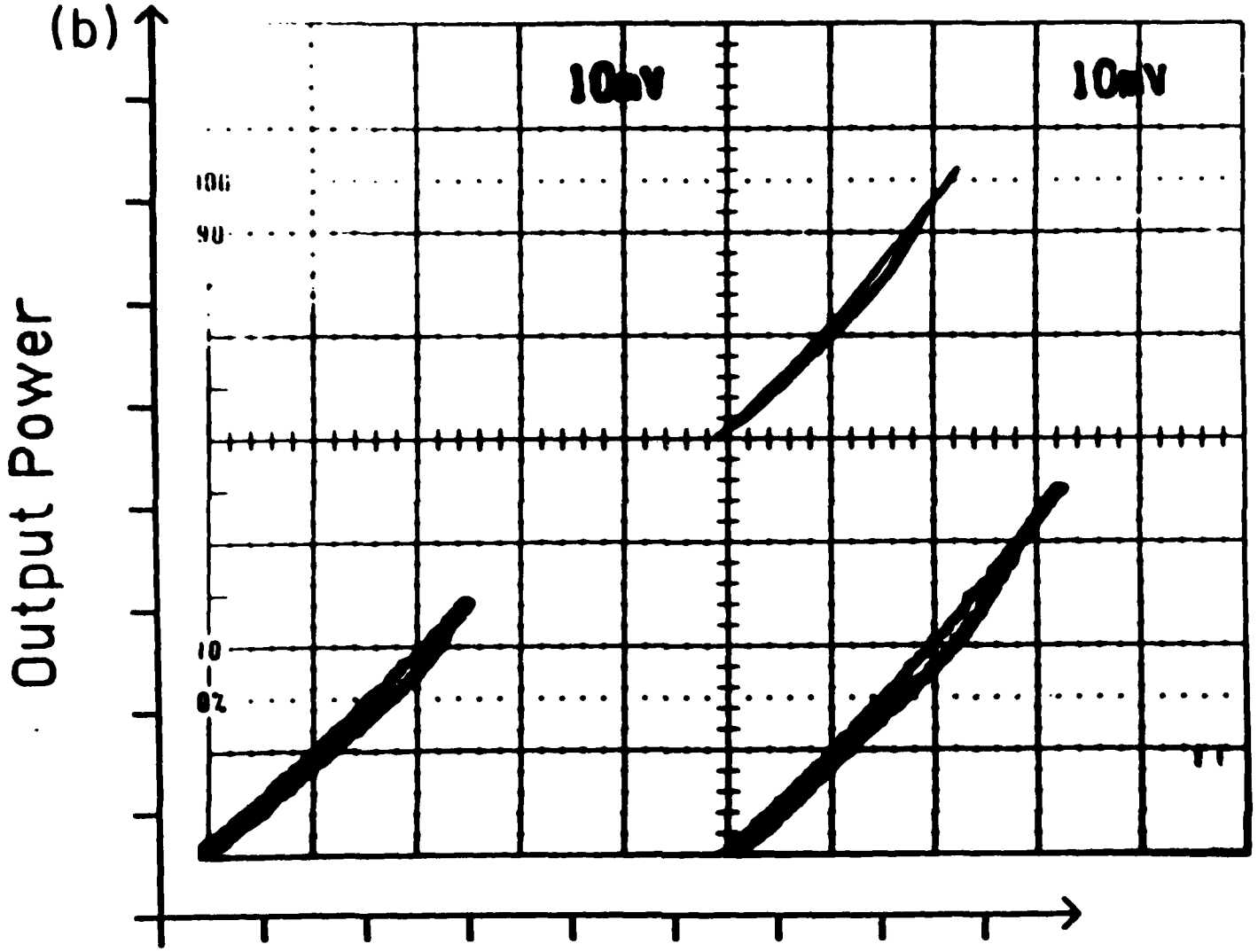
(b)
10dB
10dB
100
90
10
0%
Output Power
Input Power

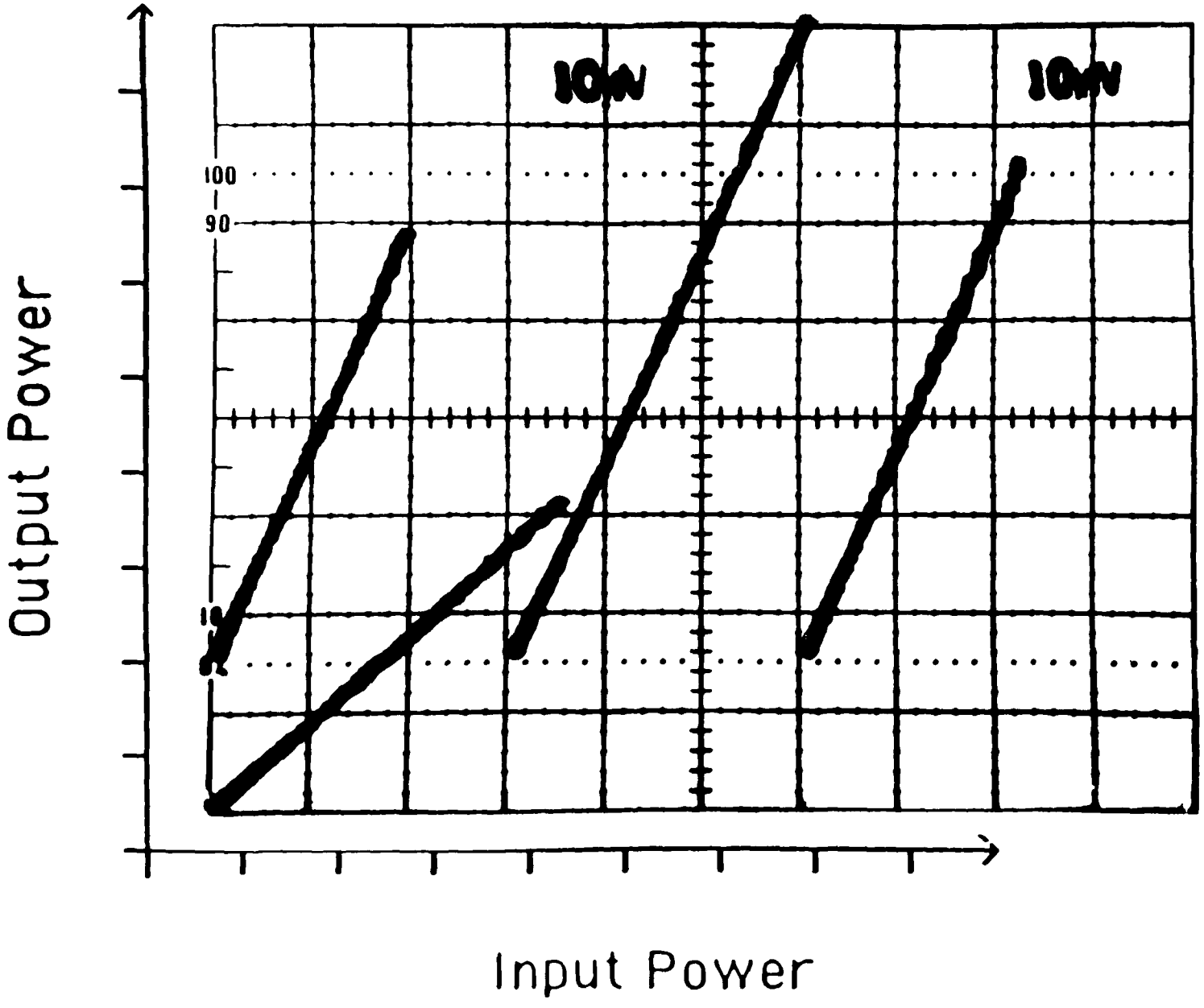
Output Power
100
90
10W
10W
Input Power

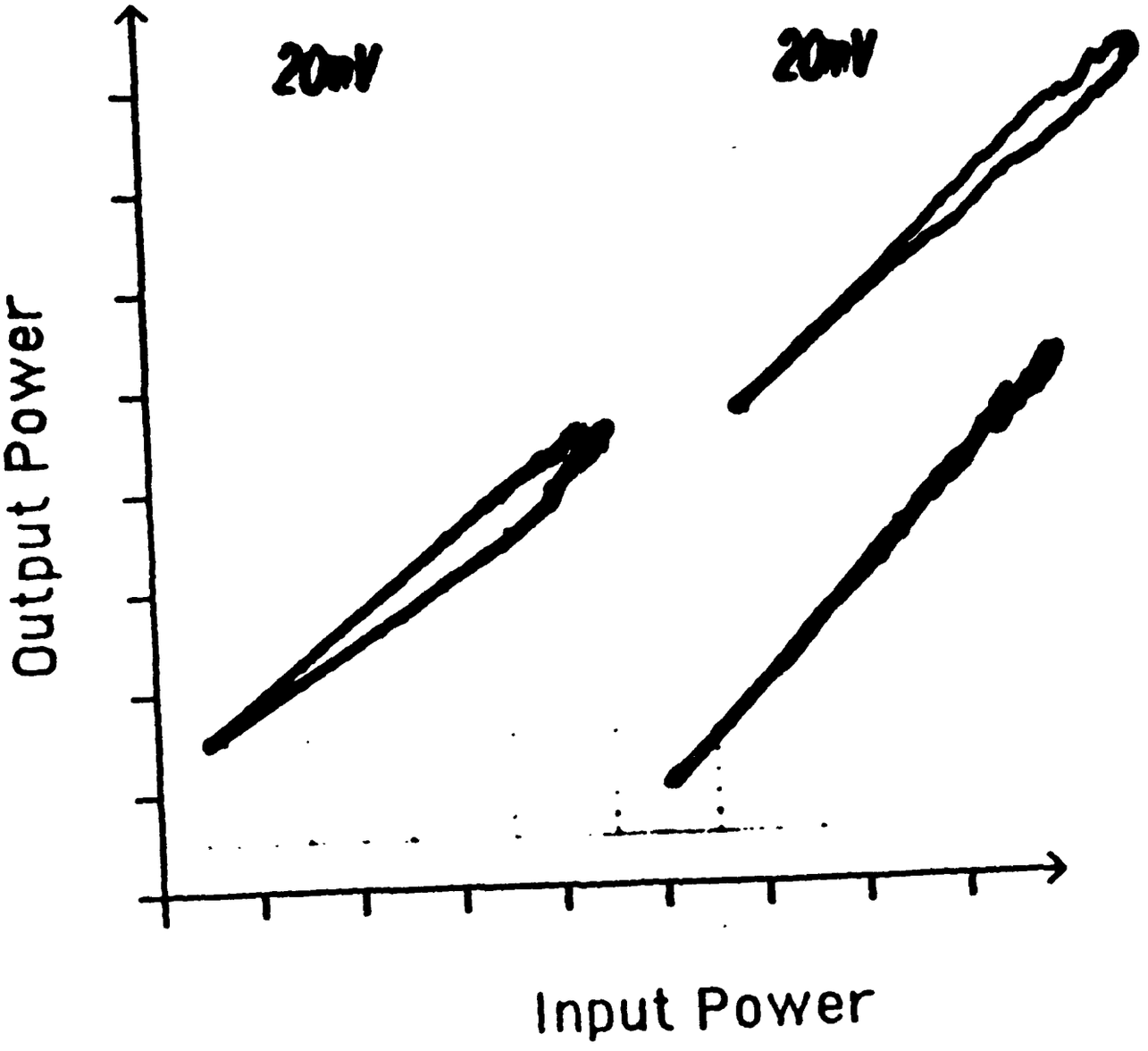
20mV
20mV
Output Power
Input Power

II. FREQUENCY DEPENDENCE OF THE OPTICAL KERR EFFECT AND THIRD ORDER ELECTRONIC NONLINEAR OPTICAL PROCESSES OF ORGANIC SYSTEMS

I. INTRODUCTION

The optical Kerr effect[1-5] (OKE) is a four wave mixing process in which an intense optical pump beam of frequency ω_1 induces depolarization in a probe beam of frequency ω_2 because of the third order nonlinear optical polarization $P_i^{(3)}(\omega_2)$. In an isotropic medium, $P_i^{(3)}(\omega_2)$ is expressed as

$$P_i^{(3)}(\omega_2) = \chi_{ijkl}^{(3)}(-\omega_2;\omega_1,-\omega_1,\omega_2)\, E_j(\omega_1)E_k(\omega_1)^*E_l(\omega_2), \qquad (1)$$

where $\chi_{ijkl}^{(3)}$ is the third order nonlinear optical susceptibility and $E(\omega_1)$ and $E(\omega_2)$ are the pump and probe fields, respectively. As extensively discussed in the review by Hellwarth,[6] at frequencies well above molecular vibration and rotation modes but below electronic resonances, $\chi_{ijkl}^{(3)}$ has contributions due to both electronic excitations and lattice displacements which in the Born-Oppenheimer approximation is expressed as the sum of the quantum averages σ_{ijkl} and D_{ijkl},

$$\chi_{ijkl}^{(3)} = F_L(\sigma_{ijkl} + D_{ijkl}), \qquad (2)$$

where σ_{ijkl} and D_{ijkl} are the third order electronic and lattice contributions, respectively, and F_L is a local field factor relating microscopic and macroscopic quanitities; both terms are assumed to be fast relative to experimental time scales.[7-9] In such a frequency regime, because of higher frequency electronic resonances nearby, the dominant frequency dependent term is the ultrafast electronic contribution, and, hence, frequency dependent measurements of the total OKE response can allow direct determination of the resonant electronic and nonresonant contributions to $\chi^{(3)}$. This is similar to the approach of Levenson, et. al.,[10,11] where the nonresonant contribution was determined by comparing OKE measurements with complementary Raman scattering data (Raman-induced Kerr effect or RIKES). The present work aims to determine the

separate resonant electronic and nonresonant contributions from OKE data over a large frequency range.[12]

The purpose of this paper is to provide an experimental and theoretical study and review that enables frequency dependent OKE results to be obtained from optimized pump-probe techniques. In Section 2, the probe beam depolarization is theoretically analyzed in terms of experimentally measured quantities with special attention paid to several standard approximations. Section 3 describes the experimental pump-probe design and the formalism required for the data analysis. Section 4 presents experimental results for the frequency dependent measurements of $\chi^{(3)}_{ijkl}(-\omega_2;\omega_1,-\omega_1,\omega_2)$ for the Kerr liquids benzene and nitrobenzene. In Section 5, electronic and lattice mechanisms are discussed. A simple model is presented to describe the dispersion of sum-frequency and difference-frequency resonances in benzene and nitrobenzene in terms of their linear absorption spectra and dipole selection rules, and to obtain the resonant and nonresonant contributions to $\chi^{(3)}_{ijkl}(-\omega_2;\omega_1,-\omega_1,\omega_2)$ for the two liquids.

2. THEORETICAL APPROXIMATIONS

In this section, explicit account is given for approximations and assumptions required for optimizing the experimental design of OKE measurements using pump-probe techniques. The plane wave limit is considered under the conditions that the probe beam waist is small relative to the pump waist and that the effects of the pump on the probe are the same everywhere on the transverse profile of the probe. Also, both the probe and pump beam profiles have waists whose diffraction and self-focusing lengths are much longer than the sample interaction length, insuring that the pump and the probe beams at small crossing angles will result in a uniform effect on the probe beam throughout this interaction region. Since the peak power of the pump beam in the present study is enough to produce a measurable refractive index change, unfocused beams are used allowing a long interaction length that minimizes extraneous nonlinear effects such as those

from the sample cell windows. The pump-probe conditions are reviewed in terms of Maxwell's equations in the following discussion.

In an isotropic medium, the nonlinear interaction between an intense spatially delocalized pump field, $\mathbf{E}_1$, and a weak probe field, $\mathbf{E}_2$, mediated by an optical Kerr-like medium with a scalar third order susceptibility, $\chi^{(3)}(-\omega_2;\omega_1,-\omega_1,\omega_2)$, is expressed by the nonlinear Maxwell equation:

$$-\nabla^2\mathbf{E} = -\frac{1}{c^2}\frac{\partial^2}{\partial t^2}\left[\varepsilon_o\mathbf{E} + 4\pi\chi^{(3)}(\mathbf{E}\cdot\mathbf{E})\mathbf{E}\right], \tag{3}$$

where the total electric field is composed of the pump and probe fields,

$$\mathbf{E} = \mathbf{E}_1 + \mathbf{E}_2. \tag{4}$$

With terms retained only to first order in $\mathbf{E}_2$ in Equation (3), the pump intensity acts as a source term in the wave equation for the probe.

For plane waves, $\mathbf{E}_1$ and $\mathbf{E}_2$ are given by

$$\mathbf{E}_1 = \frac{1}{2}[A_1 e^{i\phi_1} + \text{c.c.}]\,\mathbf{x}, \tag{5}$$

and

$$\mathbf{E}_2 = \frac{1}{2}[A_2 e^{i\phi_2}(e^{i\delta(z)}\cos\theta\mathbf{x} + \sin\theta\mathbf{y}) + \text{c.c.}], \tag{6}$$

where

$$\phi_1 = k_1 z - \omega_1 t + \phi(z), \tag{7}$$

$$\phi_2 = k_2 z - \omega_2 t, \tag{8}$$

$\phi(z)$ is the intensity dependent phase shift of the pump, θ the angle that the polarization vector of the probe makes with that of the pump at the sample entrance ($z=0$), $\delta(z)$ a phase shift induced in the probe by the pump, and A_1 and A_2 may be assumed constant if the beams approximate plane waves in the measured region. Equation (5) assumes that all the effects of the probe on the pump are negligible so that the pump remains linearly polarized at all points in the interaction region. Note that the wide pump waist implies that the phase shift, $\delta(z)$, is independent of the transverse coordinate resulting in a uniform phase shift in the transverse plane. Without this assumption, the measurement would require knowledge of the probe phase everywhere in the detection plane, or the use of a deconvolution analysis, that would greatly complicate data interpretation. If $\phi(z)$ or $\delta(z)$ is complex, then for each quantity the real part corresponds to an intensity dependent phase shift while the imaginary part describes intensity dependent absorption. In either case, there results a polarization change in the probe beam.

Equation (3) can be Fourier analyzed to obtain the equations satisfied by the pump and probe beams. We assume that the induced nonlinearity is small enough that the phase changes negligibly on wavelength scale. The phase change of the probe beam due to the pump is then:

$$\delta(z) = \frac{3k_2\pi|A_1|^2 z}{\varepsilon(\omega_2)}\,\chi^{(3)}(-\omega_2;\omega_1,-\omega_1,\omega_2), \tag{9}$$

The output to input ratio of the probe beam in a Kerr shutter is

$$\frac{P_{out}}{P_{in}} = \sin^2(2\theta)\sin^2\left[\frac{3k_2\pi|A_1|^2 L}{2\varepsilon(\omega_2)}\,\chi^{(3)}(-\omega_2;\omega_1,-\omega_1,\omega_2)\right], \tag{10}$$

where L is the interaction length in the sample. In the limit of small nonlinearities we can solve Equation (10) for $\chi^{(3)}$

$$\chi^{(3)}(-\omega_2;\omega_1,-\omega_1,\omega_2) = [\frac{P_{out}}{P_{in}}]^{1/2} \frac{2\varepsilon(\omega_2)}{3k_2\pi|A_1|^2|L\sin(2\theta)|}. \quad (11)$$

It is significant to note that Equation (11) is only valid when the argument in brackets in Equation (10) is small as required by the slowly varying phase approximation; otherwise, the formalism fails and higher order effects will also contribute, contrary to the assumptions of small refractive index change. If $\delta(z)$ is complex ($\delta(z) = \delta_R(z) + i\delta_I(z)$), the solutions follow a parallel development where $\sin^2(\delta/2)$ is replaced with $\sin^2(\delta_R/2)+\sinh^2(\delta_I/2)$, which in the small argument limit becomes $(\delta_R/2)^2 + (\delta_I/2)^2$. Equation (11) can then be generalized by replacing $\chi^{(3)}$ with $|\chi^{(3)}| = ((\chi^{(3)}_R)^2 + (\chi^{(3)}_I)^2)^{1/2}$.

At this point, it is worthwhile to discuss the approximations we have employed in arriving at Equation (11) and how well the experimental parameters obey the assumptions. For a Gaussian pump beam of initial beam waist a, $\nabla\cdot E$ is negligible in the nonlinear wave equation under the following conditions:[13]

$$\frac{\lambda^2}{\pi^2 a^2 f^2} << 1, \quad (12)$$

$$\frac{2r^2}{a^2} << 1, \quad (13)$$

and

$$\frac{z^2}{R_{NL}^2} << 1. \quad (14)$$

We further require the probe beam to be contained by the pump

$$\frac{2a_2^2}{a^2 f^2} << 1, \quad (15)$$

where a_2 is the probe beam waist. Here, f is the normalized pump beam width ($f = \frac{w}{a}$), w is the beam width as a function of z, λ the wavelength, r the radial distance from the symmetry axis in a plane transverse to the propagation direction, z the distance along the propagation direction, and R_{NL} is the nonlinear radius of curvature of the beam defined as

$$R_{NL} = a \left[\frac{\varepsilon_o}{3\pi\chi^{(3)}|A_1|^2} \right]^{1/2}. \qquad (16)$$

In the experiments described here, we have $\lambda = 1$ μm, a = 0.5 cm, f~1, z~200 cm, $|A_1|^2 = 3.45 \times 10^5$ ergs/cm^3, $\chi^{(3)} \sim 1 \times 10^{-13}$ esu, and $\varepsilon_o^{1/2} = 1.5$. Thus, typically $\lambda^2/\pi^2 a^2 f^2 \sim 4.1 \times 10^{-9}$ and $z^2/R_{NL}^2 \sim 0.05$ satisfy conditions (12) and (14), respectively.

In summary for the plane wave analysis to be valid, the sample length must be much shorter than both the diffraction length and self-focusing length scale, and the probe beam must be totally contained within the central portion of the pump beam. Moreover, the phase shift of the probe introduced by the pump must be small on the scale of the probe beam wavelength.

3. EXPERIMENTAL

3.1 APPARATUS

The experimental layout is shown in Figure 1. A mode-locked Nd:YAG laser (Quantel 401C) is used as the pump and a frequency stabilized argon ion laser (Spectra Physics 165) or frequency stabilized ring dye laser (Spectra Physics 380B) is used as the probe. The Nd:YAG pump laser beam is split into four pieces by beamsplitters BS1 and BS2, so that two of the resulting beams are used to pump the sample (S) and reference (R) Kerr cells defined by polarizers P1/A1 and P2/A2 respectively. The other two Nd:YAG beams are optically delayed with stepping motor controlled near-infrared mirror pairs (YM1/MDM1, YM2/MDM2) and recombine with the Kerr signal at the optical gate (KDP). Similarly, the cw argon ion or dye probe laser beam is split between the sample and reference arms. A weak reflection from the half wave plate HWP1 illuminates the photodiode that gates the electronic data acquisition system

The probe beam frequency stabilization prevents mode hopping, which insures that the beam is continuous wave on picosecond time scales. High power near infrared interference filters are used variously as beamsplitters or mirrors, and, when possible 45-45-90 prisms steer the beams by total internal reflection. Glan-Taylor prisms are used in the Kerr cell because of their high rejection rates, and an interferometrically aligned quartz sample cell prevents probe beam depolarization, refraction and scattering. The optically gated signal is detected with a photomultiplier tube (RCA C31034-A02), and the subsequent current pulse is in turn sent to a disciminator, a CAMAC gated integrator (LeCroy 2249W), and finally to a microcomputer (DEC PDP 11/23) for analysis.

Since only nonfocused laser beams are used, requirement (13) is satisfied. Present experiments used Nd:YAG lasers of 3-7 mm width and cw dye and Ar^+ lasers of 1-2 mm width consistent with Equation (15). Also, the central part of the measured beam profiles are consistent with the parabolic approximation of self-focusing calculations except for the small dip at the origin (Figure 2). If the beam crossing angle is adjusted between two runs, this dip could result in a ±8% change in the probed pump power if the area of beam overlap changes. When relative values of n_2 are measured between two samples, this can result in a total uncertainty in this ratio of about 16%. As long as no adjustments are made in the overlap regions, the relative frequency dependence of the third order susceptibility of a sample will be correct within the statistical uncertainty of each data point. Small nonlinear phases ($\delta << 1$) were obtained by employing a 2 cm long sample cell and Nd:YAG lasers delivering a total peak power of $P_T = 1 \times 10^{13}$ erg/sec This places a limit on the lowest measurable value of n_2, which in the present study is 10^{-14} esu.

Any Kerr cell experiment must address the problem of stray light getting through the crossed polarizers and possibly saturating the detector. This background is particularly significant in the current measurements since a cw probe laser is employed that results in an average signal to noise ratio of 10^{-9}. The use of a pulsed pump and pulsed probe would permit gating via synchronization but would also present difficulty in separating true nonlinear optical

processes from possible pulse-noise interactions and effects; thus, we use a pulsed pump/cw probe arrangement with an optical gating technique.

A KD^*P parametric mixing crystal is used to combine the Kerr cell signal at frequency ω_2 and a portion of the Nd:YAG laser output at frequency ω_1 to create ultraviolet output at the sum frequency $\omega_3=\omega_1+\omega_2$ by noncollinear phase matching. The unwanted light at ω_1 is filtered (spatially and/or spectrally) allowing only the ultraviolet sum frequency light to reach the detectors. Only when the pulse of light emerging from the Kerr cell is synchronized with the pump laser arriving at the KD^*P crystal will any signal be detected (temporal filtering). If operation of the Kerr cell is blocked or if the two pulses are not synchronized, no output is obtained from the optical gate. Accurate synchronization of picosecond pulses is achieved using a motorized near-infrared mirror for optical delay. Hence, the Kerr cell combined with the optical gate provides a highly efficient means for reliably determining whether true OKE signal is being detected. The optical gate up-converts 10 to 20 percent of the signal, and the efficiency of the gate is monitored as a function of the input parameters such as laser frequency and intensity, crossing angle in the crystal, etc. When properly used, the optical gate is an essential component in $\chi^{(3)}$ experiments using cw probes by providing high signal to noise ratios and straightforward deconvolution of the Kerr signal. Furthermore, the optical gate can be easily modified for time resolved studies through auto/cross correlation measurement techniques.[14]

3.2 DATA ANALYSIS

A data acquisition system employing a sample and reference arm measures the time integrated power of each laser shot during the electronic gate. The integrated charge spectrum of at least 1000 laser shots is tracked over time and stored and the centroid of the distribution (average number of photons per event) is calculated. A typical pulse height distribution of signal of about 10,000 events shows the expected Poissonian form (Figure 3). The centroid is expressed as the time integrated power of the instantaneous signal power, $P_{out}(t)$, and for a single pulse the contribution is,

$$C(\omega_2) = G(\omega_2) \int_{-\Delta t/2}^{+\Delta t/2} P^{\omega 2}_{out}(t)dt, \tag{17}$$

where $G(\omega_2)$ is the detection gain and Δt is the width of the gate in the detection electronics. For Δt much larger than the temporal pulse width, $C(\omega_2)$ can be expressed as

$$C(\omega_2) = P^0_{out}(\omega_2)G(\omega_2) \int_{-\infty}^{+\infty} q(t)dt, \tag{18}$$

and the measured pump energy, E,

$$E = \frac{c}{8\pi}(A_1^0)^2 A \int_{-\infty}^{+\infty} r(t)dt, \tag{19}$$

where $P^0_{out}(\omega_2)$ and A_1^0 are the peak power and peak field values, respectively, A the area of the pump beam, c the speed of light, and q(t) and r(t) are dimensionless pulse shape functions having their respective maximum values of unity at t=0. Substituting Equations (18) and (19) into equation (11), we obtain

$$\chi^{(3)}(-\omega_2;\omega_1,-\omega_1,\omega_2) = \left[\frac{C(\omega_2)}{G(\omega_2)P_{in}(\omega_2)}\right]^{1/2} \frac{\varepsilon(\omega_2)}{k_2 EL} \frac{Ac}{12\pi^2 \sin(2\theta)} \frac{\int_{-\infty}^{+\infty} r(t)dt}{\left[\int_{-\infty}^{+\infty} q(t)dt\right]^{1/2}}. \tag{20}$$

A reference arm is used to eliminate the effects of pump beam power fluctuations. The reference arm can use either the same probe as the sample arm, or a separate laser source. In the former case, it is necessary to choose a reference material with negligible dispersion in $\chi^{(3)}$ over the probe tuning range. The latter case is easier to realize experimentally, but the former has the advantage of eliminating pump and probe power fluctuations simultaneously. In the dual probe configuration with all variables relevant to the reference arm labeled as prime, the relative χ from Equation (20) is given as

$$\chi^{(3)}(-\omega_2;\omega_1,-\omega_1,\omega_2) \Rightarrow \left[\frac{C(\omega_2)/C'(\omega_r)}{P_{in}(\omega_2)G(\omega_2)/G'(\omega_r)} \right]^{1/2} n(\omega_2)\lambda_2, \tag{21}$$

where $C(\omega_2)$ and $C'(\omega_r)$ are the measured centroids, ω_r the reference frequency, $n(\omega_2)$ the linear refractive index at ω_2, and $P_{in}(\omega_2)$ is monitored periodically. In deriving Equation (21), it is assumed that the reference arm probe frequency is fixed. The detection gain, $G(\omega_2)$ is written as

$$G(\omega_2) = \alpha G_{pmt}(\omega_2)G_{og}(\omega_2), \tag{22}$$

where $G_{og}(\omega_2)$ is the gain of the optical gate, $G_{pmt}(\omega_2)$ the total gain of the photomultiplier tube, and the constant α depends on the experimental geometry. Since

$$G_{og}(\omega_2) = M(\omega_2)P_{pump}, \tag{23}$$

where $M(\omega_2)$ is a crystal tuning parameter for KD^*P, Equation (22) yields

$$\frac{G(\omega_2)}{G'(\omega_r)} = \left\{ \frac{\alpha}{\alpha' M'(\omega_r)G'(\omega_r)_{pmt}} \right\} G_{pmt}(\omega_2)M(\omega_2). \tag{24}$$

The bracketed term in (24) is constant throughout the experiment in the dual probe configuration, and the last two factors can be measured as follows. If we define $P_\perp$ as the Kerr effect power emerging from the crossed polarizers, P_s the light passing through the crossed polarizers due to depolarization from sample imperfections, and P_u the power permitted to pass through by slight uncrossing of the analyzer, then the total power, P_{out}, reaching the optical gate is

$$P_{out} = P_s + P_u + P_\perp. \tag{25}$$

The purpose of uncrossing the polarizers by a small amount is to tap out a known amount of probe light in the same spatial direction and position as the signal beam. Operation of the optical gate with this known light level is then used to calibrate the gate as follows. A cw power meter measures P_s when the polarizers are crossed and the pump beam is off; $P_s + P_u$ is measured when the polarizers are slightly uncrossed and the pump beam is off. Similarly, the crossed and uncrossed Kerr measurements with the pump on yield centroids corresponding to light at the probe frequency entering the optical gate with power $P_s + P_\perp$ and $P_s + P_u + P_\perp$, respectively. The gain of the optical gate, $G(\omega_2)$, is the ratio of the measured signal centroid corrected for the background light detected by the PMT and the known input intensity and is given by

$$G_{pmt}(\omega_2)M(\omega_2) = \frac{S_u(\omega_2)-S(\omega_2)}{(P_s+P_u)-P_s}, \tag{26}$$

where $S(\omega_2)$ is the signal centroid from the sample normalized to the reference when the polarizers are crossed, and $S_u(\omega_2)$ is the signal centroid when the polarizers are slightly uncrossed. Substituting Equations (26) and (24) into Equation (21), we finally obtain

$$\chi^{(3)}(-\omega_2;\omega_1,-\omega_1,\omega_2) \Rightarrow \left[\frac{S(\omega_2)(P_s+P_u)-S_u(\omega_2)P_s}{P_{in}(S_u(\omega_2)-S(\omega_2))}\right]^{1/2} n(\omega_2)\lambda_2. \tag{27}$$

The values of quantities in Equation (27) are directly experimentally measurable.

The single shot-to-shot referencing of the present experiment should be contrasted with signal averaging techniques. Clearly, in either case, random fluctuations can be reduced by taking more data; however, in terms of systematic errors, the methods are different. Many optics experiments have the tendency to drift over time and can be quantified by a time constant, t_D, that is defined as the elapsed time between optimal alignment and drift to the e^{-1} point of the measured signal relative to some quasi-static baseline. In the single shot-to-shot experiment, the referenced signal is mostly sensitive to inequalities between the drift rates of the two arms of the experiment (t_{D_s}-t_{D_r}). Laser pulse shape and amplitude fluctuations can systematically skew the data by time

of their unknown distributions. With the single shot referencing method, shape and amplitude changes are divided out for each individual pulse, thus eliminating any need for knowledge of the shape and amplitude distributions.

Often, in time domain studies, a temporal pulse shape is simply assumed.[3,15,16] Even if temporal profiles are known, theoretical calculations sometimes require approximating the profile by some simple function. In the signal averaging case, the sample is measured either before or after the reference, hence the results obtained from reversing the orders can be averaged to minimize drift error. The final referenced signal in the signal averaging case, however will include a quotient of sums of pulse amplitudes and shapes from the two separate experimental runs. The value of this quotient cannot be predicted without some a priori knowledge of the system behavior, even though the general behavior of the system can be very well quantified.[17] Hence, the single shot technique minimizes errors owing to laser fluctuations induced by natural factors such as temperature change, building vibrations, and power line surges as well as inherent instabilities.

4. RESULTS

4.1 THERMAL EFFECTS

In a pump-probe experiment absorptive beam heating effects can cause changes in the sample density and hence in the sample index of refraction. Probe heating can lead to thermal defocusing of the signal that results in spurious variations in the optical gate efficiency as well as changes in the pump characteristics, while pump heating can cause probe beam defocusing and erroneous apparent contributions to the total measured Kerr coefficient. Although heating effects are small at fast time scales, they can still be significant.

As an example, the thermal response time of nitrobenzene was measured by monitoring the amount of light passing through the sample and a pinhole centered on a beam of wavelength $\lambda = 488$ nm and power of 100 mW as a function of time after exposure. Typical results are given in a log plot (Figure 4) suggesting a response time of about one second. A scanning

pinhole was used to measure the spatial beam profile as a function of beam power as shown in Figure 5. The difference between the incident beam width and the thermally defocused beam width in nitrobenzene was used to determine the thermal contribution to the Kerr coefficient (Figure 6) that was determined from self-defocusing theory[18] to be about 0.1 esu.

The thermal Kerr coefficient, n_2^T, depends on the time, t, after initial illumination by a step function source and the relevant material response time, t_0,

$$n_2^T = n_{02}^T(1-e^{-t/t_0}), \tag{28}$$

where n_{02}^T is the long time thermal Kerr coefficient. With a 20ns pump pulse at wavelength λ_1 = 488 nm, the thermal Kerr contribution is about $2x10^{-9}$ esu. At a typical pump wavelength of 1064 nm, the absorption coefficient is over two orders of magnitude smaller resulting in a thermal contribution of less than $2x10^{-11}$ esu. This upper limit is nearly the electronic and orientational n_2 of single ring aromatic molecules like nitrobenzene and the orientational n_2 of molecules like CS_2. To insure that thermal effects remain negligible, pump pulse durations of less than 100ps are required. Similarly, the long time thermal effects of the cw probe will be negligible for probe powers less than a few mW. Pump heating will not directly cause probe depolarization, but can influence its magnitude through the corresponding refractive index change.

4.2 EFFECTS OF BEAM PARAMETERS

The probe power leaving the Kerr cell is given by Equation (10). The signal is maximum when the angle between the pump and probe polarization vectors is 45° and the measured dependence of the signal (Figure 7) on the polarization angle of pump beam confirms that the signal varies as $\sin^2(2\theta)$. The pump polarization is adjusted to maximize the signal and is fixed for all further measurements.

In the limit of small pump-induced phase shift, the power leaving the Kerr cell, P_{out}, is related to the probe power, P_{in}, and the pump power, P_{pump}, by

$$P_{out} = bP_{in}P_{pump}^2, \tag{29}$$

where b is a power independent constant calculable from equation (10). We note that expression (29) is strictly valid if the pump induced phase change is small and if the response time of the material nonlinearity is fast compared with the laser pulse width; this is always true for the non-resonant electronic contribution. If the response time of the material is comparable to the laser pulse width, the signal will be a convolution of the pump laser pulse shape and the response function of the medium. Equation (23) shows that the gain of the optical gate is proportional to the product of P_{out} and P_{pump} since both the gate and the pump beams are split from the same source. The measured signal is thus proportional to the cw power, P_{in}, and to the cube of the pump power, P_{pump}, for a purely third order process and small pump-induced phase change.

At low pump powers, the signal is cubic in the pump power as expected for a Kerr effect. At higher pump powers (over 40 MW/cm^2), the signal is no longer strictly cubic in P_{pump} and exhibits behavior consistent with saturation, large phase shifts, or higher order processes. If the pump power is varied only in the Kerr cell, the signal should be quadratic in P_{pump}, and this was shown for pump powers less than 40 MW/cm^2. The dependence of the signal on the power of the gate pulse in the KD*P crystal is linear. This validates the calibration of the optical gate as calculated by Equation (23). The signal is also linear in the probe power, P_{out}, showing the absence of thermal defocusing effects up to 10 mW at λ = 590 nm. The long tail of the broad absorption peak of the first strong excited state in nitrobenzene at 260 nm explains the lower defocusing threshold of about 1 mW at 488 nm as opposed to the higher value at 590 nm.

The experimental beam powers are set within limits consistent with the theoretical approximations to permit the signal to be related to the third order susceptibility. In the process

of changing pump and/or probe frequencies, the thresholds for thermal self-defocusing and system component saturation must be monitored and adjusted accordingly.

4.3 DISPERSION MEASUREMENTS

Nitrobenzene and benzene are chosen as model Kerr liquids because the wavelength of their ultraviolet electronic transitions satisfy conditions for sum-resonance of the pump wavelength at 1.06μm with the visible cw probe wavelength. The pure liquid nitrobenzene absorption spectrum is characterized by a broad strong absorption band centered at 4.6 eV with weaker bands between 3 and 4 eV. Gas phase absorption spectra show that there should be a broad weak absorption band at 3.8eV in the pure liquid appearing as a small shoulder at the onset of the 4.6 eV band. In benzene, the first strong absorption band is centered at 4.86eV and a weak band in the near ultraviolet is located at 3.65 eV. The magnitude of $\chi^{(3)}(-\omega_2;\omega_1,-\omega_1,\omega_2)$ for each liquid was measured as a function of probe energy for a range of wavelengths between 610 and 454nm (2.04 to 2.73eV). The results are shown in Figure 8 where the scale was determined by comparing the literature value for CS_2 ($\chi^{(3)} = 2.14 \times 10^{-13}$ esu)[19] to the measured ratio of the optical Kerr constants of nitrobenzene to CS_2 at a probe wavelength of 514.5nm. The error in the data is calculated from equation (21) by attributing a 5% uncertainty to the centroids $C(\omega_2)$ and $C(\omega_r)$ and to the laser powers $P_{in}(\omega_2)$ and P_{pump}. This procedure resulted in a overall statistical uncertainty of 10%; systematic uncertainty is reduced by taking repeated sets of dispersion data. Each $\chi^{(3)}$ data point is an average over five trials that thus reduces the uncertainty to 5%.

5. DISCUSSION

5.1 ELECTRONIC EXCITATIONS

As completely described in the work of Orr and Ward,[20] a quantum mechanical perturbation treatment of the electronic third order susceptibility results in an analytic expression

for the electronic OKE susceptibility that contains terms proportional to the product of four transition moments and inversely proportional to a product of three energy difference terms. Near resonance, the energy denominator of a single term can dominate the frequency dependence of the nonlinear susceptibilty.[21] Under these conditions, the electronic dispersion of the third order susceptibility for an $(\omega_1+\omega_2)$ resonance can be approximated by the phenomenological expression

$$\sigma_R(-\omega_2;\omega_1,-\omega_1,\omega_2) = \frac{A}{\Omega_{1g} - \omega_1 - \omega_2 + i\Gamma}, \tag{30}$$

where Γ is a damping constant, the sum of the pump and probe frequency, $(\omega_1+\omega_2)$, is assumed located near the electronic transition frequency, Ω_{1g}, of the first molecular excited state, and all the factors that are frequency independent near this resonance are assumed to be contained in the constant A.

The measured electronic contribution, $\sigma_R(-\omega_2;\omega_1,-\omega_1,\omega_2)$ as a function of probe frequency with fixed pump frequency, ω_1, then follows the expression

$$|\sigma_R|^2 = \frac{A^2}{(\omega_0 - \omega_2)^2+\Gamma^2}, \tag{31}$$

where $\Omega_{1g} - \omega_1 = \omega_0$. A major advantage of the pump-probe experiment is that the measured resonance does not match the frequency of either the pump or the probe beam. When the sum of the pump and probe frequency matches the material resonance, no single photon absorption occurs, making it possible to probe strong resonances with little depletion of either beam, and thereby allowing thorough study of the electronic contribution to $\chi^{(3)}(-\omega_2;\omega_1,-\omega_1,\omega_2)$. For centrosymmetric molecules, the states that are accessible are necessarily two-photon states which have been shown to be significant contributors to the hyperpolarizability of organic systems.[22] In noncentrosymmetric media one- and two-photon selection rules do not apply and any state is a priori accessible. When $(\omega_1+\omega_2)$ is far from any material excitation energy, the contribution

from all of the nonresonant electronic excitations will be referred to as σ_{NR}. σ_{NR} is present in all materials and will constitute a small background contribution when σ_R is appreciable.

5.2 MOLECULAR REORIENTATION

As has been long known, molecular reorientation can occur if the molecular linear polarizability is anisotropic; for a full discussion of molecular reorientation the reader is referred to Wagner, et. al.[23] An applied electric field can cause alignment of the constituent molecules, imparting a birefringence to the ordinarily isotropic liquid. The energy, W, of a molecule is given by dipole coupling to the field,

$$W(\theta,\phi) = -\mathbf{P}\cdot\mathbf{E} = -\frac{1}{2}\sum_{ij}\alpha_{ij}(\theta,\phi)\langle E_i E_j\rangle, \tag{32}$$

where **E** is the pump field, **P** the induced dipole moment, α_{ij} the linear polarizability, and the brackets denote a time average.

If we assume that each molecule in the liquid acts independently, then for uniaxial molecules the partition function can be written as

$$Z = \frac{1}{2}\int_{-1}^{1} \exp\tfrac{1}{4}[\beta A_1^2(\alpha_\perp+(\alpha_\parallel-\alpha_\perp)\cos^2\theta)]\, d\cos\theta\,, \tag{33}$$

where $\alpha_\perp$ and $\alpha_\parallel$ are the two independent components of the molecular linear polarizability, β the Boltzman factor and A_1 the magnitude of the electric field. The macroscopic susceptibility is given by,

$$\alpha \equiv \frac{4}{\beta}\frac{\ln Z}{A_1^2} \equiv g(A_1^2). \tag{34}$$

The refractive index can be expanded in a Taylor series and the first two terms are

$$n = n_o + \tfrac{1}{2} n_2^{or} E_1^2, \tag{35}$$

where n_o is the linear refractive index and n_2^{or} is the nonlinear index from molecular reorientation. The expression for n_2^{or} in the small signal approximation for the optical Kerr effect owing to molecular orientation is[24]

$$n_2^{or} = \frac{2\pi N}{135kTn_o(\omega_1)}(\alpha_{\parallel}(\omega_2)-\alpha_{\perp}(\omega_2))(\alpha_{\parallel}(\omega_1)-\alpha_{\perp}(\omega_1))F_L, \tag{36}$$

where N is the number density and T is the temperature. Cleary, then, n_2^{or} will adopt the dispersion of the polarizability anisotropy which is relatively flat far from one-photon resonances. The lattice contribution D has Fourier components at zero frequency (molecular reorientation) and at the difference frequency, $\Delta\omega$ (RIKES), and is conventionally written as

$$D \Rightarrow \tfrac{1}{2} B(0) + \{A(\Delta\omega) + \tfrac{1}{2} B(\Delta\omega)\}, \tag{37a}$$

and we can write

$$B(0) = \frac{2n_o^2(\omega_2)n_2^{or}}{3\pi F_L}, \tag{37b}$$

where F_L is the local field factor, and B(0) is that part of the lattice contribution arising from molecular reorientation.

The classic molecular reorientation effect can be thought of as the d.c. response of the molecular nuclei to the intense applied field; there is also the possibility of resonances with vibrational and rotational excitations of the molecular nuclei expressed as a resonant lattice contribution $\{A(\Delta\omega) + \frac{1}{2} B(\Delta\omega)\}$. When the difference between the pump and probe laser frequencies is near a Raman resonance a RIKE[10] is observed, quantified by the Raman line's frequency, linewidth, and amplitude. The optical Kerr effect can be used to measure Raman

spectra by tuning the probe frequency ω_2 through successive resonances or by using a broad band probe hence getting the entire spectrum in one laser shot. It is also clear that by measuring $\chi^{(3)}(-\omega_2;\omega_1,-\omega_1,\omega_2)$ near a Raman resonance one can measure the non-resonant contribution to $\chi^{(3)}$ through a knowledge of Raman scattering data. In this way accurate values of $\chi^{(3)}$ have been obtained for various Kerr liquids;[11] a complete review of these Raman related OKE techniques has been prepared by Levenson and Song.[25] As relates to the current studies, it is important that the difference frequency $\omega_2 - \omega_1$ remain far from fundamental and overtone Raman active modes if a simple interpretation in terms of sum- $(\omega_1 + \omega_2)$ and one- (ω_1,ω_2) photon dispersion is to be possible. Further, a general approach to the interference between resonant $(\chi_R^{(3)})$ and nonresonant $(\chi_{NR}^{(3)})$ terms in OKE measurements is necessary.

5.3 LOCAL FIELD EFFECTS

The macroscopic susceptibility is related to the microscopic susceptibility through frequency dependent local field factors. While there are various prevalent models (Lorentz-Lorenz, Onsager) all of them give the field factors in terms of the refractive index. For a third order process, the local field correction factor, F_L, is a product of four factors, and for the pump-probe configuration is of the form,

$$F_L = f_L^2(n(\omega_1))f_L^2(n(\omega_2)), \tag{38}$$

where there is a local field factor for each incoming and out-going wave. Since only two of the four local field factors are frequency dependent in this pump-probe experiment, the dispersion of the third order susceptibility will be less sensitive to the local field factors than experiments where all frequencies are varied as in third harmonic disperison measurements or in two beam experiments where pump and probe beams are derived from the same source.

In typical dispersion experiments, the range of the probe wavelength is about 200 nm. The change in index over this range is typically less than 5% for our samples and this results

changes of $\chi^{(3)}$ from Lorentz-Lorenz field factors ($f_L = \frac{1}{9}(n^2+2)(n^2+2)$) by about 9%. This is small compared to the effects of dispersion on resonance that typically enhance the signal by a factor of two or more in states of weak oscillator strength that are at the detection limit of linear absorption measurements. For strong resonances, the dispersion from the local field factors is negligible. For the remainder of this paper we will assume that the local field variation in the the nonlinear susceptibility is negligible over the frequency range interrogated, so the local field factor will not be explicitly shown. However if accurate comparisons of different materials is required the local field factors must be included.

5.4 INTERFERENCE BETWEEN RESONANT AND NONRESONANT PARTS OF $\chi^{(3)}$

The pump and probe laser frequencies used in the present measurements are far off resonance for both benzene and nitrobenzene with little dispersion of the linear refractive index (~2%) over the same range (see table 1). Hence, any dispersion in the measured signal is due to electronic sum- and difference-resonances as evident, for example, in Equation (31). If the sum frequency corresponds to a weak electronic excitation, the total susceptibility will be a sum of resonant, $\chi_R^{(3)}$, and nonresonant, $\chi_{NR}^{(3)}$, components,

$$\chi^{(3)} = \chi_R^{(3)} + \chi_{NR}^{(3)}, \tag{39}$$

where the magnitude is given by

$$|\chi^{(3)}| = [\,|\chi_R^{(3)}|^2 + |\chi_{NR}^{(3)}|^2 + 2RE[\chi_R^{(3)}\,\chi_{NR}^{(3)}]\,]^{1/2}, \tag{40}$$

and the spectrum will exhibit the interference between the resonant and nonresonant portions as first studied extensively by Levenson, et. al.[26] In terms of our previously defined parameters

$$\chi_R^{(3)} = \sum_n \sigma_R^n + \frac{1}{24}\sum_n \{2A_n(\Delta\omega) + B_n(\Delta\omega)\}. \tag{41a}$$

$$\chi^{(3)}_{NR} = \frac{1}{24}(\sigma_{NR} + B(0)), \tag{41b}$$

where σ^m_R is the resonant contribution to the hyperpolarizability centered at frequency Ω_{mg}, and $A_n(\Delta\omega)$ and $B_n(\Delta\omega)$ are the resonant Raman contributions to the nonlinear susceptibility at center frequency ω_n. Thus knowledge of $\chi^{(3)}_{NR}$ can allow determination of the separate resonant contributions while a prediction for $\chi^{(3)}_R$ (say, from molecular orbital calculations) can be used to determine the nonresonant nonlinear susceptibility.

The nonresonant susceptibility $\chi^{(3)}_{NR}$ has a weak frequency dependence that can be observed if measurements are made over a broad enough frequency range. σ_{NR} and B(0) must be treated separately, since the dispersion of B(0) follows that of the linear polarizability anisotropy, while that of σ_{NR} is related to the second hyperpolarizability. One immediate ramification is that B(0) can only derive frequency dependence from a product of two one-photon energy denominators, while σ_{NR} obtains dispersion from a product of three one- and two-photon energy denominators.

Several methods exist for developing such an expansion for σ_{NR}, ranging from a direct expansion of the time dependent perturbation theory result to calculations based on isotropic anharmonic oscillator models of the nonlinear susceptibility.[27] In the model of Owyoung,[27] σ_{NR} is written as

$$\sigma^{OW}_{NR}(-\omega_2;\omega_2,\omega_1,-\omega_1) \sim \alpha^2(\omega_2)\alpha^2(\omega_1), \tag{42}$$

where α is the isotropically averaged linear polarizability. If we suppose we can expand the linear polarizability according to its representation as a harmonic oscillator

$$\alpha(\omega_n) = \alpha_0(1+(\omega_n/\Omega_0)^2 + \ldots), \tag{43}$$

where Ω_0 is the frequency of a large oscillator strength high energy excited state, then we get the following result for σ_{NR}

$$\sigma_{NR}(-\omega_2;\omega_1,\omega_1,-\omega_1) = \alpha^4_0\,(1+(\frac{\omega_1}{\Omega_0})^2)\,(1+(\frac{\omega_2}{\Omega_0})^2)^2. \tag{44}$$

If we let $\alpha_0^4\,(1+(\frac{\omega_1}{\Omega_0})^2)^2 = \sigma_0$ then

$$\sigma_{NR} \equiv \sigma_0(1+2(\frac{\omega_2}{\Omega_0})^2), \tag{45}$$

so the ω_2 dependence is quadratic to lowest order.

Alternatively, we can use the result for σ from third order perturbation theory in the dipole approximation. If damping is assumed to be negligible then it can be shown that this must be an expansion in even powers of the optical frequency. If damping is present as when our probe frequency approaches a sum-resonant frequency then the expansion will contain terms linear in ω_2. Explicit knowledge of molecular wavefunctions and energy levels would be necessary to obtain the coefficients in this expansion so we simply write

$$\sigma_{NR}^{PT} = C_1 + C_2\omega_2. \tag{46}$$

From (37), B(0) obtains dispersion from the polarizability anisotropy. Since a single one photon energy denominator contributes in this case we might expect B(0) to have less dispersion than σ_{NR}, however, B(0) is generally larger than σ_{NR} in liquids, so the frequency dependence of B(0) may be appreciable. For the sake of simplicity we assume B(0) to be frequency independent within the experimentally measured regions, and discuss the success of this ansatz a posteriori.

In terms of equations (41) we can write

$$\chi^{(3)} = \frac{1}{24}(\sigma_{NR} + B(0)) + \frac{1}{24}\sum_n \{2A_n(\Delta\omega) + B_n(\Delta\omega)\} + \sum_n \sigma_R^n . \qquad (47)$$

Whichever model we adopt there will be certain shared characteristics in the spectra, notably the appearance of Fano-like[28] resonance peaks when $\omega_1+\omega_2 = \Omega_{mg}$, resulting from the interference of $\chi_R^{(3)}$ and $\chi_{NR}^{(3)}$. When $\chi_R^{(3)}$ is a Lorentzian resonance, the upper portion of Figure 9 shows the absolute magnitude of the susceptibility with $\chi_{NR}^{(3)} = 0$. In the bottom portion, $\chi_{NR}^{(3)}$ is given by either (48) or (49), which are valid if other electronic excitations are far from resonance.

5.5 $\chi^{(3)}$ OF BENZENE AND NITROBENZENE

The observed dispersion for nitrobenzene can be understood in terms of the gas phase linear absorption spectrum which gives the energies and oscillator strengths of the electronic excited states in the near ultraviolet.[29,30] The general rise in the $|\chi^{(3)}|$ data (Figure 8) may be related to the onset of a sum resonance with the high oscillator strength state at 5.11 eV (gas phase), while the fine structure at a probe energy of 2.6 eV is associated with a weak gas phase transition at 4.35 eV . In neat solution the 5.11 eV band is red shifted by 0.65 eV,[13] thus shifting the sum resonances by an equivalent amount. The rather complex fine structure may result from interference between a sum resonance with the red-shifted 4.35 eV band and a difference resonance ($\omega_2 - \omega_1$) with an near infrared overtone band centered at 1.48 eV. The data was analyzed using (47) with Lorentzian resonances centered at probe energies of 2.55 eV (sum - electronic) and 2.66 eV (difference - nuclear) and experimentally determined widths of 0.09 eV and 0.04 eV, respectively. If σ_{NR} was assumed to have no frequency dependence, a good fit could be achieved to all but the point at the highest probe energy (Figure 8). The 2.55 eV resonance amplitude was 15% of the nonresonant background, while the 2.66eV peak was weaker with an amplitude of 9% of the background and the estimated error in these amplitudes was approximately 5%. Far from resonance this model predicts $\sum_m \sigma_R^m$ constitutes 15% of the nonresonant $\chi^{(3)}$, and this is in good agreement with other experiments.[15]

If σ_{NR} was allowed to have frequency dependence, then both models (45) and (46) predict that B(0) must be negative, and this is ruled out by the positive definite expression (36). Since the next strong sum resonant excited state is at a probe energy of 3.3 eV, it may be close enough to prevent the binomial expansions (45) and (46) from being applicable, thus suggesting that a three Lorentzian model might be necessary ; this was not attempted because there was no data at higher energies. Furthermore, the large resonant contribution may completely mask the nonresonant frequency dependence, including any dependence from B(0) that we have neglected. A likely reason for the failure of the expansion (45) to explain the nonresonant behavior is that the coefficient of the quadratic term as predicted by the theory is incorrect, as has been observed in dc-field induced second harmonic generation experiments.[31]

Benzene possesses primary excited states at 4.75, 6.14 and 6.74 eV in the gas phase, and these suffer from little dielectric shift in the liquid. The $|\chi^{(3)}|$ spectrum of benzene (Figure 8) shows less pronounced structure than that of nitrobenzene because of the smaller dielectric shift and the preservation of the parity selection rule in the centrosymmetric benzene molecule. The $|\chi^{(3)}|$ data is largely dispersion-free aside from some structure at a probe energy of ~ 2.5 eV that coincides with a weak optical transition near 3.7 eV reported for liquid benzene.[32] The first strong excited state at 4.86 eV is not experimentally accessible because of the small solvent shift and the lack of a sum-photon contribution from that state. We note that the measured nonresonant value of $|\chi^{(3)}|$ benzene at λ_2 = 514.5 nm was about two times less than that of nitrobenzene, which is in agreement with the literature when laser pulse length corrections are accounted for.[33]

As in the case of nitrobenzene, the benzene spectrum shows the structure that results from the interference between a Lorentzian resonance and the background of molecular reorientation and non-resonant electronic transitions. If the polynomial expansion (46) is employed the benzene spectrum can be well described by a single Lorentzian with A=-0.0678 x 10^{-13} esu-eV, ω_o = 2.50 eV, Γ = 0.011 eV, C_1 + B(0) = 24.9 x 10^{-13} esu and C_2 = -4.28 x10 esu/eV with estimated errors as above. The Lorentzian parameters are reasonable for a weak

oscillator strength transition in a room temperature liquid and describe the electronic contribution of the weak state at 3.7 eV in benzene; furthermore they suggest that this state has appreciable sum-resonant character. The sign of C_2 is unexpected and may result from frequency dependence in B(0) or from angular correlations between adjacent benzene molecules, which have not been considered. The total electronic contribution can only be determined if the probe frequency is tuned through the significant sum-resonant states and the Lorentzian parameters determined as above. For the present study, we illustrate the technique by determining the electronic contribution from one weak excited state, while σ and B(0) remain unseparated.

6. CONCLUSION

An experimental and theoretical study of OKE dispersion in isotropic media has been presented. A theoretical analysis based on Maxwell's equations provides the connection between experimentally measured quantities and $\chi^{(3)}_{ijkl}(-\omega_2;\omega_1,-\omega_1,\omega_2)$. An optimized pump-probe depolarization technique was developed, and conventional theoretical approximations carefully studied. Thresholds for pump saturation and thermal lensing were obtained, and experimental powers accordingly adjusted. The OKE dispersion data is used to determine the resonant and nonresonant contributions to $\chi^{(3)}_{ijkl}(-\omega_2;\omega_1,-\omega_1,\omega_2)$ near sum-frequency resonances, and can be used to separate the nonresonant electronic and lattice contributions when a broad enough frequency range is investigated. The data were analyzed according to a simple model that required comparison with linear absorption spectra, a polynomial expansion of the nonresonant electronic contribution, and consideration of dipole selection rules. The complex nitrobenzene spectrum was seen to result from an interference between a sum-frequency resonance ($\omega_1 + \omega_2$), a difference-frequency resonance ($\omega_2 - \omega_1$), and nonresonant contributions. A simple model succeeded in explaining the results for benzene for which a single weak electronic transition at 3.7 eV was probed far from any other resonances in the presence of a nonresonant background. The general formalism presented in this study can be adopted for the study of resonant $\chi^{(3)}$

resonant $\chi^{(3)}_{ijkl}$ processes in any other media of interest, and the experimental data can be compared to a microscopic theory based upon many electron molecular orbital calculations.[30]

Table 1. Dispersion of Refractive Index of Nitrobenzene and Benzene[34]

Wavelength (nm)	Refractive Index		
	Nitrobenzene	Benzene	
		20^0 C	25^0 C
667.8	1.54683	1.49578	1.49262
656.5	1.54785	1.49643	1.49327
589.0	1.55240	1.50112	1.49792
587.6	1.55483	1.50521	1.50197
503.0	1.56947	1.51077	1.50748
486.3	1.57325	1.51313	1.50982
447.1	1.58566	1.52302	1.51964

FIGURE CAPTIONS

Figure 1. Experimental layout where HWP1 is a half wave plate at 1.06μm, P1 and P2 polarizers, A1 and A2 analyzers, BS1 and BS2 beamsplitters, MDM1 and MDM2 motor driven mirrors, KDP mixing crystals, PD photodiodes, F1 and F2 filters and PMT's are photomultiplier tubes.

Figure 2. Typical pump and probe beam profiles. The pump profile is seen to agree with the parabolic approximation (dashed line) within the probe beam waist.

Figure 3. Poissonian pulse height distribution of normalized PMT signal accumulated over 30,000 laser shots.

Figure 4. Log plot of the heating decay curve of nitrobenzene with a time constant of 1.42 sec.

Figure 5. Thermal defocusing profile in nitrobenzene as determined with a scanning pinhole.

Figure 6. Argon ion beam profiles at a wavelength of 488 nm and a power of 60 mW through nitrobenzene (solid curve) and without sample (dashed curve).

Figure 7. Kerr signal as a function of half wave-plate angle (see Figure 1) in the pump beam path. Curve represents the expected $\sin^2 2\theta$ dependence.

Figure 8. $|\chi^{(3)}|$ dispersion data for nitrobenzene is given by the solid points and benzene data is given by the open points.

Figure 9. The upper curve shows a Lorentzian form of the absolute value of the susceptibility for a two level model, while the bottom curve shows the behavior of the absolute value of an offset Lorentzian.

Figure 1. Experimental layout where HWP1 is a half wave plate at 1.06μm, P1 and P2 polarizers, A1 and A2 analyzers, BS1 and BS2 beamsplitters, MDM1 and MDM2 motor driven mirrors, KDP mixing crystals, PD photodiodes, F1 and F2 filters and PMT's are photomultiplier tubes.

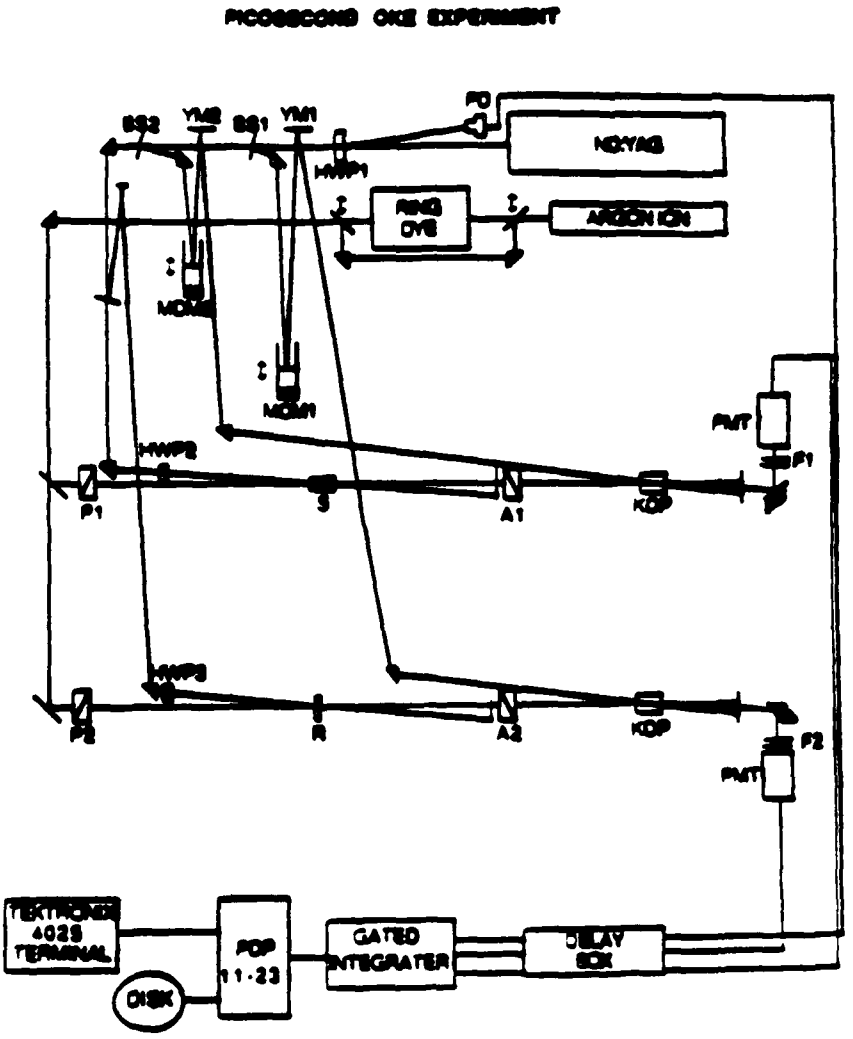

Figure 2. Typical pump and probe beam profiles. The pump profile is seen to agree with the parabolic approximation (dashed line) within the probe beam waist.

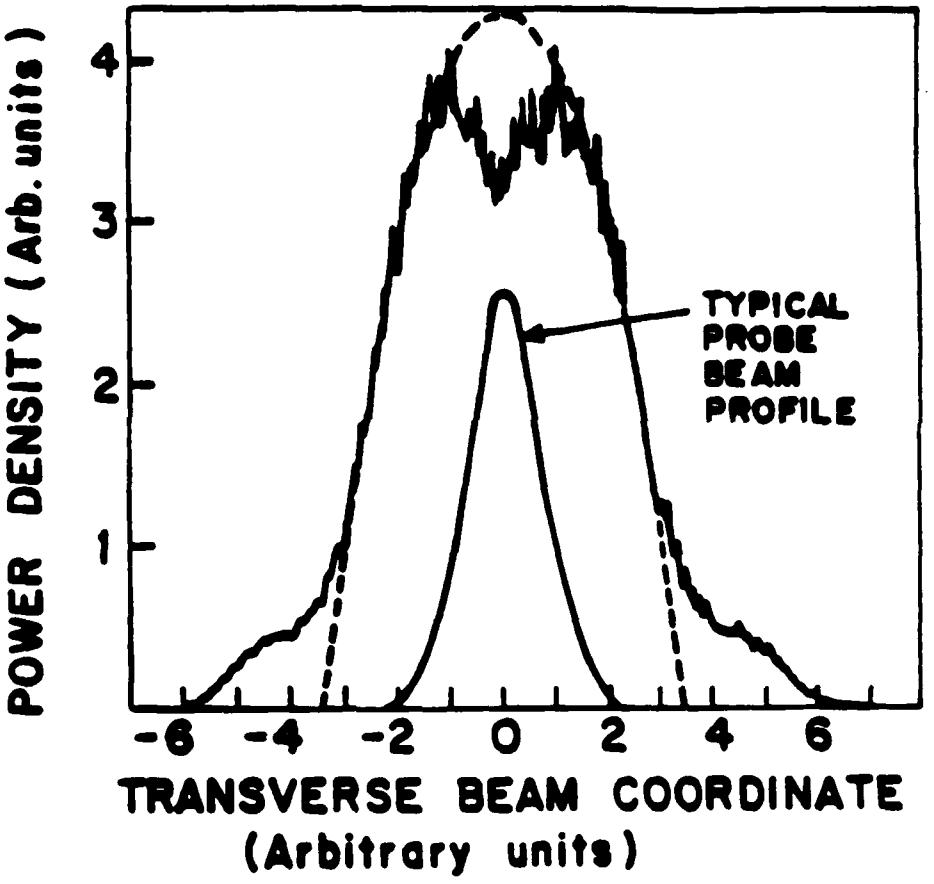

Figure 3. Poissonian pulse height distribution of normalized PMT signal accumulated over 30,000 laser shots.

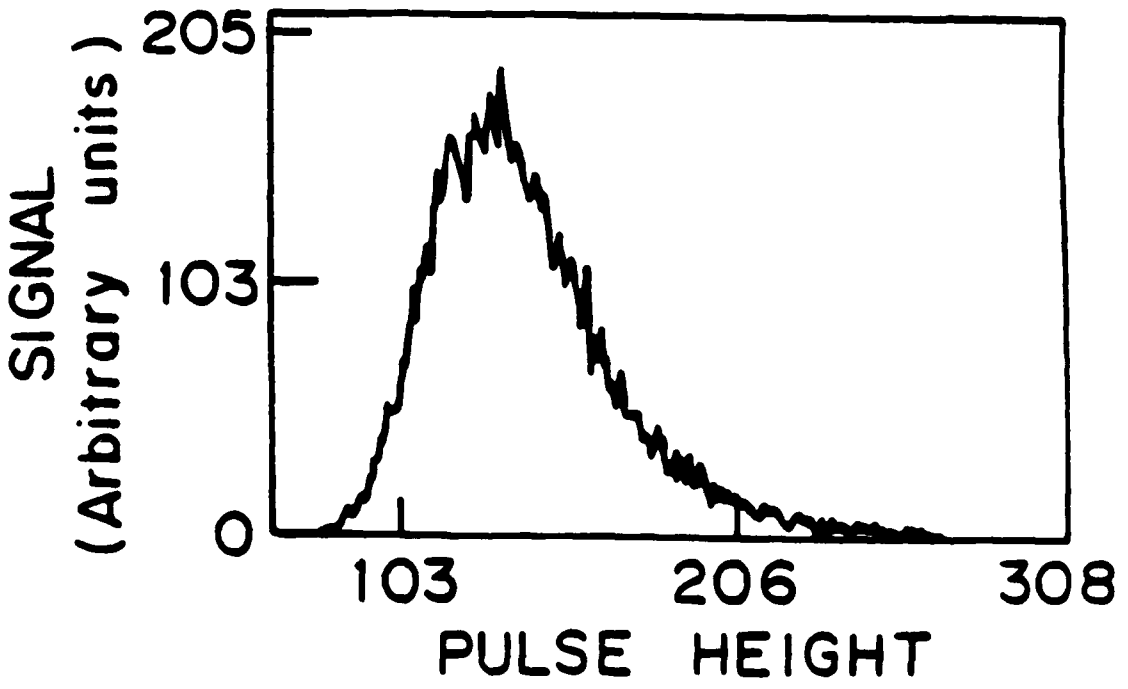

Figure 4. Log plot of the heating decay curve of nitrobenzene with a time constant of 1.42 sec.

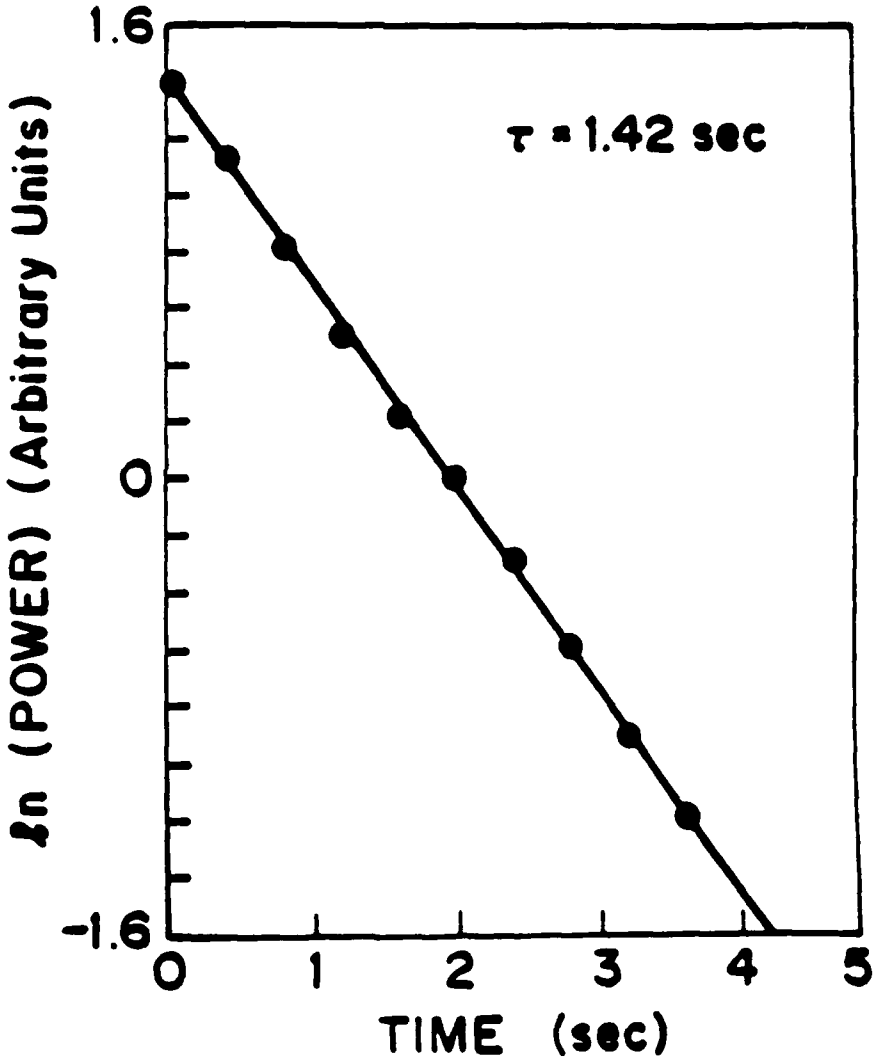

Figure 5. Thermal defocusing profile in nitrobenzene as determined with a scanning pinhole.

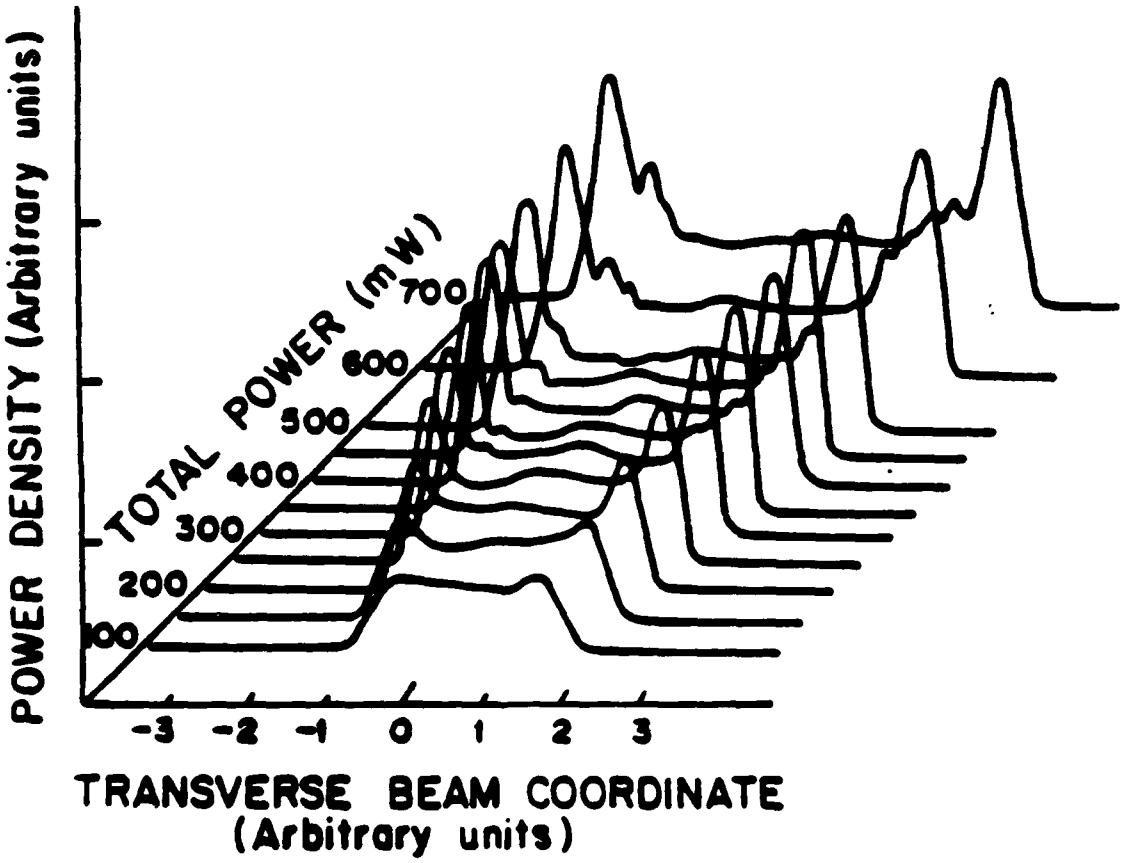

Figure 6. Argon ion beam profiles at a wavelength of 488 nm and a power of 60 mW through nitrobenzene (solid curve) and without sample (dashed curve).

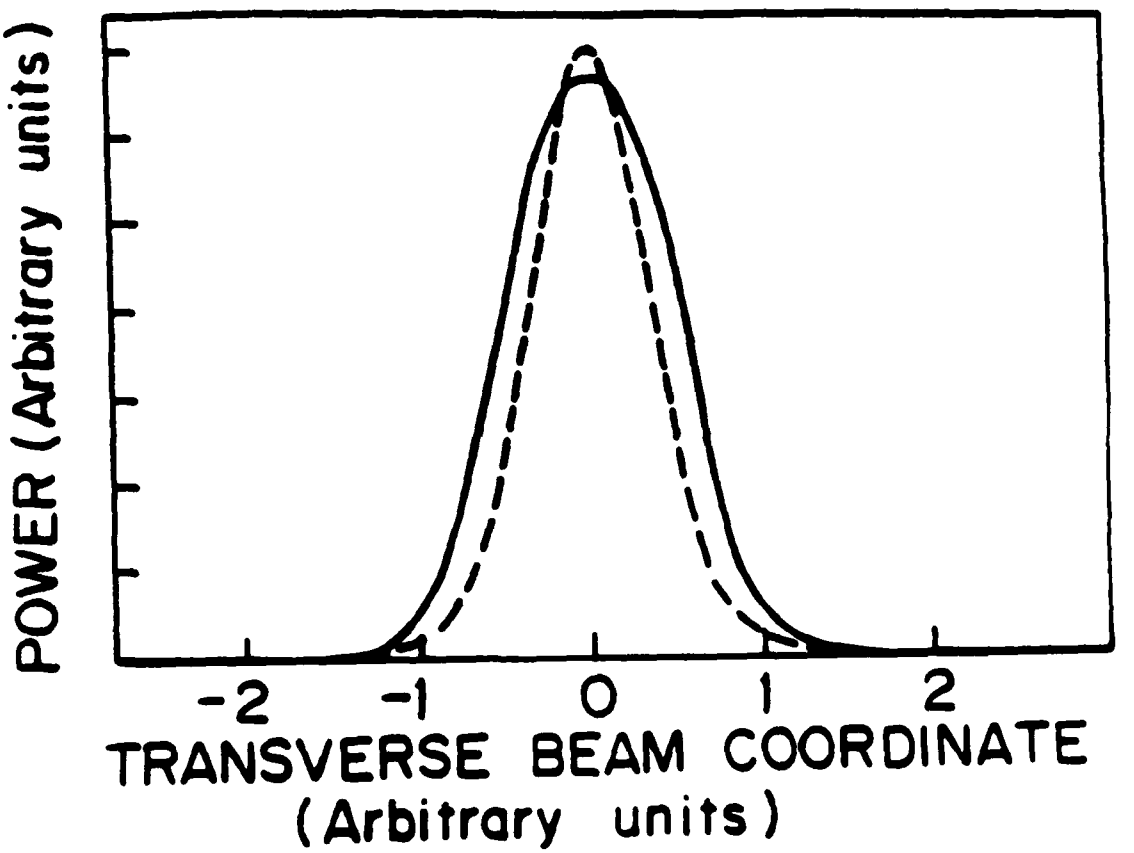

Figure 7. Kerr signal as a function of half wave-plate angle (see Figure 1) in the pump beam path. Curve represents the expected $\sin^2 2\theta$ dependence.

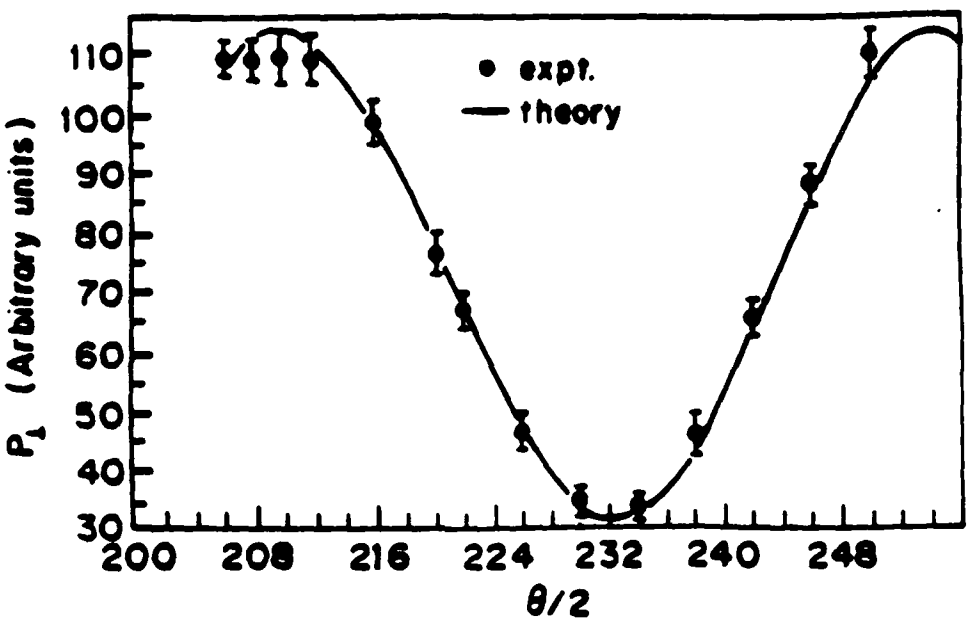

Figure 8. $|\chi^{(3)}|$ dispersion data for nitrobenzene is given by the solid points and benzene data is given by the open points.

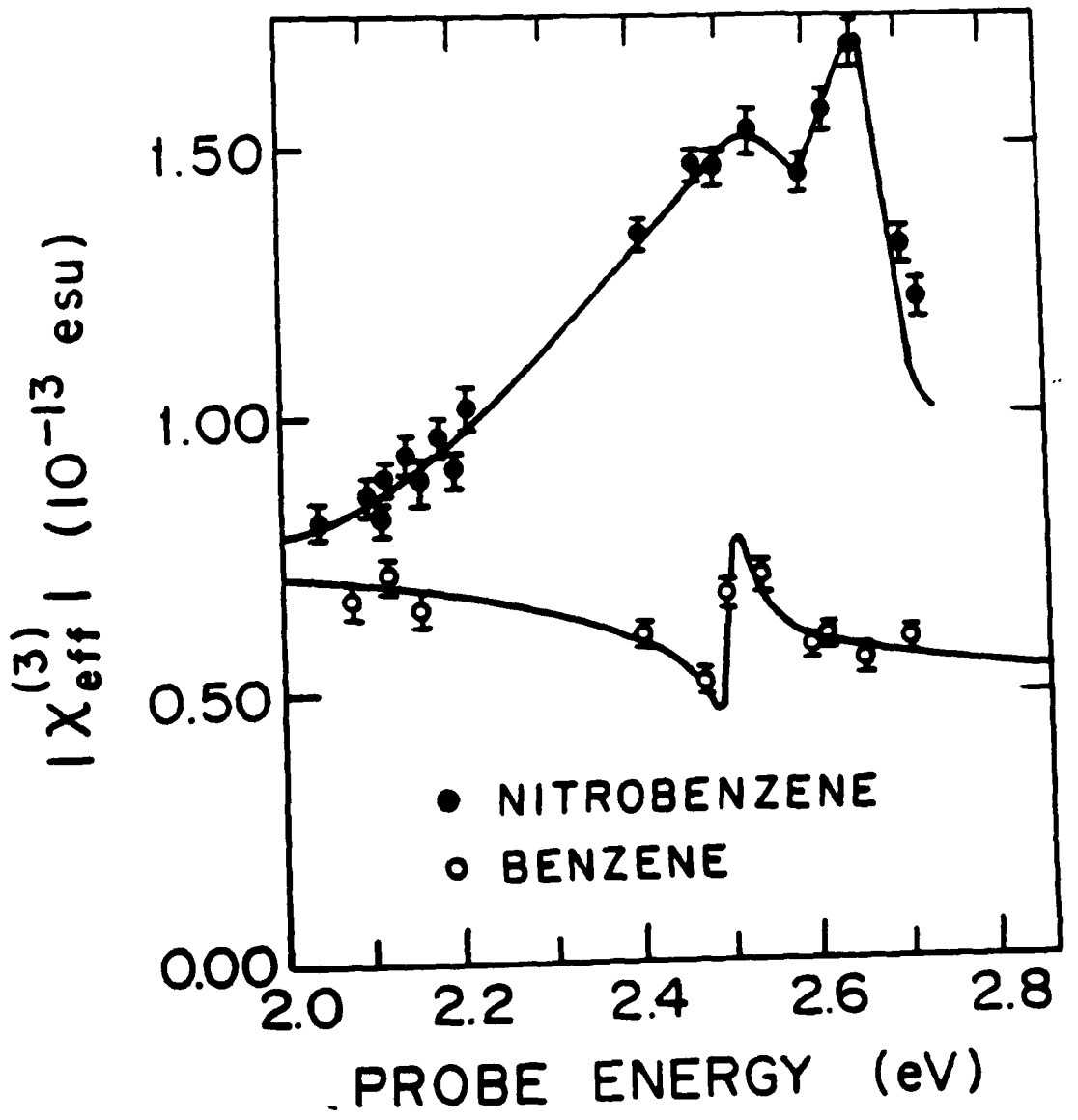

Figure 9. The upper curve shows a Lorentzian form of the absolute value of the susceptibility for a two level model, while the bottom curve shows the behavior of the absolute value of an offset Lorentzian.

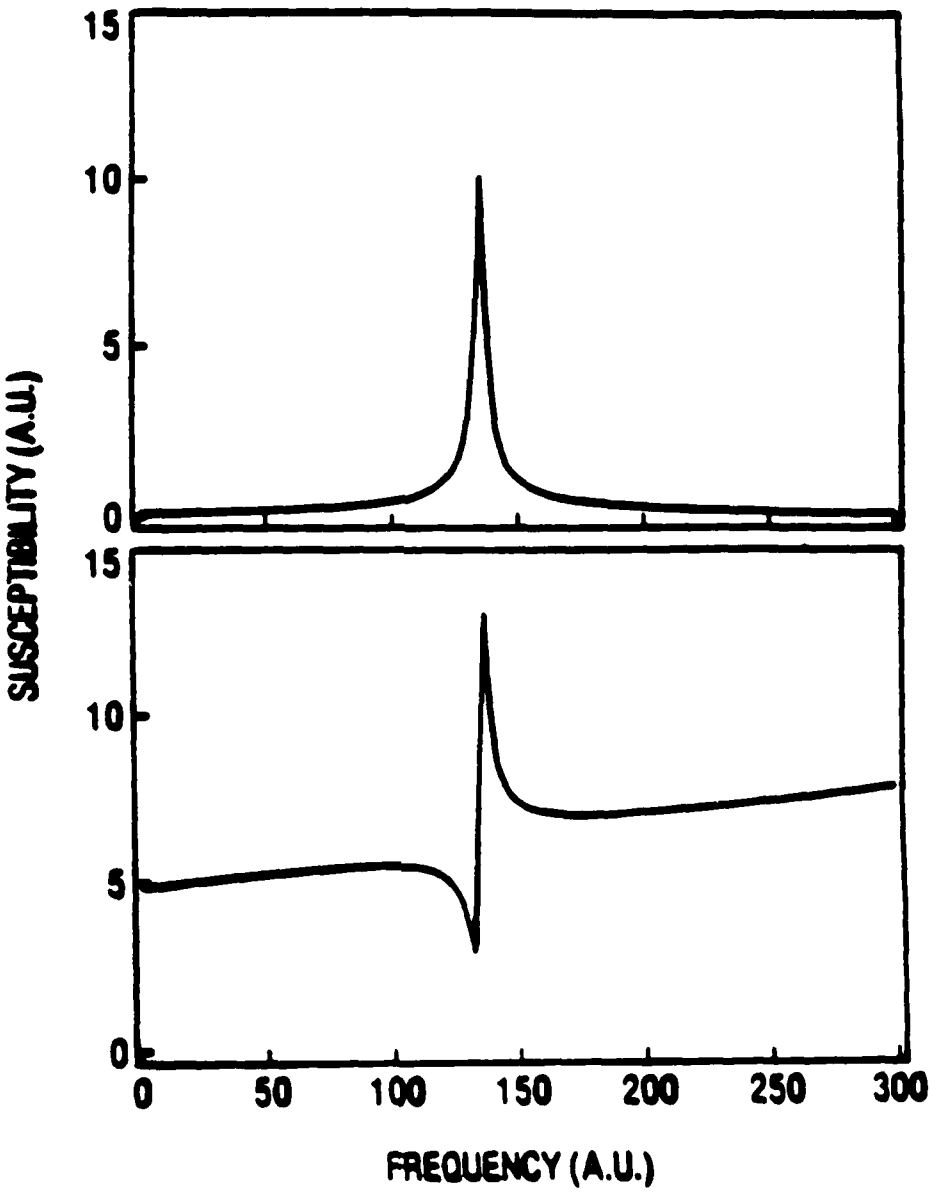

REFERENCES

1. G. Mayer and F. Gires, *C.R. Acad. Sci.* **258**, 2039 (1964).
2. P. Maker and R. Terhune, *Phys. Rev.* **137**, A801 (1965).
3. P. P. Ho and R.R. Alfano, *Phys. Rev.* **A20**, 2170 (1979).
4. H. Kildal and S. R. J. Brueck, *J. Chem. Phys.* **73**, 4951-8 (1980).
5. J. Etchepare, G. Grillon, I. Thomazeau, A. Migus and A. Antonetti, *J. Opt. Soc. Am.* **B2**, 649 (1985).
6. R. W. Hellwarth, *Prog. Quant. Electr.* **5**, 1 (1977).
7. B. I. Greene and R. C. Farrow, *J. Chem. Phys.* **77**, 4779 (1982).
8. W. T. Lotshaw, D. McMorrow, C. Kalpouzos, and G. Kenney-Wallace, *Chem. Phys. Lett.* **136**, 323 (1987).
9. J. Etchepare, G. Grillon, G. Hamoniaux, A. Antonetti, and A. Orszag, *Revue, Phys. Appl.* **22**, 1749 (1987).
10. D. Heiman, R. W. Hellwarth, M. D. Levenson, and Graham Martin, *Phys. Rev. Lett.* 36, 189 (1976).
11. J. J. Song and M. D. Levenson, *J. Appl. Phys.* **48**, 3496 (1977).
12. M. G. Kuzyk, R. A. Norwood and A. F. Garito, *J. Opt. Soc. Am.* **B2**, P45 (1985).
13. M. G. Kuzyk, Ph. D. thesis, U. of Penn., 134 (1985).
14. E. Ippen and C. V. Shank in Ultrashort Light Pulses, ed. S.L. Shapiro (Springer-Verlag, New York, 1984) p. 83.
15. K. Sala and M. C. Richardson, *Phys. Rev. A* **12**, 1036 (1975).
16. J. G. Fujimoto, A. M. Weiner, and E. P. Ippen, *Appl. Phys. Lett.* **44**, 832 (1984).
17. J. Aaviksoo, A. Anijalg, A. Freiberg, and K. Timpmann, *Appl. Phys.* **B4**, 213 (1985)
18. S. A. Akhmanov, R. V. Kokhlov and A. P. Sukorukar, *Laser Handbook*, F. T. Arecchi and E.O. Schulz-Dubois, Eds. (N. Holland Pub. Co., Amsterdam, 1972) p. 1151.

19. E. A. Volkova, V. A. Zamkov, and L. V. Nalbandov, *Opt. and Spectr. (USSR)* **30**, 300 (1971).

20. B. J. Orr and J. F. Ward, *Molecular Physics* **20**, 513 (1971).

21. J. A. Armstrong, N. Bloembergen, J.Ducuing, and P. S. Pershan, *Phys. Rev.* **127**, 1918 (1962).

22. J. R. Heflin, K. Y. Wong, O. Zamani-Khamiri, and A. F. Garito, *Phys. Rev.* **B.** (in press).

23. W. G. Wagner, H. A. Haus and J. H. Marburger, *Phys. Rev.* **175**, 256 (1968).

24. A. D. Buckingham, *Proc. Phys. Soc.* **A68**, 910 (1955).

25. M. D. Levenson and J. J. Song, in *Advances in Coherent Optics*, edited by M.S. Feld and V. S. Letokhov (Springer-Verlag, New York, 1980), p.293.

26. M. D. Levenson, C. Flytzanis, and N. Bloembergen, *Phys. Rev.* **B6**, 3962 (1972).

27. A. Owyoung, Ph. D. thesis, Cal. Inst. of Tech., (1972).

28. U. Fano, *Phys. Rev.* **125**, 1866 (1961).

29. S. Nagakura, M. Kojima and Y. Maruyama, *J. of Mol. Spec.* **13**, 174 (1964).

30. O. Zamani-Khamiri, R. A. Norwood, J. Wu and A. F. Garito, *J. Opt. Soc. Am.* **B3**, P96 (1986).

31. V. Mizrahi and D. P. Shelton, *Phys. Rev. Lett.* **55**, 696 (1985).

32. A. Sklar, *J. Chem. Phys.* **5**, 699 (1937).

33. A. K. Burnham and T. D. Gierke, *J. Chem. Phys.* **73**, 4822 (1980).

34. J. Timmermans, *Physico-Chemical Constants of Pure Organic Compounds*, Vol. 2, Elsevier (Amsterdam, 1965).